Towards Geochemical Insight Using Sum-Frequency Generation Spectroscopy

by

Paul A. Covert
B.A., Reed College, 1995
M.Sc., Oregon State University, 2001

A Dissertation Submitted in Partial Fulfillment of the
Requirements for the Degree of

DOCTOR OF PHILOSOPHY

in the Department of Chemistry

University of Victoria

Towards Geochemical Insight Using Sum-Frequency Generation Spectroscopy

by

Paul A. Covert
B.A., Reed College, 1995
M.Sc., Oregon State University, 2001

Supervisory Committee

Dr. Dennis Hore, Supervisor
(Department of Chemistry)

Dr. Alex Brolo, Departmental Member
(Department of Chemistry)

Dr. David Harrington, Departmental Member
(Department of Chemistry)

Dr. Robie Macdonald, Outside Member
(School of Earth and Ocean Sciences)

Supervisory Committee

Dr. Dennis Hore, Supervisor
(Department of Chemistry)

Dr. Alex Brolo, Departmental Member
(Department of Chemistry)

Dr. David Harrington, Departmental Member
(Department of Chemistry)

Dr. Robie Macdonald, Outside Member
(School of Earth and Ocean Sciences)

ABSTRACT

The molecular structure of solvent and adsorbates at naturally occurring solid–liquid interfaces is a feature that defines much of the chemistry of the natural environment. Because of its importance, this chemistry has been studied for many decades. More recently, nonlinear optical techniques have emerged as a valuable tool for non-invasive investigation of environmental interfaces, in part because of their inherent surface specificity. Solid–aqueous interfaces are complex regions in which chemical and electrostatic forces combine to drive adsorption processes. Second-harmonic generation and sum-frequency generation (SFG) spectroscopies have been employed by many groups to investigate water structure at these interfaces over a range of pH and ionic strength environments. In this thesis, I report results of further investigation of water structure adjacent silica, fluorite, polystyrene, and poly (methyl methacrylate) surfaces in the presence of varying concentrations of Na^+ and Cl^-. A model is developed to describe the SFG response from the fused silica–solution interface as ionic strength is increased. This model reveals both details of interfacial water structure and the interplay between second- and third-order optical responses present at charged interfaces. In context of this model, water structure at the three other interfaces is discussed.

Knowledge of the phase of the SFG response provides additional surface structural information that can be related to the polar orientation of a molecule or functional group, for example, a flip in the orientation of water at an interface. Methods to capture the phase information at exposed interfaces are well established, but buried interface phase measurement remains a challenge. Therefore, I focused on development of a systematic method for buried interface phase measurement. In this thesis, I demonstrate improvements in the precision and accuracy of two phase-sensitive SFG techniques for measurement of exposed interfaces. Results from efforts to extend the theory to the buried interface are presented, along with an examination of the challenges encountered along the way.

Contents

List of Symbols and Definitions

Symbol	**Units**	**Description**
d	µm	optical thickness
$\hat{e}$		unit polarization vector
h	J s	Planck's constant
m	kg	mass
n		complex refractive index
$\mathrm{pH}_{\mathrm{pzc}}$		pH at point of zero charge
(tt)		compound Fresnel coefficient of transmission
A		transition polarizability magnitude
$\mathbf{E}$	$\mathrm{V\,m^{-1}}$	electric field
I	$\mathrm{mol\,L^{-1}}$	ionic strength
I_{SFG}	$\mathrm{W\,m^{-2}}$	measured SFG signal
L		local field correction factor
N		number of molecules
N_{A}	$\mathrm{mol^{-1}}$	Avogadro's number
$\mathbf{P}$	$\mathrm{C\,m^{-2}}$	induced polarization
R	$\mathrm{J\,K^{-1}\,mol^{-1}}$	universal gas constant
T	K	absolute temperature

Symbol	**Units**	**Description**
α	deg	phase shifting unit tilt angle
$\alpha^{(1)}$	$\mathrm{C\,m\,V^{-1}}$	linear molecular polarizability
$\alpha^{(2)}$	$\mathrm{C\,m^2\,V^{-1}}$	second-order molecular polarizability
$\alpha^{(3)}$	$\mathrm{C\,m^3\,V^{-1}}$	third-order molecular polarizability
ε_0	$\mathrm{C\,V^{-1}\,m^{-1}}$	vacuum permittivity
ε		bulk dielectric constant
θ	deg	angle of incidence
κ^{-1}	nm	Debye length
μ	$\mathrm{C\,m}$	electric dipole moment
ν	$\mathrm{cm^{-1}}$	frequency
σ_0	$\mathrm{C\,m^{-2}}$	surface charge
φ	rad	electric field phase
$\Delta\varphi$	rad	electric field phase shift
$\chi^{(1)}$		linear electric susceptibility
$\chi^{(2)}$	$\mathrm{V\,m^{-1}}$	second-order electric susceptibility
$\chi^{(3)}$	$\mathrm{V^2\,m^{-2}}$	third-order electric susceptibility
ω	$\mathrm{rad\,s^{-1}}$	angular frequency
Γ	$\mathrm{cm^{-1}}$	linewidth
Ψ	V	potential

Symbol	**Description**
BBO	β-barium oxide
DFG	difference frequency generation
IR	infrared
LO	local oscillator
NR	non-resonant
ODT	1-octadecanethiol
OPA	optical parametric amplifier
OPG	optical parametric generator
OPL	optical path length
OTS	octadecyltrichlorosilane
SHG	second harmonic generation
SFG	sum-frequency generation
PS-SFG	phase-sensitive sum-frequency generation
PSU	phase shifting unit
PMMA	poly(methyl methacrylate)
SAM	self-assembled monolayer

List of Tables

List of Figures

ACKNOWLEDGEMENTS

The work presented in this thesis could not have been accomplished without the help of many people. First and foremost is Dennis Hore, whose advice, encouragement, and curry dinners pulled me through the frustrating moments of this thesis. I have learned an immense amount from you, Dennis, and I hope that I may return that gift in kind at some point in the future.

Thanks to my committee, Alexandre Brolo, David Harrington, Robie Macdonald who have taken the time to discuss my work with me, as well as to read and comment upon this document.

I also wish to thank Franz Geiger and Northwestern University in Illinois and Matt Moffitt at University of Victoria for discussions regarding the salt manuscripts. I further thank Regivaldo G. Sobral-Filho and Milton Wang for advice on preparation of the ODT SAMs.

During my time at UVic, the core group members were Kailash Jena, Shaun Hall, Sandra Roy, and William FitzGerald. You have all provided much needed cynicism, good food, good drink, coffee runs, oh...and scientific discussion.

Of course, none of this work could have been completed without help from the machine shop, glass shop, instrument shop, and Ekspla. I has been a pleasure working with all of you: Jean-Paul Gogniat, Chris Secord, Sean Adams, and Andrew MacDonald. Thanks to Robertas Kananavicius for his patience in the laser alignment task we set before him.

Funding for this research was from the Natural Science and Engineering Research Council of Canada (NSERC). Additional support for presentation of this work at international meetings was provided by the University of Victoria Faculty of Graduate Studies. The Mark and Nora de Goutiere Memorial Scholarship and the Lewis J. Clark Memorial Fellowship provided further financial assistance.

DEDICATION

In memory of Margret J. Geselbracht.

Chapter 1

Motivations

My attraction to surface-specific spectroscopies stems from questions that arose during my Master's research in Professor Prahl's group at Oregon State University. That research focused on changes in the bulk elemental compositions of suspended particles in the Columbia River as they were advected from freshwater riverine environments to more saline estuarine waters.[1] Significant changes in composition were observed for both the organic and mineral fractions of the particles as they entered the estuary, but this was not examined. What always piqued my curiosity, were the changes in *surface* chemistry that occurred. Undoubtedly, surface chemistry was different in the two very different aquatic environments, but at the time I did not have the tools needed to study that chemistry.

There are many established methods for probing surface chemistry. The family of second-order, nonlinear optical spectroscopies, such as sum-frequency generation (SFG) spectroscopy, provides the surface specificity needed to address such questions. SFG spectroscopy has become a powerful tool for the examination of a large variety of surfaces and environments. In the past decade, as SFG theory and methods have matured, SFG has found its way into studies of increasingly complex systems.

The scientific question originally driving the research presented in this thesis was: *what is the effect of pH upon interfacial water structure and orientation at the calcium carbonate–seawater interface?* It was my hypothesis that in the vicinity of the calcite point of zero charge ($\mathrm{pH_{pzc}} \approx 8$)[2] water molecules would be weakly ordered and at pH levels above and below $\mathrm{pH_{pzc}}$ water would exhibit a strong polar ordering. Furthermore, it is my hypothesis that the polar ordering at pH levels greater than $\mathrm{pH_{pzc}}$ would be opposite of the ordering at pH levels less than $\mathrm{pH_{pzc}}$. This ordering may play a critical role in the process of biological $CaCO_3$ shell formation and dissolution,[3,4] which are key aspects of marine ecology and biogeochemistry.[5] The end goal of investigating the calcite–water interfacial structure was not achieved, but several of the steps along the way, that are necessary for obtaining a detailed picture of the interface, were completed.

At a very rudimentary level, the SFG process occurs in the presence of two overlapping electromagnetic fields to produce a third electromagnetic field oscillating at a frequency that is the sum of the two input field frequencies. But, what happens if there is a fourth electric field present, as is the case when probing a charged interface? Since many mineral–water interfaces carry a charge, an understanding of the effects of this charge upon the SFG process is necessary for interpretation of spectra obtained from the examination of these interfaces. It turns out that one effect of the additional electric field is an emergence of third-order nonlinear optical responses in addition to the second-order responses. In Chapter 3, I develop a model that describes the relative contribution of the second- and third-order responses over a broad range of ionic strengths. I have then analyzed, in the context of the model, the evolution of water structure at both mineral–water and polymer–water interfaces as solution ionic strength is increased.

One of the strengths of the SFG method is the ability to determine the tilt and twist of molecules or functional groups within a molecule through the analysis of spectra collected in different polarization combinations.[6] An additional strength of the method is its ability to resolve bond polarity through the phase of the SFG response. The classic way of retrieving phase information is through interferometry, and in SFG spectroscopy it is no different. There are several established phase-sensitive (PS) SFG methods, each with their own set of strengths.[7–9] Broadband methods allow for rapid data collection, but sacrifice spectral resolution. On the other hand, narrowband, scanning methods yield higher spectral resolution, but require more time for data collection. Our group has focussed on development of narrowband PS-SFG methods. In Chapter 4, I report a PS-SFG technique to simultaneously collect high-precision magnitude and phase spectra and demonstrate its use at an exposed air–solid interface. This theory is expanded to SFG measurement of air–metal interfaces, which behave differently than air–dielectric interfaces.

Of course, in order to measure polar ordering of water at a mineral–water interface PS-SFG methods at a *buried* interface need to be developed. I embarked on this extension of the theory thinking that it would be a relatively straight-forward extension of the exposed PS-SFG methods already developed and refined. I quickly recognized several complexities associated with buried interface PS-SFG that were not initially considered. The challenge of these complexities prevented full development of the method. However, much was learned in the process. In Chapter 6, I describe in detail challenges encountered and possible solutions to those challenges and buried interface PS-SFG in general.

Chapter 2

Background

2.1 Interfaces in the Natural Environment

Chemical gradients and chemical interfaces are ubiquitous in natural systems and an understanding of chemical distribution, fluxes, and transformations cannot be reached without accounting for these gradients and interfaces. Interfaces form the most abrupt example of chemical gradients, where the transition from one phase to the next may occur over extremely short (sub-nanometer) length scales. As such, the chemical potential is often large at interfaces, leading to strong and defining chemical interactions at these locations. Rates of air–sea gas exchange, contaminant transport in groundwater and river systems, and atmospheric chemical transformation are all examples of processes mediated by surface chemistry and the importance of understanding interfacial chemistry and physics of these processes is mirrored by the large volume of literature devoted to each of these topics.

The adsorption of chemical species to a surface may be driven by a variety of forces. These forces may be roughly separated into two classes: short- and long-range forces. Long-range forces include the electrostatic interactions between charged surfaces and adsorbate charge or dipole and van der Waals attraction. Short-range chemical forces include covalent bonding, hydrogen bonding, and hydrophobic effects. Since most naturally occurring surfaces in aquatic systems carry a charge, both classes of interaction need be accounted for when describing adsorption to natural surfaces. Molecular level descriptions of interfacial structure can help identify the type of adsorption interactions present. Extremely well ordered surfaces, such as alkyl-silanes assembled on gold, are achieved through covalent binding to the surface, whereas a loosely ordered, or completely disordered material on the surface may be due to long-range forces.

2.1.1 Mineral–Water Interfaces

Suspended solids in river systems consist of mostly alumino-silicates sourced from erosion and weathering processes and of oxides and carbonates (SiO_2, FeO_x, MnO_x, and $CaCO_3$) precipitated in situ. These solids usually harbor charged surfaces in natural pH ranges, with silica being negatively charged, and the rest of the oxides carrying a positive charge.[10] The exposed surfaces of oxide minerals are generally covered with hydroxyl groups, which may carry a positive charge as $MeOH_2{}^+$ or a negative charge as MeO^-. The protonation state of the oxide surface is largely pH dependent, with the pH at which there is zero charge denoted as the point of zero charge, pH_{pzc}. Surface charge and pH_{pzc} are commonly determined by titration or by electrokinetic mobility. More recently, second-harmonic generation spectroscopy has been utilized to measure surface charge, protonation state and determine interfacial acid-base equilibrium constants.[11] It should be noted that, especially in natural systems, the charge of minerals is not solely dictated by pH. Several studies have shown that mineral surface charge is readily modified through the adsorption of organic matter to the mineral surface, forming a mineral–organic matter–aqueous interface.

For example, in the case of alumina, it has been shown in a controlled, laboratory setting that the adsorption of humic material onto the surface of the bare mineral shifted the surface potential from approximately $30\,\mathrm{mV}$ to around $-30\,\mathrm{mV}$.[12]

2.1.2 Gouy-Chapman and Stern Models of the Interface

The interfaces studied in this thesis may be broadly categorized as mineral–water and polymer–water interfaces. Both, however, may carry a charge in natural environments, so it is necessary to describe briefly qualities of a charged interface. Several models exist to describe charge distribution and electric fields at charged solid–liquid interfaces. Perhaps the most well-known of these is the model of the interface proposed by Gouy in 1910 and Chapman in 1913.[13] This model describes the distribution of charged species in the region adjacent to a surface by an exponential decay function (Figure 2.1). As an example, consider a negatively charged surface in contact with a dilute NaCl solution. Immediately adjacent the surface there is a net depletion of $\mathrm{Cl^-}$ and a net accumulation of $\mathrm{Na^+}$ from bulk concentrations. The interfacial concentrations are determined by the surface potential, Ψ, that decays exponentially with distance from the surface. The characteristic thickness of this layer, termed the *Debye length*, is roughly given (in dilute solutions) by

$$\frac{1}{\kappa} \approx \sqrt{\frac{(0.09\,\mathrm{nm^2\,mol\,L^{-1}})}{I}}, \tag{2.1}$$

where I is the ionic strength of the bulk electrolyte. Notice that the Debye length decreases with increasing ionic strength. This is due to a screening of the surface charge by the mobile charges in solution, thereby decreasing the penetration of Ψ.

Note that the above theory applies in dilute electrolyte solutions ($< 0.1\,\mathrm{mol\,L^{-1}}$) but is not applicable at higher concentrations. At higher electrolyte concentration,

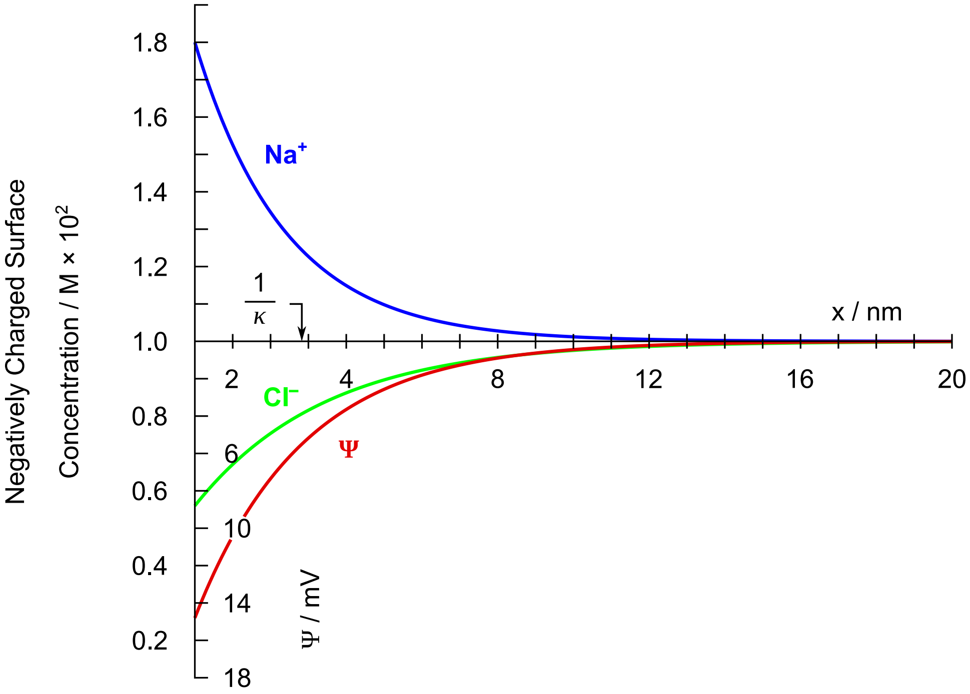

Figure 2.1: Theoretical distributions of ion concentrations and electrical potential near a charged surface. (Calculated for the small potential approximation.) $1/\kappa$ is the thickness of the double layer. Adapted from Morel & Hering, *Principles and Applications of Aquatic Chemistry*, 1993.[14]

the Stern model of the interface is more appropriate. The Stern model considers that the interface is characterized by contact adsorption of the counter ions in solution to the charged surface. The physical size of the ions sets a lower limit on the proximity to the surface that the screening charges can inhabit. This means that the surface may be, at high electrolyte concentrations, modelled as a capacitor, two charged plates separated by a finite distance. In the context of work presented in this thesis, the important difference between the Stern and Gouy-Chapman models is that the potential drop between the charged plates is linear, rather than exponential.

2.2 Probing Interfacial Structure

2.2.1 Surface Spectroscopy

Many techniques exist to measure surface and interface properties. First-order (linear in field strength) optical techniques such as attenuated total reflection IR and glancing angle Raman methods achieve their surface specificity through geometric constraints. The penetration depth of the evanescent wave in the IR technique depends upon incident angle and material refractive index. At solid–liquid interfaces this depth is typically on the order of 0.5 to 1.5 µm. The penetration depth of total internal reflection Raman techniques is considerably shorter. For example, in an examination of leaf waxes by total internal reflection Raman with 532 nm light, penetration depth was 40 nm, enabling the wax to be probed without interference from underlying pigments.[15] Glancing angle Raman methods used to examine air–water and air–ice interfaces have similar surface specificity (approx 50 nm).[16,17]

Polarization modulated infrared reflection absorption relies on a rapid switching of the incident beam polarization from s- to p- linear state to detect differential reflectivities of the infrared source from the sample surface.[18,19] Adsorption of the IR by isotropic species in the beam path is not affected by the polarization modulation, meaning that the difference spectrum is isolated to the surface.

In contrast to the linear optical methods, second-order optical techniques derive their surface specificity from symmetry rather than geometric constraints. Second-order processes are only observed in non-centrosymmetric environments, which includes interfaces. One benefit of this specificity is that chemical species at an interface may be probed while ignoring all forms of the species in bulk environments.

2.2.2 Nonlinear Optical Spectroscopy and Sum-Frequency Generation

Two forms of nonlinear optical spectroscopies commonly used to probe interfacial structure are electronic second harmonic generation (SHG) and vibrational sum-frequency generation (SFG) spectroscopy. These two techniques are related in that SHG is the degenerate analog of SFG, but they are typically used to probe different surface properties. SHG methods commonly employ a visible source to probe electronic transitions at the interface, while SFG methods typically combine visible and infrared sources to observe vibrational transitions. At its most basic implementation, SFG can be used as a probe to determine whether or not an adsorption process has occurred. Quantitative SFG methods allow for the measurement of adsorption isotherms and thermodynamic properties.[20] Control of the polarization of excitation sources and detected signal enables detailed analysis of interfacial molecular structure, including bond angles, twist, and tilt.[21] In the following section, details of the theory of SFG are presented, along with specifics pertaining to the equipment in our lab. This is not meant to be a comprehensive treatment of nonlinear optics,[6,22] but just enough to provide the background necessary for an understanding of subsequent chapters in this thesis.

Nonlinear optical phenomena are observable when a material is exposed to a large, electromagnetic field ($\mathbf{E}$). Within the material, the molecular dipoles, μ, are induced by the incident field such that

$$\mu = \mu_0 + \alpha^{(1)}\mathbf{E} + \alpha^{(2)}\mathbf{EE} + \alpha^{(3)}\mathbf{EEE} + \cdots , \tag{2.2}$$

where μ_0 is the permanent dipole and $\alpha^{(n)}$ are the molecular polarizabilities (*hyperpolarizability* is commonly used to describe higher order cases of polarizability). The

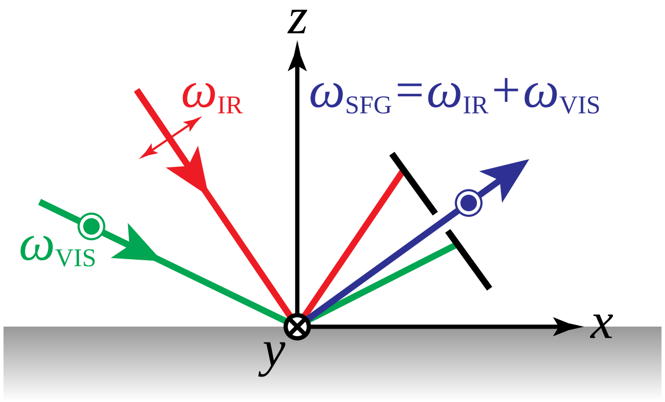

Figure 2.2: The geometry of co-propagating beams in an SFG reflection experiment. Visible and infrared beams with frequencies ω_{vis} and ω_{IR} overlap in time and space at the sample interface. In a non-collinear geometry, the SFG response may be spatially separated from the reflected incident beams prior to reaching the detector.

induced dipole is the *molecular* response to the applied electric field. The *material* response to the applied electric field is the induced polarization, $\mathbf{P}^{(n)}$. The induced polarization may be described in a form analagous to the induced dipole,

$$\mathbf{P} = \varepsilon_0 \left(\chi^{(1)}\mathbf{E} + \chi^{(2)}\mathbf{EE} + \chi^{(3)}\mathbf{EEE} + \cdots \right), \tag{2.3}$$

where ε_0 is the permittivity of free space and $\chi^{(n)}$ are functions of $\alpha^{(n)}$. Since SFG and SHG are second-order processes, they depend only upon the $\chi^{(2)}$ term in Eq. 2.3.

Sum-frequency generation (SFG) occurs when two electric fields are simultaneously incident upon the material (Figure 2.2). The combined electric field may be described as the sum of the two incident fields, $\mathbf{E}_1$ and $\mathbf{E}_2$, of frequencies ω_1 and ω_2, which, when expanded, yields the following expression

$$\begin{aligned} \mathbf{E} &= \mathbf{E}_1 \cos \omega_1 t + \mathbf{E}_2 \cos \omega_2 t \\ &= \mathbf{E}_1^2 + \mathbf{E}_2^2 + \mathbf{E}_1^2 \cos 2\omega_1 t + \mathbf{E}_2^2 \cos 2\omega_2 t \\ &\quad + \frac{1}{2}\mathbf{E}_1\mathbf{E}_2 \cos(\omega_1 - \omega_2)t + \frac{1}{2}\mathbf{E}_1\mathbf{E}_2 \cos(\omega_1 + \omega_2)t \end{aligned} \tag{2.4}$$

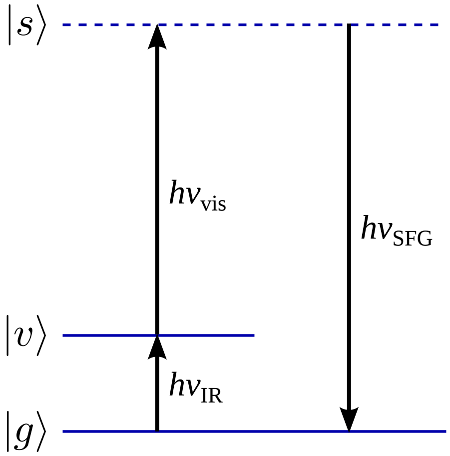

Figure 2.3: Energy level diagram of the sum-frequency generation process. The sum-frequency process occurs when an anti-Stokes Raman transition ($h\nu_{\text{vis}}$ followed by $h\nu_{\text{SFG}}$) to the ground state ($|g\rangle$) occurs starting from an excited vibrational state ($|v\rangle$). This can only occur if the transition measured is both infrared and Raman active.

consisting of two static electric fields, two second harmonic ($2\omega_1$ and $2\omega_2$) fields, a difference-frequency ($\omega_1 - \omega_2$) term and the sum-frequency ($\omega_1 + \omega_2$) term. In vibrational SFG, the induced sum-frequency polarization is therefore

$$\mathbf{P}^{(2)}_{\text{SFG}} = \varepsilon_0 \chi^{(2)} \mathbf{E}_{\text{vis}} \mathbf{E}_{\text{IR}}. \tag{2.5}$$

The energy diagram in Figure 2.3 illustrates the vibrational and electronic transitions involved in the SFG process. It may be thought of as an infrared transition to an excited vibrational state, $|v\rangle$, and simultaneous anti-Stokes Raman transition to the ground state, $|g\rangle$. This means, that for the vibrational mode to be visible by SFG spectroscopy, it must be both IR and Raman active, and its amplitude is proportional to the product of IR and Raman transition intensities. The second-order hyperpolarizability and the IR and Raman transitions ($\frac{\partial \mu_n}{\partial Q}$ and $\frac{\partial \alpha^{(1)}_{lm}}{\partial Q}$, respectively) are related in the molecular frame by

$$\alpha^{(2)}_{lmn}(\omega_{\mathrm{IR}}) = \sum_n \left(\frac{1}{2m_n\omega_n}\right)\left(\frac{1}{\omega_n - \omega_{\mathrm{IR}} - i\Gamma_n}\right)\left(\frac{\partial\alpha^{(1)}_{lm}}{\partial Q}\right)_n\left(\frac{\partial\mu_n}{\partial Q}\right)_n, \qquad (2.6)$$

where lmn define the coordinates in the molecular frame, m_n is the reduced mass and Γ_n is the width of the nth vibrational mode. In the lab frame of reference, the measured response is proportional to the ensemble average of the molecular response,

$$\chi^{(2)}_{ijk} = \frac{1}{\varepsilon_0}\sum_N \alpha^{(2)}_{ijk} = \frac{N}{\varepsilon_0}\langle\alpha^{(2)}_{ijk}\rangle, \qquad (2.7)$$

where $\langle\alpha^{(2)}_{ijk}\rangle$ is the ensemble average, over N molecules. The indices ijk specify lab frame cartesian coordinates of the response.

The quantity $\chi^{(2)}$ as shown here relates the induced polarization along a given axis in the lab frame to the polarizations of the two incident beams. As such, $\chi^{(2)}$ is a 27 element tensor, relating all the possible combinations of beam polarizations. It also possesses the symmetry constraint that for any element of the $\chi^{(2)}$ tensor to be non-zero the local environment must be non-centrosymmetric. This condition leads to the inherent surface specificity of the sum-frequency process; the average environment in most bulk media is centrosymmetric, whereas by definition, an interface creates a break in symmetry.

The measured sum-frequency response from a material is the sum of all the individual vibrational modes over the IR range measured

$$I_{\mathrm{SFG}} \propto \left|\chi^{(2)}_{\mathrm{NR},ijk} + \sum_n \chi^{(2)}_{n,ijk}\right|^2 = \left|\chi^{(2)}_{\mathrm{NR},ijk} + \sum_n \frac{A_n}{\omega_n - \omega_{\mathrm{IR}} - i\Gamma_n}\right|^2, \qquad (2.8)$$

where $\chi^{(2)}_{\mathrm{NR}}$ is the non-resonant response, n represents the individual vibrational modes contributing to the total, A_n is the magnitude of the transition polarizability, ω_{IR} is the IR energy, ω_n is the vibrational resonance energy, Γ_n is a line broadening term, and $i = \sqrt{-1}$.

In the case of simple molecules, especially those with resonances associated with a unique functional group, and if care is taken to properly calibrate the response under different polarization schemes, the spectra can be fit to Eq. 2.8 and the transition dipole angles with respect to the surface normal may be calculated. For larger molecules with many vibrational modes it becomes impossible to deconvolute the measured spectrum into each of the component modes. In this case, spectral interpretation may be aided by molecular dynamics simulations.[23]

2.2.3 Phase-Sensitive SFG

I have already discussed the inherent surface specificity of the sum-frequency technique, driven by the requirement of a non-centrosymmetric molecular arrangement. Analysis of carefully calibrated data allows for the molecular level orientation of chemical species at an interface to be determined. Since generation of an SFG response requires the absence of a centrosymmetric molecular organization (resulting in the nonlinear susceptibility $\chi^{(2)} \neq 0$), the experiment is capable of probing the polarity of chemical bonds (e.g. the direction in which the bonds are pointing may be resolved in an absolute sense), in addition to characterizing their tilt angle with respect to the surface.[7,24,25] However, since a standard (non-phase-resolved, homodyne) SFG detection scheme measures a signal proportional to $|\chi^{(2)}|^2$, it is incapable of determining a switch in the polarity of a single peak which is encoded as a 180° change in the phase of $\chi^{(2)}$. Given sufficiently high spectral resolution, the ambiguity may be minimized by careful inspection of the interference with neighboring peaks in the intensity spectrum.[26] A measurement of the signal phase would eliminate this ambiguity. This is one of the motivations for the development of phase-sensitive SFG experiments.[7,8,24,27–37]

In the case of degenerate techniques (both pump photons having the same frequency) such as SHG spectroscopy, phase measurements have been performed for decades[38–48] and the theory behind the phase measurements has been described in some detail.[49,50] More recently, methods have been developed to measure SFG signal phase in both broadband (femtosecond)[8] and narrow-band (picosecond)[7] regimes. Both methods capture the phase by interfering the sample signal with another signal of known phase, termed the local oscillator. Modulation of the difference in phase between the two signals is most commonly accomplished by passing one of the signals through a thin prism.

In our lab, PS-SFG experiments are performed in the narrowband, wavelength scanning regime. The basis of the phase measurement is to monitor the intensity of the signal I_{SFG} when the SFG field from the sample $\mathbf{E}_{\mathrm{S}}$ and the local oscillator (LO) at the same frequency $\mathbf{E}_{\mathrm{LO}}$ are brought to coincide. The interference of the two beams can be described by

$$\begin{aligned} I_{\mathrm{SFG}} &= |\mathbf{E}_{\mathrm{S}} + \mathbf{E}_{\mathrm{LO}}|^2 \\ &= |\mathbf{E}_{\mathrm{S}}|^2 + |\mathbf{E}_{\mathrm{LO}}|^2 + 2|\mathbf{E}_{\mathrm{S}}||\mathbf{E}_{\mathrm{LO}}|\cos\Delta\varphi \end{aligned} \tag{2.9}$$

where $\Delta\varphi$ is the phase difference between sample and local oscillator SFG fields. The phase-shifting unit (PSU) employed in our experiment modulates $\Delta\varphi$ according to its tilt angle, α, the angle of incidence of the three collinear beams emerging from the local oscillator. Reformulation of Eq. 2.9 as

$$I_{\mathrm{SFG}}(\alpha,\omega) = a(\alpha,\omega) + b(\alpha,\omega)\cos\Delta\varphi(\alpha,\omega), \tag{2.10}$$

where $a \propto |\mathbf{E}_{\mathrm{S}}|^2 + |\mathbf{E}_{\mathrm{LO}}|^2$, $b \propto 2|\mathbf{E}_{\mathrm{S}}||\mathbf{E}_{\mathrm{LO}}|$, and ω refers to the frequencies of all three beams, allows us to relate the measured intensities to three functions of α and ω.

The phase term $\Delta\varphi$ in Eqs. 2.9 and 2.10 can be separated into individual components relating to the PSU, the focusing lens, and the $\chi^{(2)}$ phases of the sample φ_{S} and local oscillator φ_{LO}. Defining $\Delta\varphi_{\mathrm{S\cdot LO}}$ as the difference between the two $\chi^{(2)}$ phases leads to the expression

$$\Delta\varphi(\alpha,\omega) = \Delta\varphi_{\mathrm{PSU}}(\alpha,\omega) + \Delta\varphi_{\mathrm{lens}}(\omega) - \Delta\varphi_{\mathrm{S\cdot LO}}(\omega). \tag{2.11}$$

The phase shifts imparted by the PSU and lens result from a difference in the optical path lengths (OPL) through these optics caused by dispersion of the refractive index. For the lens, whose position is static, the phase shift is

$$\Delta\varphi_{\mathrm{lens}}(\omega) = \frac{d_{\mathrm{lens}}}{c}\left(n_{\mathrm{lens}}\left(\omega_{\mathrm{SFG}}\right)\omega_{\mathrm{SFG}} - n_{\mathrm{lens}}\left(\omega_{\mathrm{vis}}\right)\omega_{\mathrm{vis}} - n_{\mathrm{lens}}\left(\omega_{\mathrm{IR}}\right)\omega_{\mathrm{IR}}\right), \tag{2.12}$$

where d_{lens} is the thickness of the lens at its center, c is the speed of light in a vacuum, and $n_{\mathrm{lens}}(\omega)$ defines the refractive index of the lens material. The phase-shift by the PSU may be calculated in an analogous fashion, with the exception that the rotation angle (α) of the PSU must now be accounted for. This is readily accomplished by calculating the refracted angles (β) of the beams within the PSU using Snell's law

$$\beta(\alpha,\omega_i) = \arcsin\left(\frac{n_{\mathrm{air}}(\omega_i)}{n_{\mathrm{PSU}}(\omega_i)}\sin\alpha\right). \tag{2.13}$$

Incorporation into the phase-shift equation yields

$$\begin{aligned}\Delta\varphi_{\mathrm{PSU}}(\alpha,\omega) =& \frac{d_{\mathrm{PSU}}}{c}\left(n_{\mathrm{PSU}}\left(\omega_{\mathrm{SFG}}\right)\omega_{\mathrm{SFG}}\cos\beta(\alpha,\omega_{\mathrm{SFG}})\right.\\ &- n_{\mathrm{PSU}}\left(\omega_{\mathrm{vis}}\right)\omega_{\mathrm{vis}}\cos\beta(\alpha,\omega_{\mathrm{vis}})\\ &\left.- n_{\mathrm{PSU}}\left(\omega_{\mathrm{IR}}\right)\omega_{\mathrm{IR}}\cos\beta(\alpha,\omega_{\mathrm{IR}})\right).\end{aligned} \tag{2.14}$$

An additional factor in the model of the fringe shape is the variation in transmittance of the fields through the PSU as it rotates. This may be modelled as the product of two Fresnel coefficients of transmission across the air–PSU interface and the PSU–air interface:

$$(tt)(\alpha,\omega) = t_{\mathrm{air,PSU}}(\alpha,\omega) \cdot t_{\mathrm{PSU,air}}(\alpha,\omega). \tag{2.15}$$

The value of $(tt)(\alpha,\omega)$ decreases as tilt angle, α, increases, resulting in diminished fringe intensity at the outside edges. It is now possible to create expressions for a and b in Eq. 2.10. These are

$$a(\alpha,\omega) = |(tt)(\alpha,\omega_{\mathrm{SFG}})|^2 + f^2|(tt)(\alpha,\omega_{\mathrm{vis}})(tt)(\alpha,\omega_{\mathrm{IR}})|^2 \tag{2.16}$$

$$b(\alpha,\omega) = 2f|(tt)(\alpha,\omega_{\mathrm{SFG}})(tt)(\alpha,\omega_{\mathrm{vis}})(tt)(\alpha,\omega_{\mathrm{IR}})|, \tag{2.17}$$

where f is the ratio of the sample to local oscillator field magnitudes ($f = |\mathbf{E}_{\mathrm{S}}|/|\mathbf{E}_{\mathrm{LO}}|$). The effect of differing fringe visibility is demonstrated by varying f. The solid line in Figure 2.4a illustrates the ideal case of maximum fringe visibility with $f = 1$. Here, all the fringes have nearly equal intensity at their minima, and their maxima are only slightly diminished at large angles α. (Note that the interference patterns have all been scaled from zero to unity, so offsets from zero are not displayed. This best reflects the situation in an experiment where the shape of the fringes is analyzed after a potentially large background is subtracted.) Varying the relative amplitude of the two SFG signals has a significant affect on the predicted interference pattern (wide dashed line has $f = 0.05$, narrow dashed line has $f = 0.02$, and dotted line has $f = 0.01$) as it becomes overlaid on an arc. Although Fresnel corrections to tilt-operation phase-shifting units are frequently ignored when measuring phase shifts, they are very prominent at reduced fringe visibility. Figure 2.4b shows data obtained

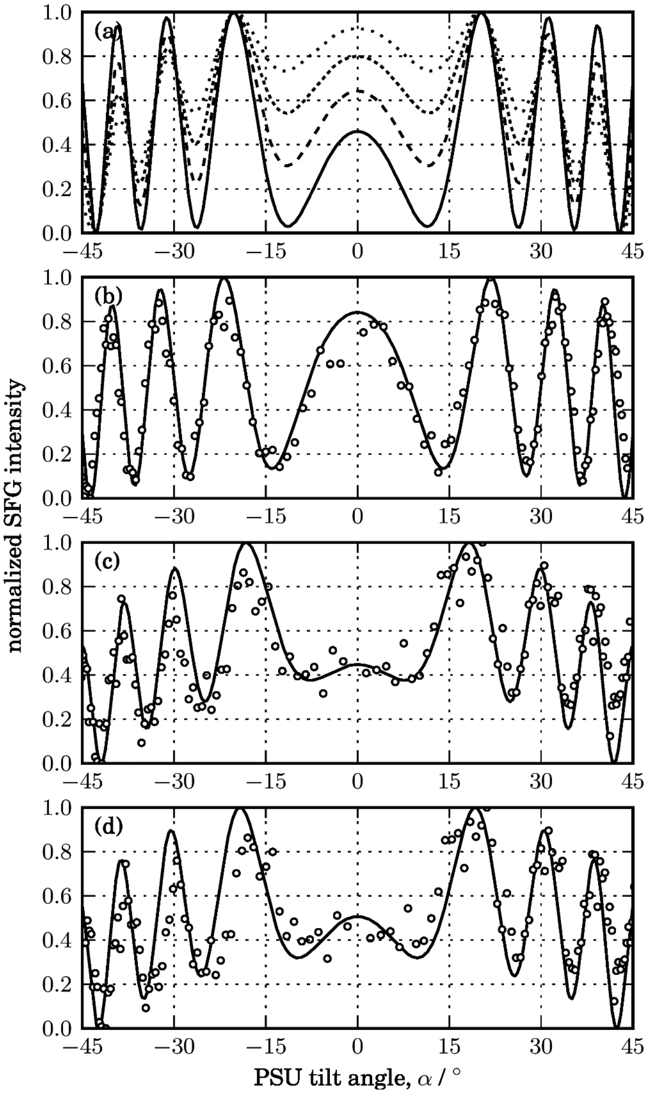

Figure 2.4: Effect of the fringe visibility on the observed SFG intensity as a function of PSU tilt angle. (a) Simulations of $\Delta\varphi = 0°$ at $\omega_{\mathrm{IR}} = 2900\,\mathrm{cm}^{-1}$ with $f = 1$ solid line; $f = 0.05$ wide dashed line; $f = 0.02$ narrow dashed line; $f = 0.01$ dotted line. (b) Experimental measurement of α-quartz at $\omega_{\mathrm{IR}} = 2950\,\mathrm{cm}^{-1}$ (circles); fit to Eq. (2) with $f = 0.143$, $\Delta\varphi = 24.5°$. (c) Experimental measurement of an OTS monolayer at $\omega_{\mathrm{IR}} = 2868\,\mathrm{cm}^{-1}$ (circles); fit to Eq. (2) with $f = 0.0357$, $\Delta\varphi = 327°$. (d) Same OTS sample at $\omega_{\mathrm{IR}} = 2875\,\mathrm{cm}^{-1}$ with $f = 0.0460$, $\Delta\varphi = 347°$.

by reflecting off a z-cut α-quartz sample at $\omega_{\mathrm{IR}} = 2950\,\mathrm{cm}^{-1}$. The fit returned $f = 0.143$, indicating that the LO SFG signal was $1/f\sqrt{\approx 50}$ times greater than that of the sample, in agreement with our measurements of the intensities of the two separate signals. Figures 2.4c and d show fringes collected from octadecyltrichlorosilane (OTS) monolayer on glass. Interference fringes obtained at $\omega_{\mathrm{IR}} = 2868\,\mathrm{cm}^{-1}$, just below the methyl symmetric stretch, were fit with a value of $f = 0.0357$, which indicates that the LO is $\approx$ 800 times greater than the SFG signal from the monolayer. On resonance at $\omega_{\mathrm{IR}} = 2875\,\mathrm{cm}^{-1}$, the local oscillator signal is about 470 times stronger than the monolayer signal $f = 0.0460$. We have chosen these examples since SFG from monolayers is weak, even near resonance, and z-cut quartz is often used as a calibration standard.

In nonlinear optical phase measurements, it is generally desired to avoid dispersive elements such as lenses in the beam path between the LO and the sample. However, there are situations that require this configuration, such as studies of buried solid–liquid interfaces where the pump beams must approach the interface through a window or prism. This optic has a large consequence on the measurement, as illustrated in Figure 2.5, where the same fringe model parameters are plotted, except that $d_{\mathrm{lens}} = 0$ in Figure 2.5b. Here the temporal interference is still evident, but the spectral interference profile has an extremely long period. This is most clear in the right side panel where the normalized trace through the vertical cross hair is plotted. It is interesting to note that a nearly identical image was obtained (not shown) with the introduction of 4 mm of fused silica in the beam path. Only when the lens material was changed to $\mathrm{BaF_2}$ was I able to arrive at Figure 2.5a. This draws attention to the criticality of the refractive index of the phase-shifting optics and their dispersion profiles.

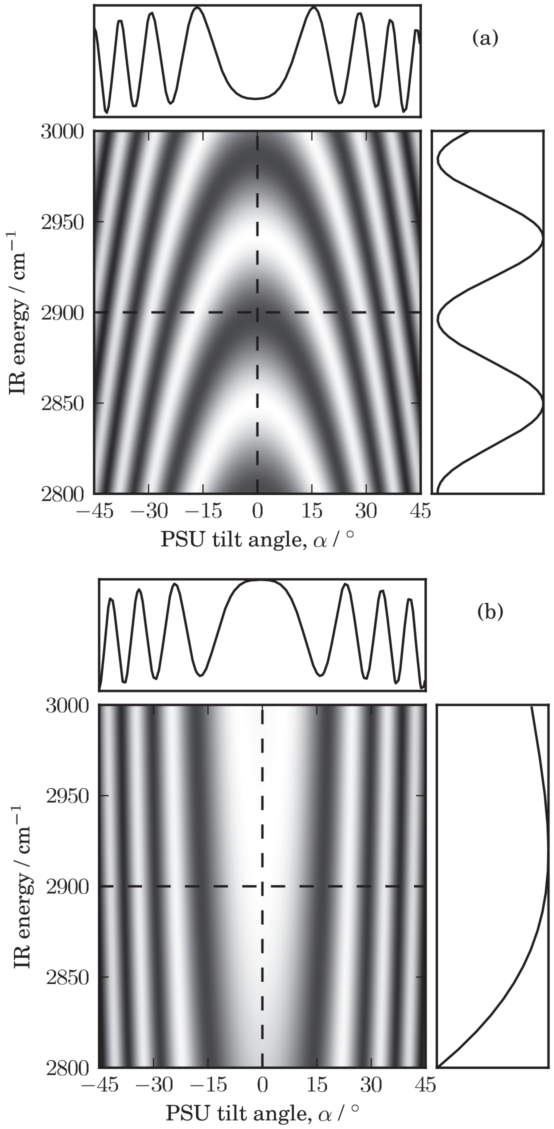

Figure 2.5: (a) Simulation of interference fringe using Eq. 2.9, simultaneously considering the temporal and spectral interferences. Results are plotted for $d_{\mathrm{PSU}} = 0.993\,\mathrm{mm}$, $d_{\mathrm{lens}} = 3.84\,\mathrm{mm}$, and $\Delta\varphi_{\mathrm{S \cdot LO}} = 29°$. (b) The result of a simulation with no lens present, but all other parameters the same.

Chapter 3

Influence of Electrolytes Upon Interfacial Water Structure

Reproduced in part from Jena, K.; Covert, P.; Hore, D. "The effect of salt on the water structure at a charged solid surface: differentiating second-and third-order nonlinear contributions." *J. Phys. Chem. Lett.,* **2,** 1056 (2011) and Covert, P.; Jena, K.; Hore, D. "Throwing Salt into the Mix: Altering Interfacial Water Structure by Electrolyte Addition." *J. Phys. Chem. Lett.,* **5,** 143 (2013). Copyright 2011, 2013 American Chemical Society. All data collection, including preparation of surfaces and solutions, and measurement of SFG spectra performed by Kailash Jena. Treatment of data, model development, and analysis of data from multiple interfaces done by Paul Covert.

3.1 Introduction

The role of ions is crucial in screening electrostatic fields at charged solid interfaces and creating electric double layers at air–water interfaces.[11,51–56]. As a result, many studies seek to address questions about the depth to which water molecules are ordered, electrolyte contribution to the development or to the screening of the surface field, and the amount to which contact adsorption of ions significantly disturbs interfacial solvent structure. The answers to these questions have a profound impact on the subsequent adsorption, orientation, and conformation of molecules at charged interfaces.

Recently, there have been many experimental and computational approaches addressing the issue of water structure at solid surfaces.[11,30,51–54,56–64] Among these studies, there has been some controversy surrounding the distance over which water is ordered at a charged surface. For example, X-ray scattering[61–64] and molecular dynamics simulations[65–68] indicate that structured water exists no further than approximately 1 nm from the surface. On the other hand, data from nonlinear optical[54,60,69] and atomic force measurements[70] have suggested that water molecules may be structured up to the Debye length. Nonlinear optical spectroscopies such as electronic second harmonic generation (SHG)[71–79] and electronic/vibrational sum-frequency generation (SFG)[6,80–87] are particularly attractive for such investigations since, in the simplest case, the signals are expected to be dipole-forbidden for any molecules that are not structured in a polar manner. They therefore offer extreme sensitivity to interfaces, without relying on shallow bulk penetration of the beams. Vibrational SFG in particular has been used to study water structure as a function of electrolyte composition and concentration.[29,52,55,56,69,87–94] However, when these techniques are applied to charged interfaces, care must be taken in the interpretation of the measured signals. At a charged surface, the presence of a strong electrostatic field at the interface acts as a third input field with zero frequency. In this chapter I examine how second- and third-order contributions to the electric susceptibility manifest themselves in the SFG signal as a function of ionic strength. By comparing data obtained over a wide range of salt concentrations, I have been able to develop a model of SFG response coupled with interfacial water structure at the fused silica–water interface, providing new insight into the interfacial water structure and reconcile previous results from the literature. Furthermore, the insight derived from this model was used to describe interfacial water structure and charge buildup at a variety of other surfaces, polymer and mineral, with increasing electrolyte concentration.

3.2 Experimental Methods

3.2.1 Surface Preparation

Prior to each experiment, IR-grade fused silica and calcium fluoride dove prisms (Del Mar Photonics, CA) were immersed in a concentrated solution of sulfuric acid containing 0.1 % nitric acid to remove all traces of organic contamination, thoroughly rinsed with 18 MΩ cm water (Nanopure, Barnstead Thermo), and placed in a drying oven for several hours to remove all water. Polymer surfaces were applied to the back side of cleaned CaF_2 prisms by spin coating (90 s; 1500 rpm; Model G3-8, Specialty Coating Systems, IN) from a polymer/chloroform solution. Polystyrene solutions were composed of 3 wt %/wt deuterated d_8-polystyrene (molecular weight 270 500 $\mathrm{g\,mol^{-1}}$, PDI 1.25 from Polymer Source, QC) in chloroform. Poly(methyl methacrylate) (PMMA) films were prepared from 2 wt %/wt d_8-PMMA (molecular weight 35 000 $\mathrm{g\,mol^{-1}}$, Scientific Polymer Products NY) in chloroform. Film thicknesses were on the order of 100 nm.

3.2.2 Solution Preparation

Salt solutions spanning a concentration range of 0.1 $\mathrm{mmol\,L^{-1}}$ to 4 $\mathrm{mol\,L^{-1}}$ were prepared by dissolution of NaCl (ACP, Montreal Canada) in 18 MΩ cm water (Nanopure, Barnstead Thermo). The measured pH of the salt solutions was 6.0 ± 0.1, slightly more acidic than neutral water. Deviation from neutral pH was most likely due to equilibration with atmospheric CO_2, as the samples were not kept in an inert environment.

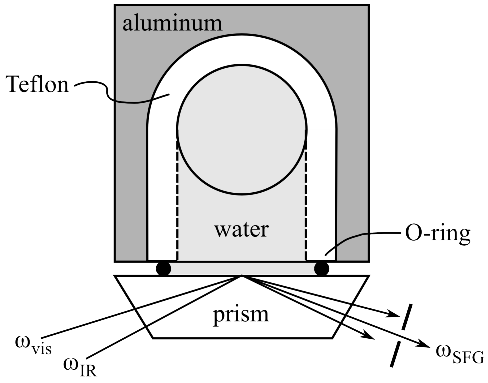

Figure 3.1: Detailed view of the experimental geometry used for solid–salt solution experiments. A Teflon cell inside an aluminum block contains the salt water solutions. The solution–solid interface consists of a bare or polymer-coated fused silica or fluorite prism connected to the Teflon cell by a fluoropolymer O-ring. Beams enter the prism and then reflect from the solution–prism interface.

3.2.3 SFG measurement

A 1064 nm Nd:YAG laser with 25 ps pulse width and 10 Hz repetition rate (Ekspla PL241) was frequency doubled for use as the visible pump beam ($\bar{\nu}_{\text{vis}}$). The same laser provided the input to the BBO/$AgGaS_2$-based OPA/OPG/DFG (Ekspla PG501), used to create a tunable infrared pump beam ($\bar{\nu}_{\text{IR}}$=2750–3750 cm^{-1}, 5 cm^{-1} step size). The visible beam approached the solid–liquid interface from the solid side at an incident angle of 66°, was focused to a diameter of 1 mm, and had an energy of 110 µJ/pulse. The infrared beam also approached the interface from the solid side, had an angle of incidence of 63°, beam diameter of 0.5 mm, and an energy of 200 µJ/pulse at 3000 cm^{-1}. In this geometry, total internal reflection was achieved for all beams. All spectra for this study were collected with p-polarized infrared and s-polarized visible beams incident at the interface; the s-component of the SFG response was recorded as a function of infrared energy. As shown in Figure 3.1, the sample prism is clamped to a Teflon water cell with a fluoropolymer O-ring (Marco Rubber, NH) creating a water-tight seal.

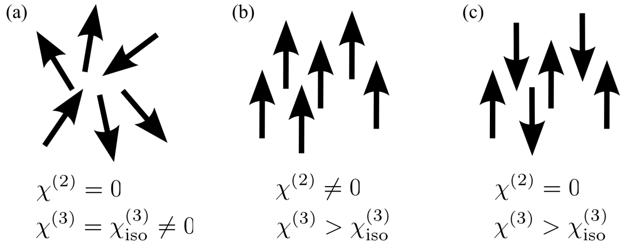

Figure 3.2: An illustration of the relationship between $\chi^{(2)}$ and $\chi^{(3)}$ in (a) isotropic, (b) polar ordered, and (c) non-polar ordered environments. Arrows indicate the direction of the water dipoles.

3.3 Fused Silica–Solution Interface

In SHG and SFG experiments at neutral interfaces, signal is understood to result from the second-order susceptibility $\chi^{(2)}$. However, it has been observed that the SHG signal can be enhanced by applying a DC electric field, and this has been attributed to the contribution of the third-order susceptibility $\chi^{(3)}$.[95,96] The above process is known as electric field induced second harmonic (EFISH) generation. In non-collinear geometries, the $\chi^{(2)}$ and $\chi^{(3)}$ signals have different phase-matching directions and so are easily distinguished.[6,97] However, since the $\chi^{(3)}$ contribution in EFISH comes from a static field $\mathbf{E}_0$, $\chi^{(2)}$ and $\chi^{(3)}$ signals are simultaneously detected as

$$I_{\text{SFG}} \propto |\chi^{(2)}\mathbf{E}_{\text{vis}}\mathbf{E}_{\text{IR}} + \chi^{(3)}\mathbf{E}_{\text{vis}}\mathbf{E}_{\text{IR}}\mathbf{E}_0|^2. \tag{3.1}$$

Here the $\chi^{(2)}$ signal originates from those molecules that are asymmetrically orientated at the interface. The $\chi^{(3)}$ signal has contributions from isotropic bulk water molecules ($\chi^{(3)}_{\text{iso}}$) and from oriented molecules due to the static electric field.[11,98] Figure 3.2a illustrates that, under the electric dipole approximation, $\chi^{(2)} \propto N^{(2)}\langle\alpha^{(2)}\rangle = 0$ in centrosymmetric environments, where $\alpha^{(2)}$ is the second-order molecular polarizability. In contrast $\chi^{(3)} \propto N^{(3)}\langle\alpha^{(3)}\rangle = \chi^{(3)}_{\text{iso}} \neq 0$, where $\alpha^{(3)}$ is the third-order molecular polarizability. Here $N^{(2)}$ refers to those molecules with a net polar (non-centrosymmetric) orientation, and $N^{(3)}$ refers to all molecules experiencing the surface-originating field $\mathbf{E}_0$, regardless of whether they are aligned. It is emphasized that while the second-order susceptibility requires a polar orientation of water molecules, the third-order susceptibility is merely enhanced from its isotropic value when water molecules are oriented (Figure 3.2b). Figure 3.2c illustrates that, even when there is a high degree of orientational order, $\chi^{(2)} = 0$ in the absence of polarity since this again represents a centrosymmetric environment.

The field present at aqueous–oxide interfaces and its interaction with water dipoles has been well-studied, and is understood to promote ordering of water molecules at the interface.[11,51,52,55,56,69,87,99,100] In studies of the fused silica–water interface, Ong et al. performed a thorough investigation in which they varied the solution pH, ionic strength, and temperature of the solution.[11] Among their conclusions, their observation of an enhanced SHG signal attributed to an intrinsic interfacial electric field $\mathbf{E}_0$ is of central interest to this work. Du et al. studied the quartz–water interface using vibrationally-resonant SFG spectroscopy.[51] At pH values corresponding to a charged quartz surface, the addition of salt was observed to lower the SFG intensity. At neutral pH there was no change in the water structure, even at NaCl concentrations as high as $0.5\,\mathrm{mol\,L^{-1}}$. Considering this surface-originating field and its interaction with water molecules, Yeganeh et al. used SFG to measure the isoelectric point of Al_2O_3–water interfaces by varying the pH of the solution.[87] Similarly, Gragson and Richmond studied the molecular alignment and hydrogen bonding at charged air–water and CCl_4–water interfaces as a function of surface charge density, ionic strength, and temperature.[54] Eftekhari-Bafrooei and Borguet compared the OH vibrational lifetime at a neutral and a charged silica surface.[69] A shorter lifetime at the charged surface was attributed to a greater number of solvation shells available for energy dissipation in a deeper interfacial region. In all of the above studies, the presence of $\mathbf{E}_0$ at a

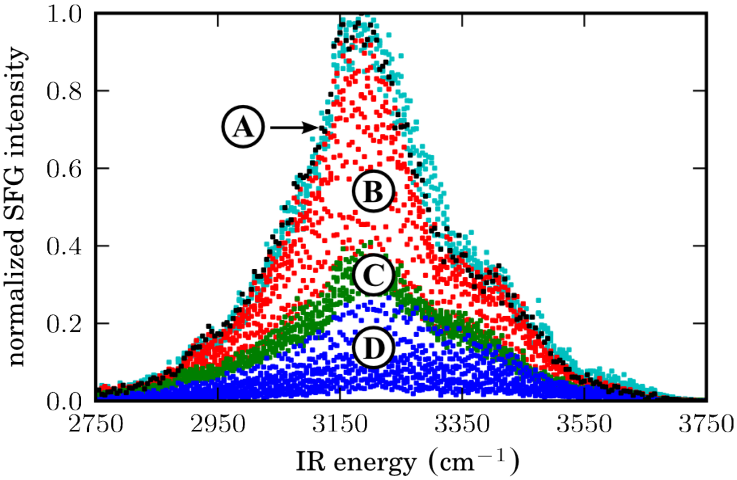

Figure 3.3: Sum-frequency response from the fused silica–solution interface as a function of ionic strength. The black spectrum corresponds to the pure fused silica–water interface at pH 6, before any salt addition. Spectra in series A (cyan) correspond to dilute ($4.8 \times 10^{-5}\,\mathrm{mol\,L^{-1}}$ to $4.7 \times 10^{-4}\,\mathrm{mol\,L^{-1}}$) NaCl solutions; series B (red) $9.2 \times 10^{-4}\,\mathrm{mol\,L^{-1}}$ to $4.7 \times 10^{-2}\,\mathrm{mol\,L^{-1}}$; series C (green) $0.13\,\mathrm{mol\,L^{-1}}$ to $1.1\,\mathrm{mol\,L^{-1}}$; series D (blue) $1.7\,\mathrm{mol\,L^{-1}}$ to $4.1\,\mathrm{mol\,L^{-1}}$ NaCl.

charged surface results in a greater depth over which water molecules are aligned, an increased orientation of interfacial water, and a $\chi^{(3)}$ contribution to the signal. However, the relative contribution of $\chi^{(2)}$ and $\chi^{(3)}$ to the observed spectra is still an open question.

3.3.1 Evolution of Water Spectra

From our data over a wide range of ionic strengths, several regimes were identified that reveal the depth over which molecules respond to electrolyte addition, the balance between charge development and screening, and the relative contribution of second- and third-order optical nonlinearities to the spectral response.

Figure 3.3 shows SFG spectra of the fused silica–water interface at various ionic strengths. The black spectrum corresponds to the neat interface, before any salt addition. A plot of integrated SFG intensity, normalized with respect to the neat water spectrum, is shown in Figure 3.4.

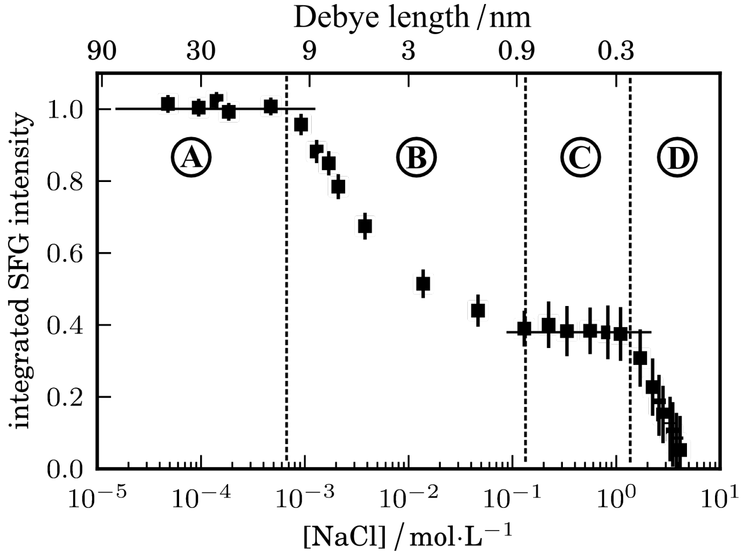

Figure 3.4: Integrated intensity of all spectra shown in Figure 3.3, normalized with respect to the one acquired before salt addition. The top axis is drawn according to Eq. 3.2.

In the discussion of physical and chemical processes responsible for the trends in the data shown in Figure 3.4 two models of interfacial charge distribution are considered. At low ionic strength, the Gouy-Chapman diffuse charge model[54,102,103] describes the distribution of ionic species in the vicinity of a charged surface. The Debye length, which results from this model, describes the extent to which the electrolyte screens the surface field and may be calculated as

$$\kappa^{-1} = \sqrt{\frac{\varepsilon\varepsilon_0 RT}{2F^2 I}} \approx \sqrt{\frac{(0.09\,\mathrm{nm}^2\,\mathrm{mol}\,\mathrm{L}^{-1})}{I}}, \tag{3.2}$$

where ε is the relative dielectric constant of water, F is the Faraday constant, R is the universal gas constant, T is the absolute temperature, and ε_0 is the permittivity of free space. Values of κ^{-1} obtained from this relationship are indicated in the top axis of Figure 3.4. At high ionic strengths (greater than $0.13\,\mathrm{mol}\,\mathrm{L}^{-1}$) the surface charge reaches a level where the Gouy-Chapman model is no longer suitable and the Stern model is the more appropriate model of the interface. In this model, the interfacial

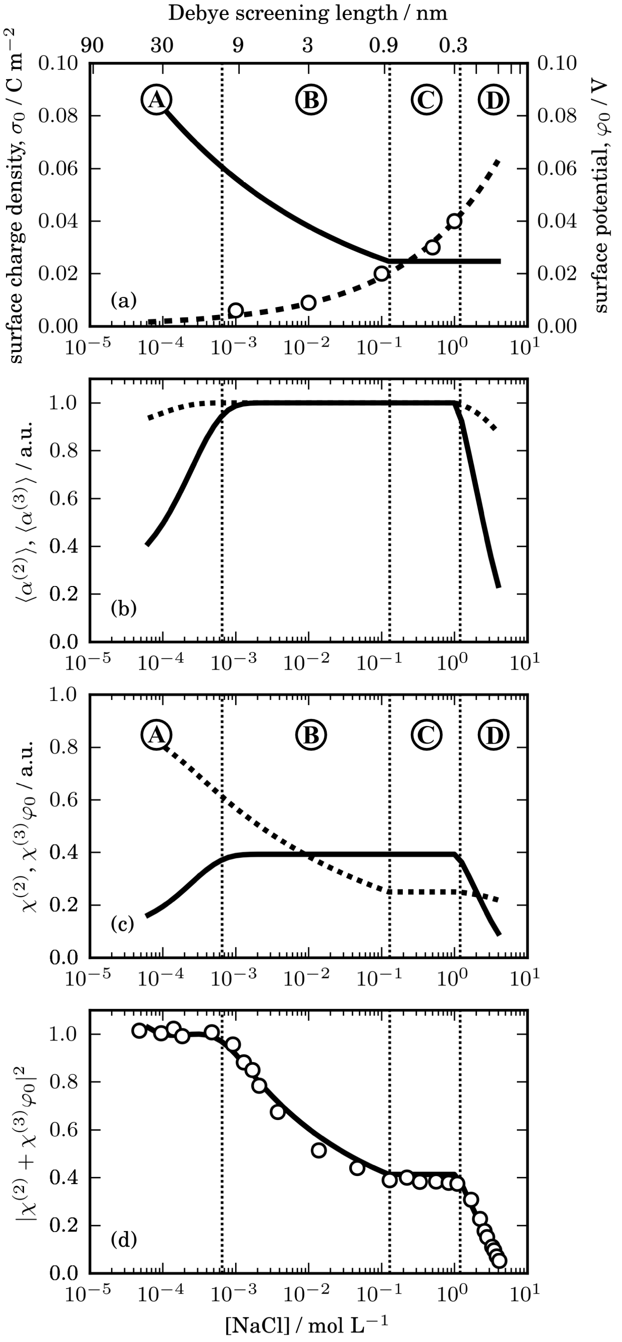

Figure 3.5: Proposed model of the balance between electrolyte screening of the surface electric field and charge-induced molecular order at the interface. The dashed line in (a) shows a function fit to empirical surface charge measurements (points) at the fused silica–water interface.[101] The solid line in (a) represents the surface potential, calculated from the surface charge data at $I \leq 0.13\,\mathrm{mol\,L^{-1}}$ and by the Stern model at $I > 0.13\,\mathrm{mol\,L^{-1}}$. Relative effects of interfacial order are shown in (b) by the solid lines for $\langle\alpha^{(2)}\rangle$ and dotted lines for $\langle\alpha^{(3)}\rangle$. Contributions of the $\chi^{(2)}$ (solid line) and $\chi^{(3)}$ terms to the measured signal are shown in panel (c). The solid line in (d) shows the modeled signal alongside our measured data (points).

structure acts like a capacitor[11]

$$\Psi_0 = \frac{\sigma_0 d}{\varepsilon_{\mathrm{Stern}}\varepsilon_0} \tag{3.3}$$

where Ψ_0 is the potential at the surface, $\varepsilon_{\mathrm{Stern}}$ is the dielectric constant of the Stern layer (which differs from that of bulk water), ε_0 is the vacuum permittivity, and d is the distance between the negatively charged surface and the cations.

3.3.2 Model

Now consider the four regions A–D identified in Figure 3.4. The development of the surface charge, surface potential,[101,103] $\langle\alpha^{(2)}\rangle$, $\langle\alpha^{(3)}\rangle$, $\chi^{(2)}$, and $\chi^{(3)}\Psi_0$ with increasing ionic strength, along with the model predicted SFG intensities, is shown in Figure 3.5 to aid in this discussion.

Region A. At ionic strengths less than $0.7\,\mathrm{mmol\,L^{-1}}$ (indicated by the cyan data in Figure 3.3) there is no change in SFG intensity with increasing ionic strength. This region is clearly identified as the initial flat region in Figure 3.4. Since the static field penetrates into the bulk, it is reasonable to expect that screening by charged species in solution would reduce the relative contribution of the $\chi^{(3)}$ term in Eq. 3.1. On the other hand, it has been established that increasing solution ionic strength promotes the development of a more negative charge at the surface,[101,104,105] as plotted in Figure 3.5a (points). This should increase the degree to which the first few layers of water are oriented, and thereby enhance the $\chi^{(2)}$ and $\chi^{(3)}$ contributions to the signal. Simulations of water structure next to charged interfaces show that, as the surface charge increases, water molecules are increasingly aligned adjacent to the interface, but are not oriented past $\approx 1.5\,\mathrm{nm}$ from the surface.[65–68] This balance between enhancement of $\chi^{(2)}$ and $\chi^{(3)}$ due to increased structure near the interface and reduction of $\chi^{(3)}$ due to screening is illustrated in Figure 3.5 and results in the region A plateau. In the original SHG ionic strength study by Eisenthal et al., the authors remarked that they did not observe evidence of the expected increasing surface charge with salt concentration.[11] Since our data include measurements at much lower ionic strengths, the balance between screening and the development of additional surface charge, that results in the region A plateau, is observed

Region B. Above an ionic strength of $0.7\,\mathrm{mmol\,L^{-1}}$, it was observed that the signal drops as the ionic strength increases. This is accounted for in the model by continued development of the surface charge coupled with only a slight increase to a constant interfacial ordering. The net effect on the SFG signal is that the $\chi^{(2)}$ term in Eq. 3.1 now remains constant while the $\chi^{(3)}$ term decreases, being dominated by an increased screening of $\mathbf{E}_0$ throughout the region.[101,104,105] These results are in agreement with those observed by Eisenthal et al.[11] As we approach Debye lengths of $\approx 2\,\mathrm{nm}$, we are now near the extent of the outermost ordered non-centrosymmetric water layers. We propose that the slower drop in signal towards the end of region B is a sign that we are entering a region near the surface where there is a more significant contribution from $\chi^{(2)}$.

Region C. A second plateau in the SFG signal is observed between approximately $0.1\,\mathrm{mol\,L^{-1}}$ and $1\,\mathrm{mol\,L^{-1}}$ ionic strength. We propose that this plateau is the effect of two phenomena. First, $\chi^{(2)}$ dominates signal in this region as a result of the short penetration distance of the surface field into bulk, resulting in a small relative $\chi^{(3)}$ contribution. Second, this region marks the transition from the Gouy-Chapman model of surface to the Stern model where the surface potential now remains constant. As a result, both the second- and third-order terms remain constant over this region. This means that the (already small) contribution of $\chi^{(3)}$ remains constant over the entire range of ionic strengths in region C, further supporting the plateau feature observed in this region.

Region D. At ionic strengths greater than $1.1\,\mathrm{mol\,L^{-1}}$, the signal drops rapidly. As this behavior abruptly follows the region C plateau, we believe that the hydrogen bonding environment near the interface is disturbed at these high salt concentrations. This results in a less-ordered environment near the surface and hence both $\chi^{(2)}$ and the ordered component of $\chi^{(3)}$ decrease rapidly. A similar behavior has been observed in the case of the air–water interface at high salt concentrations.[53] The perturbation may be partially due to water displacement upon ion contact adsorption, thereby disrupting the highly-ordered water layers immediately adjacent to the surface. If all polar ordering were to be disrupted, we would be left with only the isotropic contribution of $\chi^{(3)}$.

3.3.3 Model Construction

The model described above is comprised of several equations parameterized to fit the observed changes in SFG response. As such, it does not provide a quantitative description of the interface (i.e. the absolute number density of molecules contributing to $\chi^{(2)}$ is not known). However, relative contribution of second- and third-order processes are presented by the model.

Surface charge as a function of ionic strength was estimated from a fit of empirical charge data[101]

$$\sigma_0 = (0.04\,\mathrm{C\,m^{-2}\,L^{0.33}\,mol^{-0.33}})I^{0.33}. \tag{3.4}$$

From the estimated surface charge, surface potential was determined using an approximation of Gouy-Chapman theory for $I < 0.13\,\mathrm{mol\,L^{-1}}$ and set to be constant as per the Stern model at concentrations greater than $0.13\,\mathrm{mol\,L^{-1}}$

$$\Psi_0 = \begin{cases} \dfrac{\sigma_0}{(2.3\,\mathrm{F\,m^{-2}\,L^{0.5}\,mol^{-0.5}})\sqrt{I}}, & I < 0.13\,\mathrm{mol\,L^{-1}} \\ \dfrac{\sigma_0}{(2.3\,\mathrm{F\,m^{-2}\,L^{0.5}\,mol^{-0.5}})\sqrt{0.13\,\mathrm{mol\,L^{-1}}}}, & I \geq 0.13\,\mathrm{mol\,L^{-1}} \end{cases} \tag{3.5}$$

The equations describing molecular order were defined so that a value of 1.0 corresponds to the fully ordered state (note that the fully ordered state for the second- and third-order responses are not necessarily the same). The equations are split into two cases; the first case represents development of interfacial order due the increase in surface charge with increasing ionic strength and the second case describes the breakdown of interfacial order by disruption of hydrogen bonding network.

$$\langle \alpha^{(2)} \rangle = \begin{cases} (1) - (0.76)e^{(-4070\,\mathrm{L\,mol^{-1}})I}, & I < 1.1\,\mathrm{mol\,L^{-1}} \\ (1)e^{(0.5\,\mathrm{L\,mol^{-1}})(1.1\,\mathrm{mol\,L^{-1}} - I)}, & I \geq 1.1\,\mathrm{mol\,L^{-1}} \end{cases} \tag{3.6}$$

$$\langle \alpha^{(3)} \rangle = \begin{cases} (1) - (0.13)e^{(-11200\,\mathrm{L\,mol^{-1}})I}, & I < 1.1\,\mathrm{mol\,L^{-1}} \\ (1)e^{(0.046\,\mathrm{L\,mol^{-1}})(1.1\,\mathrm{mol\,L^{-1}} - I)}, & I \geq 1.1\,\mathrm{mol\,L^{-1}} \end{cases} \tag{3.7}$$

Since the model is designed to describe changes in the *integrated* response to changes in ionic strength, a relative integrated susceptibility was defined as a function of the molecular order as follows:

$$X^{(2)} = (3.93)\langle \alpha^{(2)} \rangle \tag{3.8}$$

and

$$X^{(3)} = (101)\langle \alpha^{(3)} \rangle. \tag{3.9}$$

Since the shapes of the fused silica–water spectra do not change as a function of ionic strength, $X^{(2)}$ and $X^{(3)}$ are analogous to $\chi^{(2)}$ and $\chi^{(3)}$ and may be assumed to co-vary. Now, the normalized SFG response may be calculated

$$\frac{\int I_{\text{SFG}}(\omega, I)d\omega}{\int I_{\text{SFG}}(\omega, I=0)d\omega} = (X^{(2)} + \Psi_0 X^{(3)})^2. \tag{3.10}$$

3.4 Comparison of Mineral and Polymer Interfaces

In this section we interpret changes in the SFG spectra of fused silica, calcium fluoride (CaF_2), polystyrene, and poly(methyl methacrylate) in contact with aqueous solutions of sodium chloride. Our results illustrate the striking effects that substrate material and electrolyte concentration have upon interfacial water. Spectra from the fused silica–solution and polystyrene–solution interfaces both decrease in overall intensity with increasing salt concentration. On the other hand, the effect of salt on the CaF_2–solution and PMMA–solution interfaces is to strongly increase the spectral intensity at high ionic strength. Across the board, however, a shift in the intensity of the $3400\,\text{cm}^{-1}$ peak relative to the $3200\,\text{cm}^{-1}$ peak provides evidence that a decrease in the coordination of surface-bound water may be a unifying behavior that links these observations.

In order to compare SFG spectra collected from different solid–solution interfaces over a wide range of ionic strengths, the local field effects must be accounted for.[6,106–108] The quantities in Equation 3.1 are more precisely effective susceptibilities, $\chi^{(2)}_{\text{eff}}$ and $\chi^{(3)}_{\text{eff}}$. These contain the local field correction factors L that relate the incident and generated fields in a bulk medium to the respective fields at the interface, and are themselves functions of the angle of incidence θ_i, and the refractive indices n_1 and n_2 of the two interfacial phases. One also considers the unit polarization vectors $\hat{e}$ that account for the projection of the s- and p-states onto the x, y, z coordinate system,

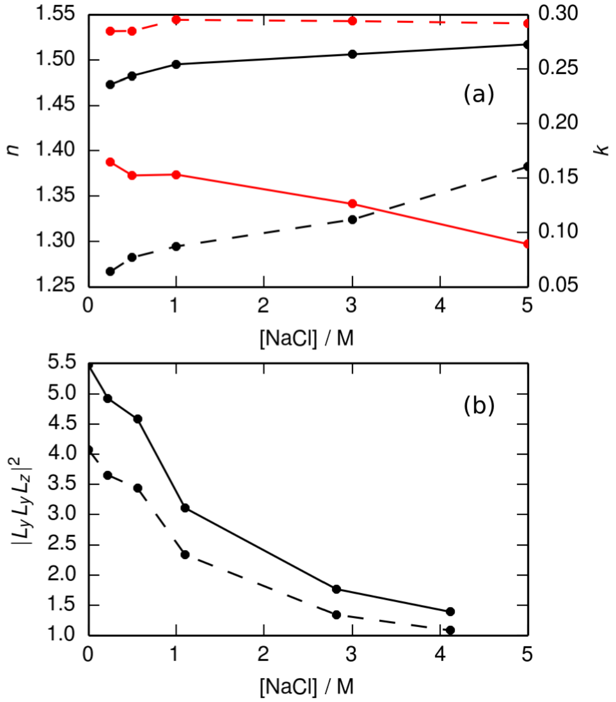

Figure 3.6: (a) Dependence of the real (n, black) and imaginary (k, red) components of NaCl solution refractive index at 3200 cm^{-1} (solid line) and 3400 cm^{-1} (dashed line). (b) Dependence of the local field correction on NaCl concentration.

resulting in

$$\chi^{(2)}_{\text{eff}} = L_{\text{SFG}}(\theta_{\text{SFG}}, n_1, n_2)\hat{e}(\theta_{\text{SFG}})\chi^{(2)}L_{\text{vis}}(\theta_{\text{vis}}, n_1, n_2)\hat{e}(\theta_{\text{vis}})L_{\text{IR}}(\theta_{\text{IR}}, n_1, n_2)\hat{e}(\theta_{\text{IR}}). \tag{3.11}$$

As a surface field, no local field correction is necessary for $\mathbf{E}_0$ and the relationship between $\chi^{(3)}$ and $\chi^{(3)}_{\text{eff}}$ is analogous to Equation 3.11. We used complex refractive indices of the prisms and polymers as reported in the literature.[109–112] Refractive indices of NaCl solutions were determined via interpolation from published data[113–115]. The importance to our analysis of rigorously determining n_1 and n_2 is evident from the relative change in NaCl solution refractive index at 3200 cm^{-1} and 3400 cm^{-1} (Figure 3.6a) and the effect upon the product of the local field correction factors (Figure 3.6b).

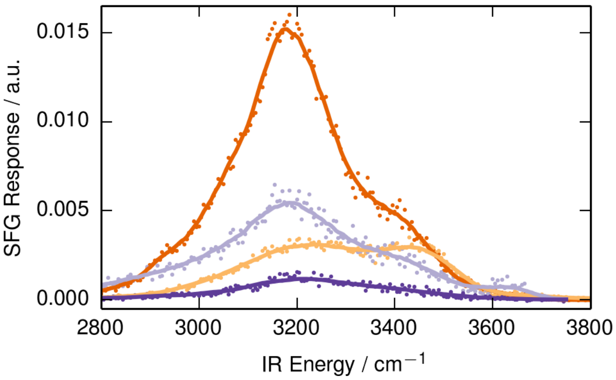

Figure 3.7: SFG spectra, corrected for local field effects, of fused silica–water (orange), polystyrene–water (light purple), CaF_2–water (light orange), and PMMA–water (purple) interfaces. Lines through the data are shown to guide the eye.

The starting point for this discussion is a comparison of the neat water spectra collected from the four interfaces (Figure 3.7). In all cases, spectra exhibit the broad peaks near 3200 cm^{-1} and 3400 cm^{-1} that are characteristic of interfacial water. The system with the strongest response is, by far, the negatively charged fused silica–water interface. Its shape is dominated by the peak near 3200 cm^{-1}. Previously reported spectra of the fused silica–water interface displayed the same 3200 cm^{-1} peak,[56,116] but to a lesser extent than we have observed. We suggest that this difference is an outcome of slightly different silica crystalline structure arising from differences in surface preparation; a comparison of α-quartz–water and fused silica–water SFG spectra reveals the sensitivity of water structure to SiO_2 crystal structure.[116] Spectral response from the CaF_2 interface is relatively weak compared to that of fused silica. This is consistent with earlier observations of this interface at a pH near the CaF_2 point of zero charge (6.2).[117,118] At the working pH (6.0), the interfacial potential will be small and exert minimal orienting influence upon the neighboring water molecules. Similar to CaF_2, SFG responses from the polymer interfaces are weak compared with FS. This again is attributed to a relatively weak interfacial potential.

We now turn our attention to the effect of electrolytes upon the interface. Central to this discussion are two representations of the data obtained by varying the salt concentrations of solutions adjacent to the four solid surfaces. The top row of Figure 3.8 (a–d) shows the evolution of the SFG spectra normalized to the point of overall highest intensity for each interface. This draws attention to the overall signal variation in response to the ionic strength. The bottom row (e–h) was created by first normalizing the spectra with respect to the point of highest intensity at each ionic strength. This representation allows the variation in SFG with IR energy to be inspected as the salt concentration changes, irrespective of the magnitude of the overall response. The manner in which the overall intensities vary highlights the considerable differences of the four materials. However, a similarity shared by all four interfaces is observed in the evolution of spectral shape.

3.4.1 Fused Silica

Evolution of the overall spectral intensity at the silica–solution interface (Figure 3.8a) is considered to be typical of a negatively charged mineral surface.[11,69,98,119] In the model specific to the silica–solution interface changes in integrated signal are related to changes in interfacial structure through $\chi^{(2)}$ and $\chi^{(3)}$.[91] Following the evolution of the $3200\,\mathrm{cm}^{-1}$ peak intensity from low to high ionic strength, there is an initial plateau of strong intensity (purple) followed by a gradual decrease to near zero intensity (orange). Over the course of this decrease, the dominant mode remains at $3200\,\mathrm{cm}^{-1}$; only at the highest salt concentrations does the resonant mode at $3400\,\mathrm{cm}^{-1}$ increase in prominence (Figure 3.8e). At pH 6, the fused silica–water interface is negatively charged, with the charge σ_0 located on exposed oxygens of the Si–O lattice. As I increases, so too do σ_0 and φ_0.[101,104,105] The model accounted for the low ionic strength behavior by an increase in the polar ordering of the water molecules, thereby increasing the second-order contribution to the signal.[91] Balancing the second-order signal

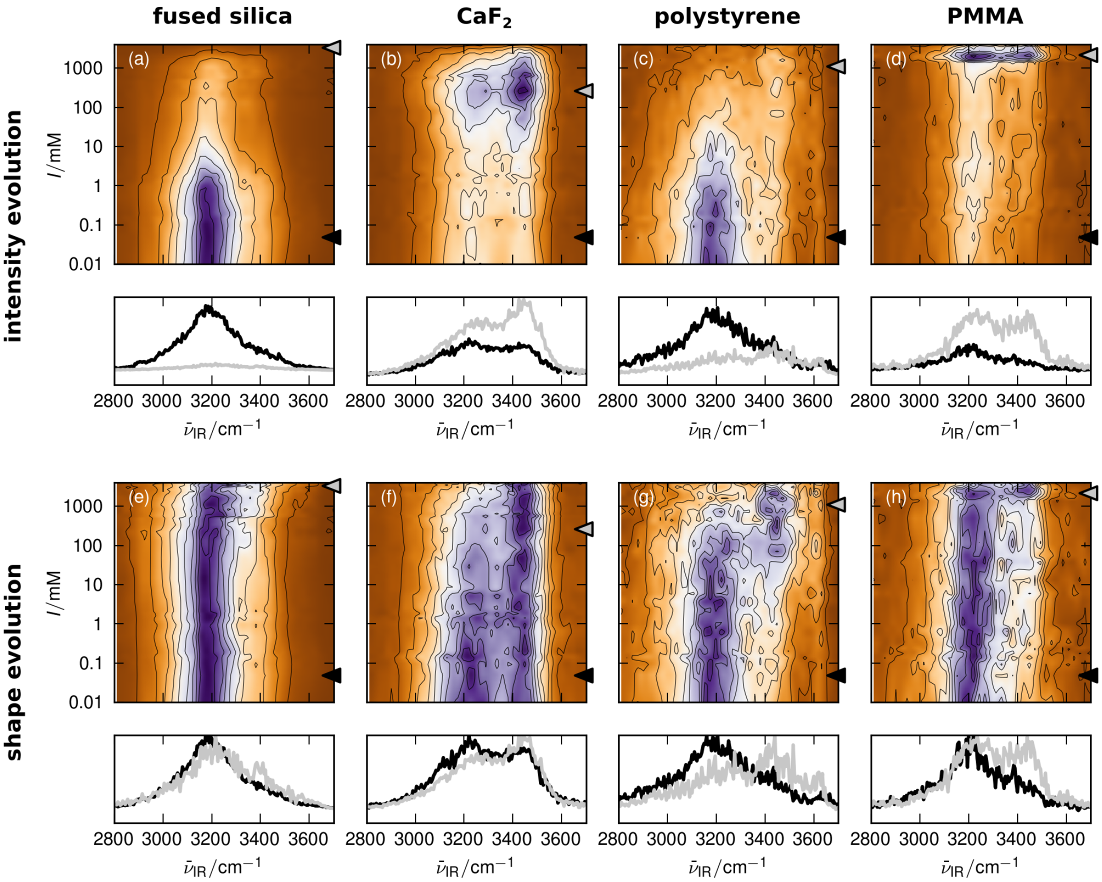

Figure 3.8: The evolution of SFG spectra as a function of solution NaCl concentration. (a–d) Contours generated from individual spectra, normalized to the strongest overall response, show the evolution of spectral intensity. (e–h) The same dataset, but normalized to the strongest response at each ionic strength, illustrate the evolution of spectral shape. Data from each of the four interfaces are scaled independently. Strong spectral response is shown in purple and weak response is shown in orange. Panels below the contour plots highlight the differences at low (black) and high (gray) salt concentrations, as indicated by the arrows.

increase was a decrease in the third-order contribution resulting from a decreased penetration depth of the static field, $\mathbf{E}_0$. At higher I, when maximum water ordering has been achieved, decrease in the signal intensity was attributed solely to a further decrease in the extent of $\mathbf{E}_0$. During the course of increasing I there is a migration of ionic species in the interfacial region to balance σ_0.[14,102] In this system, the migration has been described to be a net depletion of Cl^- and accumulation of Na^+ near the interface.[14] It is likely that at high I, the accumulated Na^+ cations partially disrupt hydrogen bonding between water molecules, lower their average coordination, and increase the relative strength of the $3400\,\mathrm{cm}^{-1}$ peak.

3.4.2 Calcium Fluoride

Evolution of the overall intensity and shape of the CaF_2–solution spectra (Figure 3.8b) clearly indicates a much different interfacial structure than the FS–solution interface. Overall intensity was weak and nearly constant at low I ($< 1\,\mathrm{mmol\,L}^{-1}$). Intensities at $3200\,\mathrm{cm}^{-1}$ and $3400\,\mathrm{cm}^{-1}$ were similar, with perhaps a slight favoring of the lower energy mode. Based on the proximity of the experimental pH (6.0) to the mineral point of zero charge ($\mathrm{pH}_{\mathrm{pzc}}$) (6.2)[90,120], and in the context of the silica–solution interfacial model, this low I interfacial behavior was expected. Near the point of zero charge, φ_0 will be small, and hence a weak second-order response is expected due to a lack of significant electrostatic alignment of the water molecules. Furthermore, since $\mathbf{E}_0$ is small, minimal third-order response is expected. However, the behavior at higher ionic strength was unexpected. Spectral intensity slowly builds throughout the O–H stretching region, reaching a maximum at $0.5\,\mathrm{mol\,L}^{-1}$, followed by a rapid decrease. At the same time the spectra become dominated by the $3400\,\mathrm{cm}^{-1}$ feature (Figure 3.8f). A possible explanation for these observations hinges on dissolution of CaF_2. Unlike silica, CaF_2 is an ionic solid and the formation of interfacial charge is different. Above $\mathrm{pH_{pzc}}$, the surface gains negative charge by exchange of exposed F with OH. Below $\mathrm{pH_{pzc}}$, a positive charge is established by selective dissolution of $\mathrm{F^-}$, leaving a positive charge centered on the exposed $\mathrm{Ca^{2+}}$ sites.[121] A study of the effects of solution ionic strength on $\mathrm{CaF_2}$ solubility measured a one order of magnitude increase in the solubility between pure water and an NaCl concentration of $0.73\,\mathrm{mol\,kg^{-1}}$.[122] Our experiment was performed at a pH slightly lower than $\mathrm{pH_{PZC}}$, resulting in a slight positive charge at the interface. At this pH, an increase in NaCl concentration leads to further dissolution of $\mathrm{F^-}$, enhancing the surface charge. In the context of our model,[91] enhancement of φ_0 promotes polar ordering of interfacial water molecules thereby increasing both $\chi^{(2)}$ and $\chi^{(3)}$. At the same time, increased screening of the developing surface field reduces $N^{(3)}$. For a while, the buildup of φ_0 outweighs the diminishing $N^{(3)}$, and the third-order term in Equation 3.1 increases, but eventually diminishing $N^{(3)}$ dominates and the third-order term decreases.

3.4.3 Polystyrene

A pattern similar to the FS–solution interface is seen at the polystyrene–solution interface (Figure 3.8c). The strongest response is seen at very low ionic strength. This response diminishes with increased ionic strength until very little signal is observed. As this behavior is typical of a charged surface, we have reason to believe that our polymer sample exhibits properties of an oxidized polystyrene surface. This would have the effect of providing oxygen centers attached to the polystyrene aromatic carbons on which to carry a charge.[123,124] A recent molecular dynamics study of the oxidized polystyrene–water interface showed increased hydrophilic nature with increased surface oxygen concentration.[125] The same study examined the distribution of O–H–O (polystyrene oxygen, water hydrogen, water oxygen) angles and found them to be dominated by angles representative of hydrogen-bonding interactions.

Coupled with atomic force microscopy measurements of interfacial double layer-like potential decay from charged PS surfaces,[126] we propose that our measurements of the polystyrene–solution interface represent a non-mineral example of the behavior of water at a charged surface. While the variation in overall intensity is similar to fused silica, the evolution of spectral shape differs (Figure 3.8g). The spectra start out dominated by intensity at $3200\,\mathrm{cm^{-1}}$ at low ionic strength and undergo a sharp transition to $3400\,\mathrm{cm^{-1}}$ near $0.1\,\mathrm{mol\,L^{-1}}$ NaCl. As the concentration reaches $1\,\mathrm{mol\,L^{-1}}$, the spectral response becomes strongly localized near $3400\,\mathrm{cm^{-1}}$. Although we also observed emergence of $3400\,\mathrm{cm^{-1}}$ intensity at the fused silica interface, it is much more pronounced here.

3.4.4 Poly(methyl methacrylate)

The spectral evolution at the PMMA–solution interface is more similar to CaF_2 than to that of the FS–solution interface. At low ionic strength the overall spectral intensity is weak (Figure 3.8d). Spectra are dominated by intensity at $3200\,\mathrm{cm^{-1}}$ and this dominance is nearly immune to increasing ionic strength. However, a dramatic burst in signal intensity at $2\,\mathrm{mol\,L^{-1}}$ NaCl reveals itself with equal contributions of the $3200\,\mathrm{cm^{-1}}$ and $3400\,\mathrm{cm^{-1}}$ response (Figure 3.8h). Similar to the CaF_2 interface, the low intensity (and unvarying spectra at low ionic strength) is the direct result of low interfacial potential at this uncharged interface, leading to weak $\chi^{(2)}$ and $\chi^{(3)}$. The sharp development of signal at $2\,\mathrm{mol\,L^{-1}}$ NaCl may be due to a buildup of Cl^- anions at the interface. Similar behavior has been modeled and measured at the hydrophobic air–water and octadecyltrichlorosilane (OTS)–water interfaces.[59,127] In the OTS–water study, Tian et al demonstrated increases in spectral intensity arising from an increase in solution pH or an increase in solution NaCl concentration.[127] They attributed the enhanced signal upon increased pH to additional surface charge from

OH^- accumulation. Following that same logic, they inferred that the signal increase observed upon addition of NaCl was due to increasing Cl^- at the interface. Since it has been demonstrated that the terminal methyl groups are exposed at PMMA and OTS surfaces,[25] it is reasonable that the development of interfacial gradients is similar to that of the OTS–solution interface. In our experiments, this would have the effect of increasing both φ_0 and $\mathbf{E}_0$ and would lead to the observed strong second- and third-order responses. Such a model may also account for our observation of a change in the relative contributions of the $3200\,\mathrm{cm}^{-1}$ and $3400\,\mathrm{cm}^{-1}$ peaks. It is plausible that the anions compete with neighboring waters in the hydrogen bonding network, in effect decreasing the overall coordination of the interfacial water molecules.

3.4.5 Water Coordination

We propose that a thread linking these four interfaces may be a change in water coordination. In the case of FS, the charged nature of the surface acts to strongly maintain the hydrogen-bonding network over a large range of ionic strength. This network is disrupted only at very high ionic strength, leading to the observed spectral changes. At the nearly charge-neutral CaF_2 interface where there is likely a more gradual build-up of anionic species in the interfacial region, we observe a concomitant shift towards $3400\,\mathrm{cm}^{-1}$. Similarly, the PS interface is not as strongly orienting as FS, and therefore an accumulation of ions in the interfacial region is more effective at disrupting the water structure. Finally, the shift from $3200\,\mathrm{cm}^{-1}$ to $3400\,\mathrm{cm}^{-1}$ at the PMMA interface, which does not occur until very high ionic strength, may be due to preferential accumulation of ionic species. For all interfaces studied, we observe a drop in spectral intensity to near zero at very high salt concentration. This has previously been attributed to a breakdown in ordered water via disruption of the hydrogen bonding network by ionic species.[52,89,91]

3.5 Summary

In summary, we have varied the concentration of salt to measure key characteristics of water structure at a charged solid surface. At extremely low ionic strength, we observe a plateau in the spectroscopic response. This is attributed to the expected but previously-unobserved balance between screening and the development of additional surface charge for fused silica. At ionic strengths greater than $0.7\,\mathrm{mmol\,L^{-1}}$, a rapid drop in signal occurs as the surface field is now effectively screened. Near the end of region B, the trend gives way to a slower decrease as $\chi^{(2)}$ dominates, approaching an interfacial depth of about $2\,\mathrm{nm}$. Eventually we reach the limit of the ionic cloud diffuse charge model, and switch to a capacitor model at high ionic strength. Here, both $\chi^{(2)}$ and $\chi^{(3)}$ contributions remain constant with increasing salt concentration. Finally, at very high ionic strength, we observe a disruption in the hydrogen bonding network on account of contact adsorption. Our findings suggest that a few layers of water are strongly ordered near the charged surface. These ordered layers contribute to the second-order response that relies on symmetry breaking. The third-order response may be generated from a much greater depth, limited by the penetration of the surface field due to screening by the electrolyte ions. This highlights the necessity of considering $\chi^{(3)}$ contributions in nonlinear optical studies of charged interfaces.

Additional experiments would be able to further support these claims. For example, varying the electrolyte concentration and species over range of pH values would be valuable. For these proposed experiments, resolving the amplitude and phase of the SFG signal under a variety of beam polarizations would also assist in the further refinement of a model for surface water structure. It is noted that, while SFG experiments provide insight on the distribution of local hydrogen bonding environments, non-resonant SHG experiments would also provide an efficient and robust manner for obtaining pertinent data for these models.

We have also observed surprising similarities and differences in the behavior of interfacial water at four surfaces in the presence of salt. Fused silica and polystyrene surfaces are similar in that both display a monotonic decrease in nonlinear susceptibility throughout the O–H stretching region with increasing ionic strength. From that standpoint, CaF_2 and PMMA are closely related as the overall intensity increases with ionic strength; both surfaces display a signal spike at high ionic strength. Despite their differences, all four surfaces respond in a manner that may be evidence of a decrease in water coordination upon salt addition. The concentrations at which this response initiates, and the range of concentrations over which it proceeds, are dependent upon chemical and physical properties of the individual surfaces. We hope that the data we have provided will promote deeper investigation of the water structure at these important interfaces.

Chapter 4

Phase-sensitive SFG of Exposed Interfaces

Reproduced in part from Covert, P. A.; FitzGerald, W. R.; Hore, D. K. "Simultaneous measurement of magnitude and phase in interferometric sum-frequency vibrational spectroscopy." *J. Chem. Phys.,* **137,** 014201 (2012). Copyright 2012 American Institute of Physics. All experimental design, data collection, and data analysis performed by Paul Covert.

4.1 Introduction

While the theory and methods for SFG phase measurement have been developed,[7,8,33,37] the experiment remains challenging to perform quantitatively, as extreme care is required to minimize the error in the measured phase. As a result, there is considerable attention to how well measurements from different labs can be compared.[128] An elegant technique for high-precision phase measurements has been developed for broadband SFG experiments by Tahara's group.[8,33] While their technique has emerged as the method of choice for ultrafast pulses, it is not amenable to picosecond pulses. We have previously presented a model to describe the two-dimensional interference fringes generated in picosecond, scanning phase-sensitive experiments that allows for the determination of $\chi_{\mathrm{S}}^{(2)}$ phase from the fringe features that extend in the temporal and spectral dimensions.[37] We now illustrate that the magnitude and phase of $\chi_{\mathrm{S}}^{(2)}$ can be quantitatively extracted from the interference fringes alone, thereby providing a robust route to picosecond phase-resolved SFG. Furthermore, the method described here eliminates the need to alter the experiment by removal of the local oscillator. We provide a complete demonstration of this procedure in the characterization of the octadecyltricholosilane (OTS) surface over the IR energy region of the C–H stretching modes.

4.2 Experimental Methods

SFG measurements A schematic of our experimental geometry appears in Figure 4.1. Details of our vibrational sum-frequency spectrometer are found in Jena et al.,[37] as well as details concerning the addition of a local oscillator (LO) in a collinear geometry. In brief, a 10 Hz, 25 ps, 1064 nm Nd:YAG laser (Ekspla PL2241) is doubled to serve as the visible (532 nm) pump beam. The 1064 nm and a fraction of the 532 nm beams pump a parametric generator (Ekspla PG501) to create continuously tunable infrared radiation (2800–3000 cm^{-1} in this experiment) with a FWHM bandwidth less than 6 cm^{-1}. A nominally 50 µm thick piece of y-cut quartz (Del Mar Photonics, CA) generates the LO that passes through the phase-shifting unit (PSU) along with the remaining visible and infrared pump beams. The tilt angle of the PSU was rotated from $-45°$ to $45°$ to generate an interferogram at each wavelength of interest over the 2800–3000 cm^{-1} region. To better capture the decreasing period of the temporal fringes, the PSU tilt angle was not varied linearly. At high angles (PSU close to $\pm 45°$) the spacing between data points was smaller than at low angles (closer to normal incidence). All spectra were measured in the ssp polarization configuration with an angle of incidence of 50°.

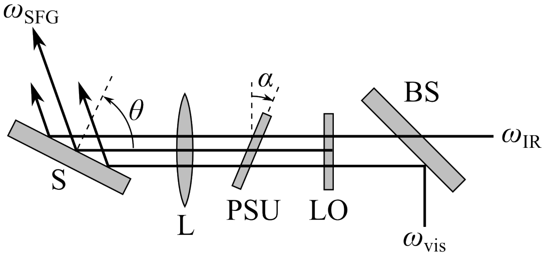

Figure 4.1: Collinear beam geometry used for phase-sensitive vibrational sum-frequency experiments. Illustrated are placements of a beamsplitter (BS), LO generator, PSU, focusing lens (L), and sample (S).

Sample preparation OTS monolayers were prepared following the procedure described Liu et al.[129] Octadecyltrichlorosilane (Aldrich, 90+%), used with no further purification, was prepared as a $1.0\,\text{mmol}\,\text{L}^{-1}$ solution in a 4:1 v/v mixture of hexadecane and carbon tetrachloride. Glass plates (approx. 5 mm thick) were cleaned by immersion for 1 h in piranha solution at 110 °C, rinsed with copious amounts of Milli-Q water, and dried with nitrogen. The OTS monolayers were deposited onto the clean, dry glass plates by submersion of the plates into the OTS solution for 6 h. Following immersion, unreacted precursor molecules were removed from the substrate by rinsing with the following sequence of solvents: chloroform, acetone, methanol, Milli-Q water, methanol, acetone, approx. 1 min sonication in chloroform, acetone, methanol, Milli-Q water. Finally, the substrates were dried with nitrogen gas and heated in an oven at 80 °C for 3 h.

Crystalline α-quartz cut perpendicular to the z-axis was used as the phase reference material. The quartz surface was polished in four steps using progressively finer grit silicon carbide and finished with approximately 35 h of polishing with iron oxide (jeweler's rouge). Following the polishing, the surface was sonicated and thoroughly rinsed with Milli-Q water to remove all traces of the polishing compound.

4.3 Results and Discussion

Interferograms collected at each IR wavelength encode magnitude and phase information for both the sample and local oscillator sum-frequency fields, $\mathbf{E}_{\mathrm{S}}$ and $\mathbf{E}_{\mathrm{LO}}$ respectively. In an earlier publication, we reported a method to obtain the phase of $\chi_{\mathrm{S}}^{(2)}$ from normalized temporal interferograms.[37] Here we extend that method to extract the magnitude of the sample SF field $|\mathbf{E}_{\mathrm{S}}|$, in addition to its phase ϕ_{S}, from the same interferogram. The benefit of this approach is that we can obtain both the real and imaginary components of $\chi_{\mathrm{S}}^{(2)}$ with the local oscillator present. While this approach is not as straightforward as is a homodyne experiment for obtaining $|\chi_{\mathrm{S}}^{(2)}|$, we demonstrate that it leads to increased precision in the phase measurement. This is a result of the static nature of all optics in the setup, apart from the PSU, and the insensitivity of the collinear geometry to sample positioning.

4.3.1 Phase stability in a collinear beam geometry

Prior to discussing our procedure for simultaneous $\chi^{(2)}$ magnitude and phase retrieval, we first illustrate that collinear SFG experiments are particularly interesting candidates for this analysis due to their high phase stability with respect to sample position. This motivates the use of a single experimental configuration for the simultaneous collection of $|\chi_{\mathrm{S}}^{(2)}|$ and φ_{S}. Data collection in this manner is advantageous since the local oscillator may remain in place while the relative phase of an unknown sample is translated into an absolute phase by comparison with the response of a reference sample measured at the same position.

Referring to Figure 4.1, the phase of $\chi_{\mathrm{S}}^{(2)}$ has three contributions: the phase difference between the sample and the local oscillator $\Delta\varphi_{\mathrm{S \cdot LO}}$; the phase shift associated with the phase-shifting unit (rotating silica plate) $\Delta\varphi_{\mathrm{PSU}}$; and the phase shift due to the fixed focusing lens $\Delta\varphi_{\mathrm{lens}}$. Here we note that we are working under the assumption that the radius of curvature of the lens is large with respect to the diameter of the beam. In order to discuss the sensitivity of our phase measurement to the precise positioning of the sample, the phase shift of the beams in air between the sample and the source of the LO must additionally be considered. A complete description of the phase contributions is given by

$$\Delta\varphi = \Delta\varphi_{\mathrm{psu}} + \sum_j \Delta\varphi_j - \Delta\varphi_{\mathrm{S \cdot LO}} \tag{4.1}$$

where we account for the phase shift due to each of j fixed-position dispersive elements between the sample and the y-cut quartz. In order to assess the effect of sample position (z_{S}) on the measured phase, we recognize that a change in sample position is in effect equivalent to altering the path length that each of the beams travel through air

$$\delta d_i = \frac{\delta z_{\mathrm{S}}}{\cos\theta_i}. \tag{4.2}$$

Here i refers to each of the sum-frequency, visible, and infrared beams; δz_{S} is the uncertainty in the sample position, and θ_i is the angle of incidence for each beam. The phase error is then the relative phase shift due to changes in the optical path lengths of the three beams

$$\delta\varphi_{\mathrm{air}} = n_{\mathrm{SF}}\omega_{\mathrm{SF}}\ \delta d_{\mathrm{SF}} - n_{\mathrm{vis}}\omega_{\mathrm{vis}}\ \delta d_{\mathrm{vis}} - n_{\mathrm{IR}}\omega_{\mathrm{IR}}\ \delta d_{\mathrm{IR}}. \tag{4.3}$$

In the case of $\Delta\varphi_{\mathrm{air}}$ the uncertainty associated with this quantity can be related to the uncertainty in the sample position δz_{S}.

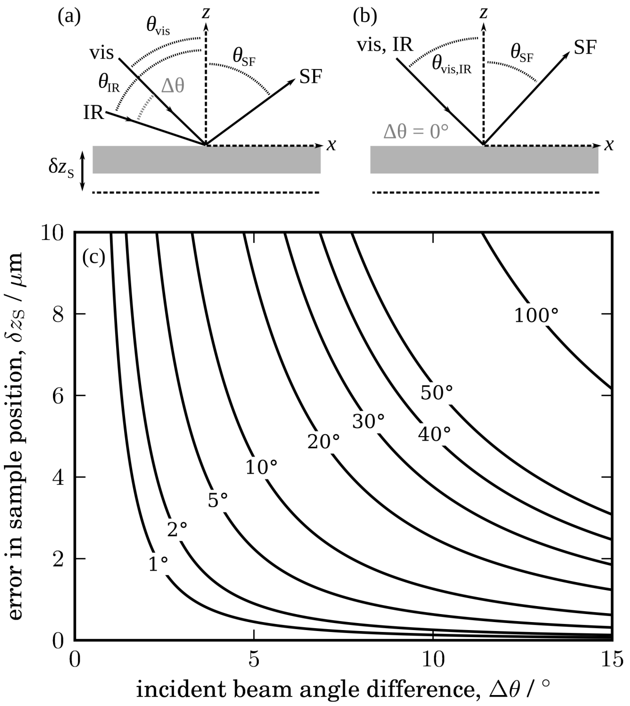

Figure 4.2: The difference between (a) non-collinear ($\Delta\theta \equiv |\theta_{\mathrm{vis}} - \theta_{\mathrm{IR}}| > 0°$) and (b) collinear ($\Delta\theta = 0°$) beam geometries in generating a sum-frequency response. (c) A map of the phase error as a function of the error in sample position and the difference in the incident angles of the two pump beams. A few phase error contours are labelled.

We now consider how the geometry of the three incident beams affects the phase error. When the beams are not collinear, as shown in Figure 4.2a, a small change in z_{S} leads to unequal changes in the physical path lengths of the three beams and so $\delta d_{\mathrm{SF}} \neq \delta d_{\mathrm{vis}} \neq \delta d_{\mathrm{IR}}$. The greater the angle between the incident IR and visible pump beams, the more dominant the difference in physical path length becomes in determining the phase error as a result of the dispersion in air. A map of the sensitivity of the phase error to the sample position and $\Delta\theta$ in Figure 4.2c illustrates this relationship.

4.3.2 Amplitude and phase determination

One way to measure the magnitude and phase of $\chi_{\mathrm{S}}^{(2)}$ is to first measure the sum-frequency spectrum of the sample in the absence of the local oscillator, resulting in $|\mathbf{E}_{\mathrm{S}}|^2$. A subsequent heterodyne experiment in the presence of the LO is then performed to obtain φ from the temporal and/or spectral interference fringes. In cases (such as, but not limited to, a collinear geometry) where the phase stability is high, it is an attractive prospect to extract $|\mathbf{E}_{\mathrm{S}}|$ and the phase in a single experimental configuration, without removing the LO. The model developed to describe the shape of the interference fringes is based upon the PSU tilt angle, wavelength, and the dispersion due to the optical elements placed between sample-originating and LO sum-frequency fields.[37] Previously, a fit of the model to measured fringes resulted in only φ_{S}, as it was applied to normalized data. Omission of the normalization step allows for extraction of the magnitude of both the sample and local oscillator fields at each IR energy.

The intensity, I_{SFG}, of the SF signal resulting from the interference of the sample and LO sum-frequency signals is proportional to the square of the sum of the input fields

$$\begin{aligned} I_{\mathrm{SFG}} &= |\mathbf{E}_{\mathrm{S}} + \mathbf{E}_{\mathrm{LO}}|^2 \\ &= |\mathbf{E}_{\mathrm{S}}|^2 + |\mathbf{E}_{\mathrm{LO}}|^2 + 2|\mathbf{E}_{\mathrm{S}}||\mathbf{E}_{\mathrm{LO}}| \cos \Delta\varphi, \end{aligned} \tag{4.4}$$

where $\Delta\varphi$ is their phase difference. In our geometry, the infrared, visible and local oscillator SF fields are each attenuated as they pass through the PSU. This attenuation is dependent upon PSU tilt angle and may be accounted for with wavelength-dependent Fresnel coefficients. The total attenuation is a product of the attenuation upon crossing the air–PSU and PSU–air interfaces

$$(tt)_\omega \equiv t_{\mathrm{air|PSU}}(\omega,\alpha)\cdot t_{\mathrm{PSU|air}}(\omega,\alpha) \tag{4.5}$$

where each t factor on the right-hand side of Eq. 4.5 is a standard Fresnel field transmission coefficient. The sample SF field will be affected by the attenuation of the incident visible and IR fields while the local oscillator SF field is attenuated directly by the PSU. Accounting for these factors results in

$$\begin{aligned} I'_{\mathrm{SFG}} &= |(tt)_{\mathrm{IR}}(tt)_{\mathrm{vis}}\mathbf{E}_{\mathrm{S}} + (tt)_{\mathrm{SFG}}\mathbf{E}_{\mathrm{LO}}|^2 \\ &= |(tt)_{\mathrm{IR}}(tt)_{\mathrm{vis}}|^2|\mathbf{E}_{\mathrm{S}}|^2 + \ |(tt)_{\mathrm{SFG}}|^2|\mathbf{E}_{\mathrm{LO}}|^2 + \\ &\quad 2|(tt)_{\mathrm{IR}}(tt)_{\mathrm{vis}}(tt)_{\mathrm{SFG}}||\mathbf{E}_{\mathrm{S}}||\mathbf{E}_{\mathrm{LO}}|\cos\Delta\varphi, \end{aligned} \tag{4.6}$$

and, if both sides are divided by $|\mathbf{E}_{\mathrm{LO}}|^2$ and f is substituted for $|\mathbf{E}_{\mathrm{S}}|/|\mathbf{E}_{\mathrm{LO}}|$,

$$I'_{\mathrm{SFG}} = \left(|(tt)_{\mathrm{IR}}(tt)_{\mathrm{vis}}|^2 f^2 + |(tt)_{\mathrm{SFG}}|^2 + |(tt)_{\mathrm{IR}}(tt)_{\mathrm{vis}}(tt)_{\mathrm{SFG}}|f\cos\Delta\varphi\right)|\mathbf{E}_{\mathrm{LO}}|^2. \tag{4.7}$$

Finally, as indicated by Eq. 4.1, $\Delta\varphi$ is the sum of the phase shifts due to each of the optical components between the LO and sample positions. For each of the static optics,

$$\Delta\varphi_j = \frac{d_n}{c}[n_{\mathrm{SFG}}\omega_{\mathrm{SFG}} - n_{\mathrm{vis}}\omega_{\mathrm{vis}} - n_{\mathrm{IR}}\omega_{\mathrm{IR}}]. \tag{4.8}$$

where c is the speed of light in vacuum. In the case of the rotating phase shifting unit, the appropriate expression is

$$\Delta\varphi_{\mathrm{PSU}} = \frac{d_{\mathrm{PSU}}}{c}[n_{\mathrm{SFG}}\omega_{\mathrm{SFG}}\cos\beta_{\mathrm{SFG}} - n_{\mathrm{vis}}\omega_{\mathrm{vis}}\cos\beta_{\mathrm{vis}} - n_{\mathrm{IR}}\omega_{\mathrm{IR}}\cos\beta_{\mathrm{IR}}], \tag{4.9}$$

with β_i as the refracted angle of the beams within the PSU. Using Eqs. 4.1 and 4.7–

4.9, the model can be fit to the measured interferograms and $\mathbf{E}_\mathrm{S}$ and $\Delta\phi_{\mathrm{S \cdot LO}}$ are thus obtained.

4.3.3 Demonstration at the OTS surface

Data for two-dimensional interferograms were collected for z-cut quartz and OTS surfaces, collected over the wavelength region containing the aliphatic C–H vibrational modes of OTS. The pattern displayed by the z-cut quartz sample (Figure 4.3a) is exemplary of what we expect for the temporal and spectral interference between a nonresonant local oscillator and nonresonant sample. The curvature of the spectral fringes results from the dispersion of the beams through all optics (Eq. 4.1) between the LO source and the sample.[37] The horizontal stripes result from the changing multiple beam interference conditions inside the y-cut quartz as the IR energy is varied.

Inspecting the OTS interferograms in Figure 4.3c, we can see that the pattern is significantly altered in the presence of vibrational resonances. Since the multiple beam interference stripes are overlaid on the spectral features, close examination of the sample $\chi^{(2)}$ response must follow fitting of the temporal fringes. The interference has a much more pronounced effect on the visible (pump and SFG) beams since their wavelength is approximately an order of magnitude shorter than that of the IR beam. Since the wavelength of the visible beam is fixed in the experiment, the effect of the interference on its amplitude and phase is constant, and the same for the OTS and quartz reference sample. However, this is not the case for $\mathbf{E}_\mathrm{LO}$ as it approaches the sample with varying amplitude as the IR energy is scanned. In the fit of the temporal fringes (as demonstrated in Jena et al.[37]) we extract $\mathbf{E}_\mathrm{LO}$ and $\mathbf{E}_\mathrm{S}$, thereby removing the effect of variation of $\mathbf{E}_\mathrm{LO}$ on $\mathbf{E}_\mathrm{S}$. In cases where the fringe visibility is low (where there is no resonant contribution from the OTS), we cannot sufficiently resolve the fringes to extract any phase information. These regions, below $2825\,\mathrm{cm}^{-1}$, near $2895\,\mathrm{cm}^{-1}$, and above $2970\,\mathrm{cm}^{-1}$ are indicated by the horizontal dashed lines in Figure 4.3c.

We now process the data in these images (using the method described in Section 4.3.2) according to the following procedure. From fits to the individual PSU scans (for example, as shown in Fig. 4.3b and d), $\mathbf{E}_\mathrm{S}$, $\mathbf{E}_\mathrm{LO}$, and $\Delta\varphi$ are obtained for the z-cut quartz and OTS sample at each IR energy. Details of this fitting to temporal slices of these images is given in Jena et al.[37] Since both samples represent cases of external reflection at air–dielectric interfaces, the set of Fresnel coefficients that relate the fields $\mathbf{E}_\mathrm{S}$ to the effective susceptibility tensor elements $\chi^{(2)}_\mathrm{S}$ are real and have the same signs for OTS and z-cut quartz. We infer the magnitude of $\chi^{(2)}_\mathrm{S}$ from the magnitude of $\mathbf{E}_\mathrm{S}$ obtained for OTS. In Figure 4.4a, this is plotted for each IR wavenumber for which sufficient fringe visibility was obtained (that is, excluding the hatched regions). The absolute phase of the OTS nonlinear susceptibility is obtained by comparison of the OTS and quartz relative phases, followed by a correction based on the absolute phase ($\varphi_\mathrm{ref} = -\pi/2$ rad) previously determined for our quartz reference sample in the same orientation.[25]

$$\varphi_\mathrm{S} = \Delta\varphi_\mathrm{S} - \Delta\varphi_\mathrm{ref} + \varphi_\mathrm{ref} \tag{4.10}$$

A plot of φ_S as a function of IR energy appears in Figure 4.4b. Since the imaginary components of $\chi^{(2)}_\mathrm{S}$ are often more qualitatively revealing of the sample resonances, it is desirable to plot the acquired magnitude and phase of the response in terms of real (Figure 4.4c) and imaginary components (Figure 4.4d). We note that our OTS phase spectrum is shifted by 180° (hence real and imaginary spectra have different signs) compared to that presented in Ji et al.[7] Our assignment of $\mathrm{Im}[\chi^{(2)}_\mathrm{S}] < 0$ for the CH_3 symmetric stretch, in the case of the methyl group directed away from the surface, is in agreement with what has been determined for other aliphatic methyl groups by experiment[24,33,130] and calculation.[25] Furthermore, calculation of dipole moment and polarizability derivatives[25] follows the same sign convention as used to calculate the SFG response for the air–water interface[131–133] to produce air–water $\chi^{(2)}$ real/imaginary spectra with the same sign as those observed experimentally.[32,35,134]

We emphasize that, until now, the discussion has referred to only the data points in Figure 4.4, ignoring the solid lines. One advantage of phase-resolved SFG experiments is that no line shape need be assumed in order to arrive at these spectral features. At this point, it is useful to introduce a model of the sample response. A popular choice is to use a complex Lorentzian function such as

$$\chi^{(2)}_{\mathrm{S}}(\omega_{\mathrm{IR}}) = A_{\mathrm{NR}} + \sum_k \frac{A_k}{\omega_k - \omega_{\mathrm{IR}} - i\Gamma_k} \tag{4.11}$$

where each of k resonant modes is described with an amplitude A_k, resonance frequency ω_k, and linewidth Γ_k. Here A_{NR} represents an additional non-resonant contribution, and $i = \sqrt{-1}$. The real and imaginary components of this can be written as

$$\begin{aligned} \mathrm{Re}[\chi^{(2)}_{\mathrm{S}}(\omega_{\mathrm{IR}})] &= A_{\mathrm{NR}} + \sum_k \frac{A_k(\omega_k - \omega_{\mathrm{IR}})}{(\omega_k - \omega_{\mathrm{IR}})^2 + \Gamma_k^2} \\ \mathrm{Im}[\chi^{(2)}_{\mathrm{S}}(\omega_{\mathrm{IR}})] &= \sum_k \frac{A_k\Gamma_k}{(\omega_k - \omega_{\mathrm{IR}})^2 + \Gamma_k^2} \end{aligned} \tag{4.12a}$$

in the case where the non-resonant response is purely real, as expected at a dielectric surface. We then simultaneously fit Eq. 4.12a to the data in Figure 4.4c, and Eq. 4.12b to the data in Figure 4.4d. The resulting parameters are shown in Table 4.1, and are in good agreement with those obtained in other SFG studies of OTS films.[7,129,135] The lineshape obtained with these best-fit parameters is overlaid on the data with the solid lines in Figure 4.4. Although fitting is not required in order to arrive at the real

mode	A_i	ω_i / cm^{-1}	Γ_i / cm^{-1}
NR	-0.040	–	–
d^+	3.3	2842	17
d_w^+	-0.32	2849	18
r^+	-3.6	2879	5.4
d_w^-	0.72	2889	5.2
r_{FR}^+	-5.2	2942	9.1
r^-	2.2	2962	12

Table 4.1: Results of simultaneous fits of real and imaginary line shapes (Eqs. 4.12a and b) to the measured real and imaginary spectra (Figures 4.4c and d) of OTS.

and imaginary spectra of $\chi_{\mathrm{S}}^{(2)}$, it may be used to provide further interpretation of the data. For example, it has been illustrated that the d_w^+ resonance near 2850 cm^{-1}, when weak in homodyne experiments, is more evident in the real and imaginary spectra.[7] Another study has demonstrated that the relative intensities of all these resonances, especially the contribution of the 2850 cm^{-1} peak, is strongly dependent on the OTS film preparation conditions.[129] Phase-resolved SFG spectroscopy therefore provides a robust and sensitive method of characterizing the surface structure. Furthermore, although there are regions where no interference is observed due to low response from the sample (hatched regions in Figure 4.4), a model such as that in Eq. 4.11 may be used to connect and extend these regions, as shown in Figure 4.4c and d.

4.4 Conclusions

We have demonstrated a procedure for simultaneously extracting the magnitude and phase of a sample's SFG response from fitting the interference fringes obtained in a heterodyne SFG experiment. This allows the experiment to be performed in a fixed configuration, without removing the local oscillator to measure the the magnitude in a separate homodyne experiment. We illustrate that such a scheme is particularly attractive for experiments with high phase stability, such as those performed in a collinear pump geometry. We have provided a demonstration of this for aliphatic C–H stretching at the OTS–air interface.

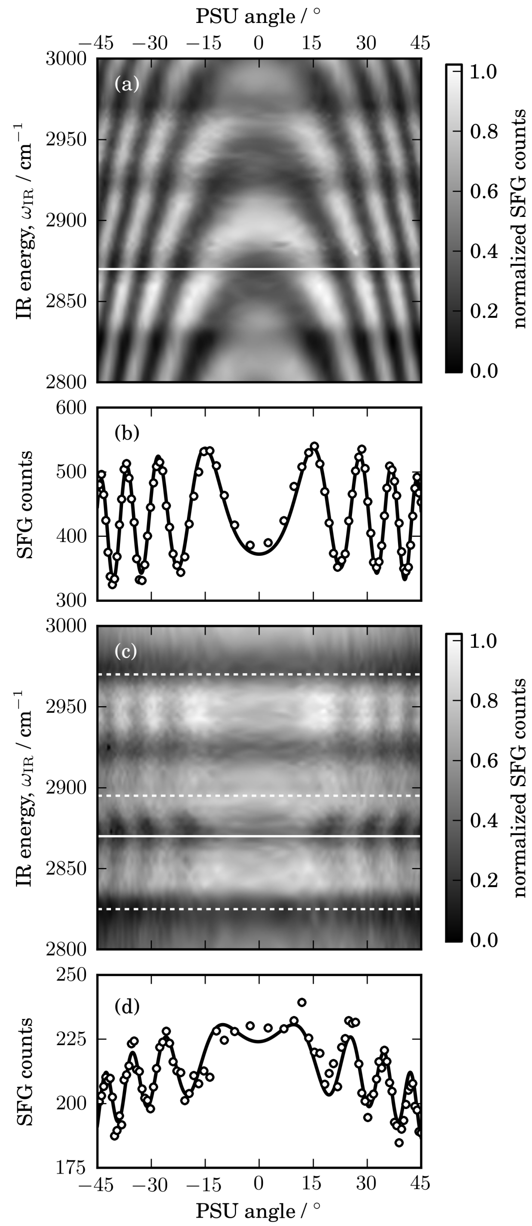

Figure 4.3: (a) Two-dimensional interferometric sum-frequency data collected at the z-cut quartz–air interface. Temporal fringes are observed along the horizontal axis as the PSU is scanned; spectral fringes are observed along the vertical axis as the IR energy is varied. The horizontal line at $\omega_{IR} = 2870$ cm^{-1} indicates the IR energy at which (b) a scan of the PSU is shown along with a fit to Eq. 4.6. The same is shown in (c) for the OTS–air interface. Here spectral regions below 2825 cm^{-1}, in the vicinity of 2895 cm^{-1}, and above 2970 cm^{-1}, indicated with dashed lines, are those for which the OTS fringe visibility was not sufficient for quantitative analysis. (d) An OTS PSU scan at $\omega_{IR} = 2870$ cm^{-1}.

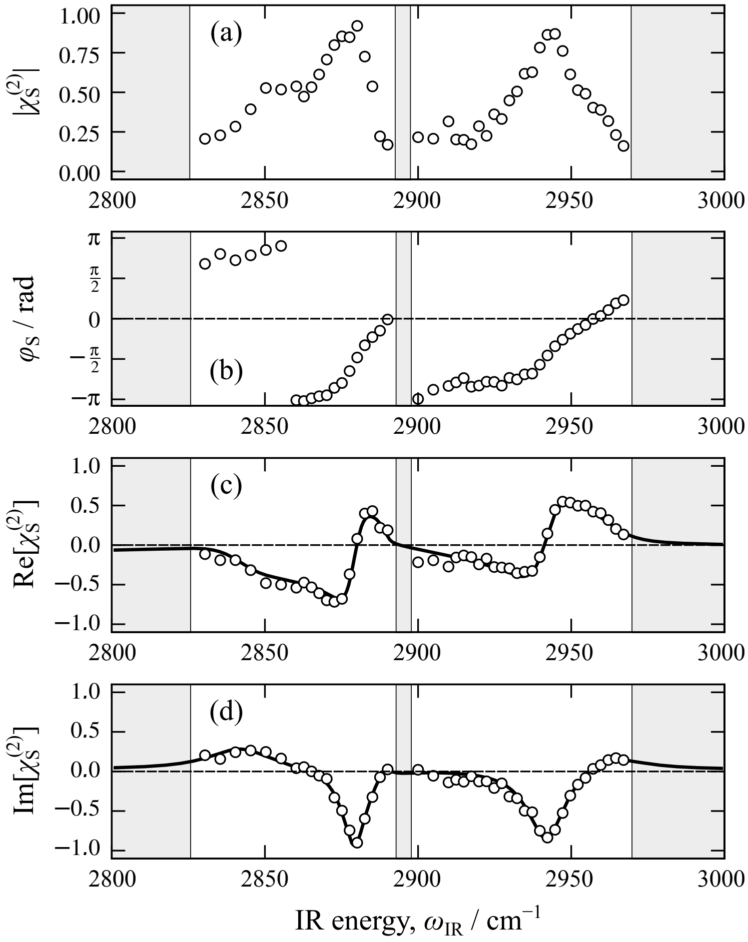

Figure 4.4: OTS $\chi_S^{(2)}$ spectra displayed as (a) measured magnitude, (b) measured phase, (c) calculated real, and (d) calculated imaginary components. The hatched regions at IR energies below 2825 cm^{-1}, around 2895 cm^{-1}, and above 2970 cm^{-1} indicate areas where, due to low sample response, the fringe visibility was not sufficient for determining any parameters from the temporal interference profiles. Points indicate data; lines represent a fit using Eq. 4.12.

Chapter 5

Direct Measurement of Gold Surface Nonlinear Susceptibility

Reproduced in part from Covert, P. A.; Hore, D. K. "Assessing the Gold Standard: Measurement of the Complex Nonlinear Susceptibility of Metals" *J. Phys. Chem. C,* **119,** 271–276 (2015). Copyright 2015 American Chemical Society.

5.1 Introduction

Ward et al. first demonstrated the utility of gold as a phase reference by recording an inversion in the direction of the peaks assigned to the methyl symmetric stretch upon flipping the polarity of the methyl group, thereby changing the sign of the relevant susceptibility tensor elements.[136] Two interfaces were studied in their experiment: a self-assembled monolayer (SAM) of 1-octadecanethiol (ODT) on gold, and octadecanol adsorbed to a deuterated ODT monolayer on gold (data reproduced in Figure 5.1). In the first case, the terminal methyl group of ODT provides the resonant response and is pointed away from the interface. In the second case, it is the terminal methyl group on octadecanol, which is oriented towards the interface, that provides

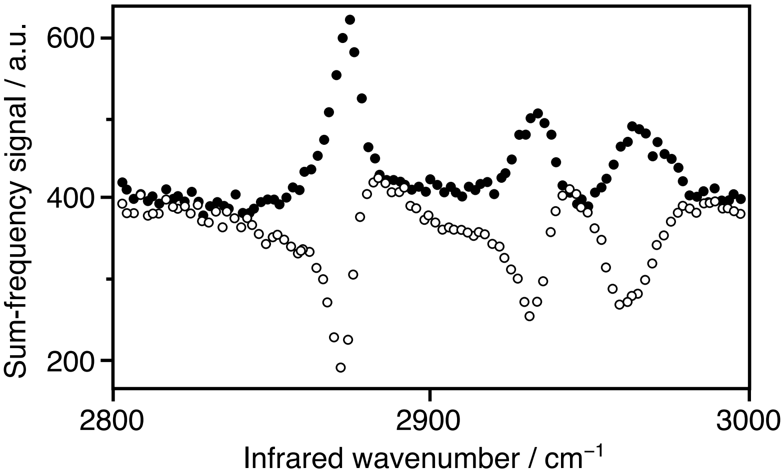

Figure 5.1: Sum-frequency spectra in the C–H stretching region with the electric fields of the visible and infrared lasers and the emitted sum-frequency light all p-polarized. Solid circles represent the monolayer of octadecanethiol on gold in contact with water. Open circles represent the monolayer of d_{37}-octadecanethiol on gold in contact with a saturated aqueous solution of dodecanol. Adapted with permission from Ward et al.[136] Copyright 1993 American Chemical Society.

the resonant response. The nonresonant response from gold provides the background signal that interferes constructively with the ODT methyl response to provide the upwards-pointing peaks, and destructively with the response from the octadecanol methyl group resulting in downwards-pointing peaks. The versatility of this method is evidenced by the range of molecules and interfaces it has since been applied to, providing phase information from polymer–metal interfaces,[137] lipid bilayers and cell structures,[138–140] monolayers,[141–145] and immobilized proteins.[146,147]

The above method for phase detection allows the *relative* phase of the resonant modes to be determined. In some cases, where the vibrational modes are clearly identified, unambiguously assigned, and of known polarity, fitting of the data may also retrieve the phase of the gold nonresonant response (φ_{NR}). However, previous measurements have shown that it is inappropriate to choose a single value for φ_{NR}. Measurements by second-harmonic generation (SHG) methods[148] and by SFG[149] have shown a strong phase dependence upon excitation wavelength in the visible region.

In addition, the phase has been observed to vary as a function of ODT coverage,[148] a dependence that has been attributed to changes to the electronic structure of the metal with surface binding.[149] This has also been observed on a variety of other metals, including studies of lateral heterogeneity revealed by SFG microscopy.[150–152] It is therefore desirable to know, from independent measurement, the value of the nonresonant phase, as this enables comparison of SFG phase spectra from dissimilar samples.

Heterodyne SFG methods, calibrated against an external reference material, have the ability to measure phase directly, with high accuracy and precision, and without the need to assign surface vibrational features of known polarity. In this chapter, the phase of the second-order nonresonant susceptibility of ODT–Au is measured directly by heterodyne SFG and indirectly by conventional homodyne SFG. Since the SFG responses of gold and ODT interfere in the near field, while the heterodyne local oscillator/ODT–Au interference occurs in the far field, comparison of the two must take into account both magnitude and phase of the local field corrections. Comparison of the results from the two methods has enabled us to formulate a protocol that allows the phase of any material, dielectric or metal, to be determined.

5.2 Experimental Methods

Sample preparation Self-assembled monolayers of 1-octadecanethiol (Sigma-Aldrich) on gold were prepared following the method of Bain et al.[153] Commercially available (EMF, Ithaca, NY) squares of 100 nm Au over 5 nm Cr on float glass were cleaned by sonication in acetone followed by anhydrous ethanol. The cleaned gold substrates were submersed in a $1\,\mathrm{mmol\,L^{-1}}$ solution of ODT in anhydrous ethanol overnight. Following the self-assembly, residual ODT that may have been adsorbed to the SAM surface was removed by four sequential soaks in fresh, anhydrous ethanol. Prepared ODT–Au samples were stored in anhydrous ethanol until ready for use, at which time they were dried under an N_2 gas stream.

SFG measurements In order to establish a technique for comparing the SFG phase response from metal and dielectric substrates, the phase of the nonlinear susceptibility was examined by two independent methods. In both methods, spectra were collected using the laser and parametric generator described in Chapter 2. Spectra were measured over an IR frequency range of 2800 to 3050 cm^{-1}. Visible and infrared beams approached the sample in collinear geometry at a 50° angle of incidence. Beam diameters at the sample were approximately 0.5 mm. At the sample, the visible beam energy was 30 µJ/pulse and the IR beam energy was 90 µJ/pulse. The visible and IR beams were s- and p-polarized, respectively. The s-polarized component of the SFG response was measured. A direct measurement of the phase of $\chi^{(2)}$ was made using the heterodyne SFG techniques presented Chapters 2 and 4. Experimental conditions were the same as for the homodyne measurements with the addition of a 50 μm thick piece of y-cut quartz (Del Mar Photonics, CA) as the local oscillator (LO) generator, and a 1 mm thick fused silica plate as the phase shifting unit (PSU) used to generate the interference fringes that contain the phase information. The components of our experimental setup specific to phase measurement are illustrated in Figure 5.2, and are described in detail in the Results and Discussion.

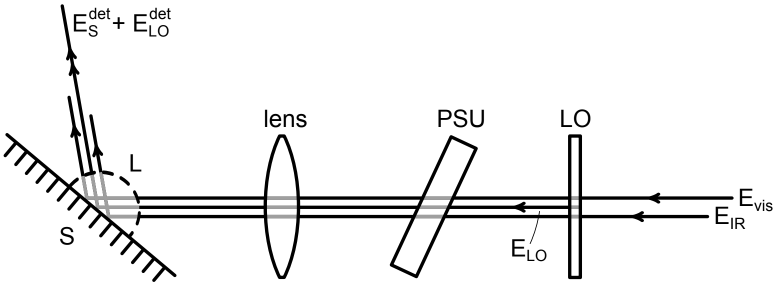

Figure 5.2: Schematic of the optical elements and fields explicitly included in the calculation of relative phase. The phases of the electric fields $\mathbf{E}_{\text{vis}}$, $\mathbf{E}_{\text{IR}}$, and $\mathbf{E}_{\text{LO}}$ are affected as they pass through the phase shifting unit (PSU) and lens and into the local field (L) on their way to the sample (S). The phases are again affected as they pass from the local field into the far field and to the detector.

5.3 Results and Discussion

5.3.1 Homodyne Results

ODT is a long-chain aliphatic molecule with a thiol head group at one end that readily binds to metal surfaces.[153] A well ordered ODT SAM on gold consists of covalently bound sulfur atoms in a close-packed configuration with the alkyl chains extending away from the gold surface. In this configuration the terminal methyl groups form an ordered, hydrophobic surface. The homodyne spectrum of the ODT–Au surface (open circles, Figure 5.3) exhibits two strong, downward-pointing peaks and several smaller peaks superimposed on a nonresonant response from gold.

The homodyne spectrum has been fit to

$$I_{\text{SFG}}(\omega_{\text{IR}}) \propto |L_{yy}(\omega_{\text{SFG}})e_y \cdot L_{yy}(\omega_{\text{vis}})e_y \cdot L_{zz}(\omega_{\text{IR}})e_z \cdot \chi^{(2)}(\omega_{\text{IR}})|^2 \qquad (5.1)$$

where L_{ii} are components of the local field tensor,[6,71,106,154] e_i are elements of the unit

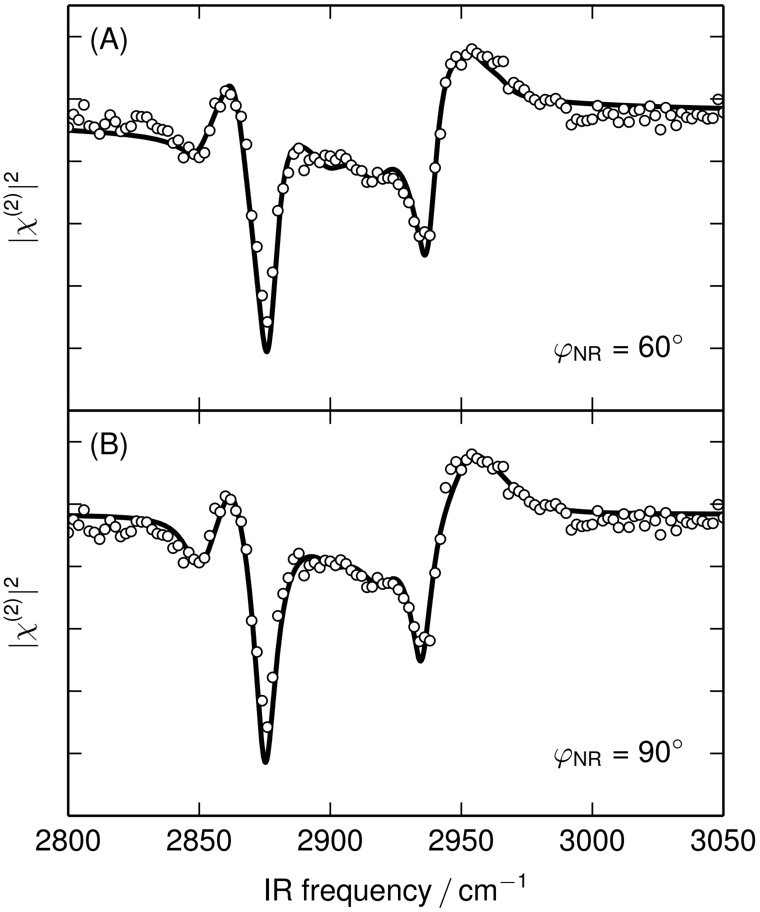

Figure 5.3: Homodyne spectrum of ODT–Au surface, corrected for local field effects, fit to two different parameterizations of the $\chi^{(2)}$ dispersion equation (Eq. 5.2). Experimental data are represented by the circles, and fits using two different values of φ_{NR} are shown by solid lines in panels A and B. The residual sum of squares for each of the fits is the same to three significant figures.

polarization vector, and $\chi^{(2)}(\omega_{\mathrm{IR}})$ is the dispersion expression

$$\chi^{(2)}(\omega_{\mathrm{IR}}) = A_{\mathrm{NR}} e^{i\varphi_{\mathrm{NR}}} + \sum_n \frac{A_n}{\omega_n - \omega_{\mathrm{IR}} - i\Gamma_n}. \tag{5.2}$$

A_{NR} and φ_{NR} are the magnitude and phase of the nonresonant surface nonlinear susceptibility ($\chi^{(2)}_{\mathrm{NR}} = A_{\mathrm{NR}} e^{i\varphi_{\mathrm{NR}}}$) of ODT–Au, and A_n, ω_n, and Γ_n are the amplitude, frequency, and width of each of the n ODT resonant modes. Eight vibrational modes[155,156] were included in fits of the model given in eq 5.2 to the data. The major peaks at 2877 and 2937 cm^{-1} result from the symmetric stretch of the terminal methyl group on ODT. Methylene modes at 2850, 2902, and 2918 cm^{-1} are likely due to some *trans-gauche* defects in the aliphatic chains.[157]

We have attempted to fit the data with a broad range of φ_{NR}, noting that reasonable results could be obtained if the amplitudes and widths of the resonant terms were allowed to vary. In all cases, the frequencies were within 1 cm^{-1} of previously reported values. Among these fits, the best results were obtained in the range $60° < \varphi_{\mathrm{NR}} < 90°$. The $\varphi_{\mathrm{NR}} = 60°$ and 90° cases shown in Figure 5.3 have sums of squares of residuals that are identical to three significant figures. Outside of this range, it was not possible to accurately reproduce the SFG intensity line shape. This is a result of the phase information encoded in the interference between the nonresonant contribution and the resonant modes.

In each case, analogous fits could be obtained if the signs of all A_n were changed along with a 180° change in φ_{NR}, since the spectral intensities are the square of the effective susceptibility as written in eq 5.1. In this case, it is of particular interest that the methyl symmetric stretch has been assigned $A < 0$. In our convention, the resonant terms in eq 5.2 have a denominator defined in a such a way that the numerator is

$$A_n = \frac{1}{2m_n\omega_n}\left(\frac{\mathrm{d}\alpha_{yy}^{(1)}}{\mathrm{d}Q}\right)_n\left(\frac{\mathrm{d}\mu_z}{\mathrm{d}Q}\right)_n \tag{5.3}$$

where m_n is the reduced mass, $\alpha_{yy}^{(1)}$ is the linear polarizability, μ_z is the dipole moment, and Q is the normal mode coordinate. The derivatives $\mathrm{d}\alpha_{yy}^{(1)}/\mathrm{d}Q$ and $\mathrm{d}\mu_z/\mathrm{d}Q$ represent a harmonic approximation to the Raman transition polarizability and IR transition dipole moment, respectively. A combination of previous phase-resolved SFG studies and calculations of these derivatives have established that, for the CH_3 symmetric stretch, $A < 0$ corresponds to the methyl group pointing away from the surface.[24,25,33,130] As a result we can conclude that φ_{NR} lies within the 60–90° range (as opposed to 240–270°), thereby resolving the 180° phase ambiguity.

5.3.2 Heterodyne Results

Fringes shown in Figure 5.4A result from interference of the local oscillator with SFG signal generated at the ODT–Au surface. The data were fit to a model of the fringe shape,[37,158] which accounts for the phase shifting effects of the PSU and lens (Figure 5.2), to obtain the ODT–Au relative phase spectrum (open circles, Figure 5.4B). Similar data were collected and analyzed over the same frequency domain for a z-cut quartz reference sample to generate the reference phase spectrum (filled circles, Figure 5.4B). The structure superimposed on the general positive slope of the ODT–Au relative phase trace correlates with the strong vibrational modes observed in the homodyne spectrum. In contrast, the relative phase of the z-cut quartz sample increases in a nearly linear fashion with increasing IR frequency. Multiple beam interference in the y-cut quartz LO generator result in small oscillations superimposed on the phase spectra. These are most clear in the case of the z-cut quartz, as the resonances in the gold sample obscure this phenomenon. These artifacts cancel each other in the

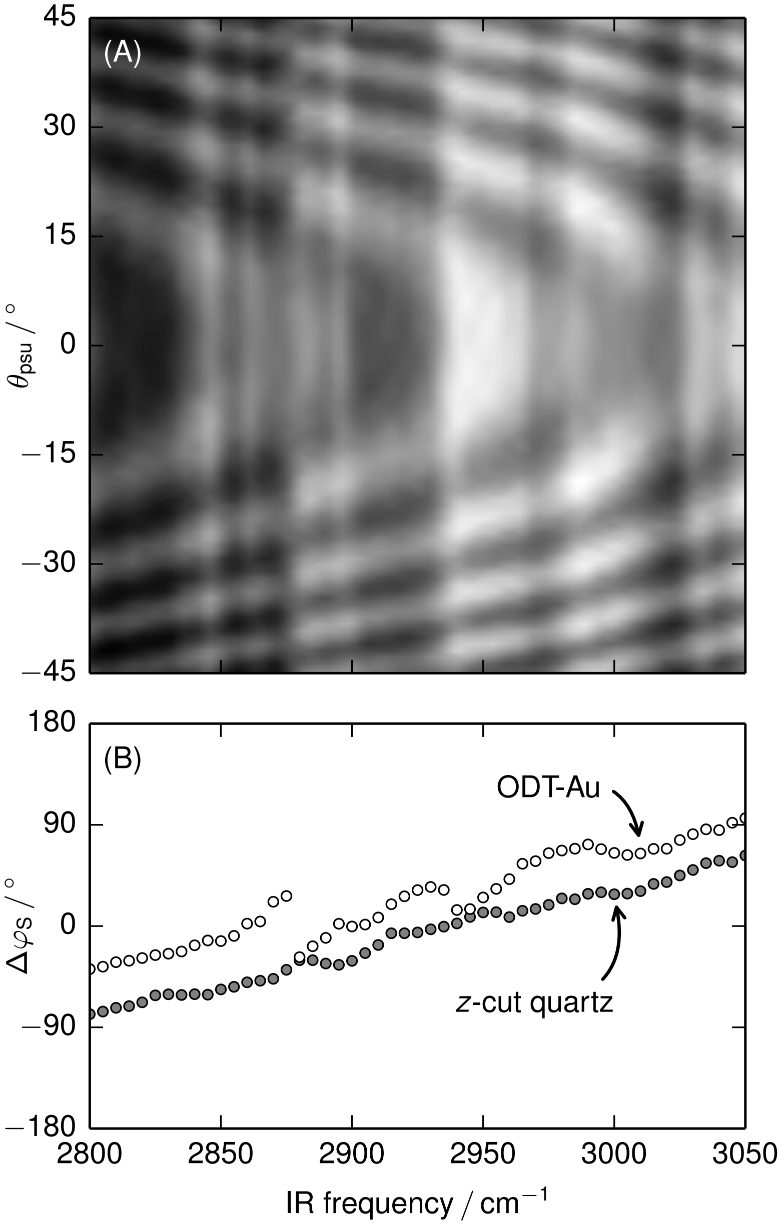

Figure 5.4: (A) Interference fringes measured from the ODT–Au surface were fit to obtain (B) the phase relative to the local oscillator. Identical measurement and analysis was performed to generate the relative phase spectrum of the z-cut quartz sample.

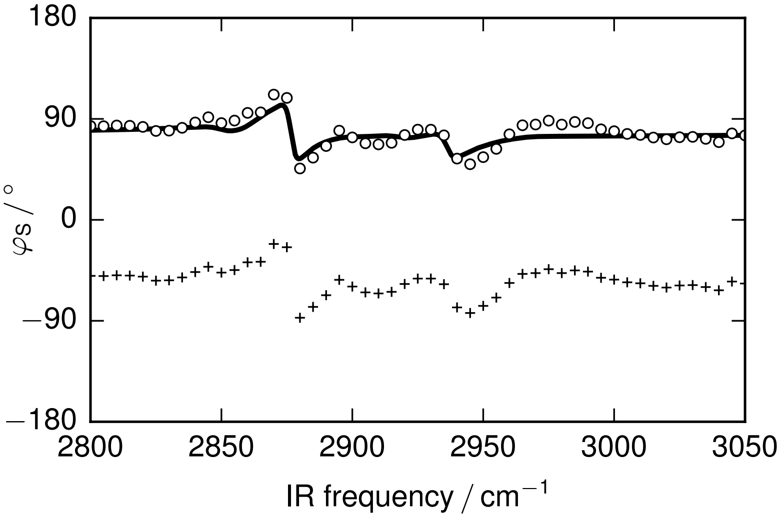

Figure 5.5: The absolute phase of ODT–Au, calculated from heterodyne detection data, and neglecting local field effects (crosses), differs from the phase obtained from a fit of the homodyne data (solid line) by approximately 135°. Absolute phase calculated, accounting for the local field effects (circles), resolves this discrepancy.

absolute phase calculation.

In prior work, the absolute phase of the SFG signal was found to be simply related to the difference in relative phase between the sample and reference. Treatment of the data in this manner results in the phase spectrum indicated by the crosses in Figure 5.5, revealing a discrepancy of approximately 135° between the heterodyne and homodyne (solid line in Figure 5.5) methods. In such a treatment, only the optics between the LO and sample were explicitly accounted for in terms of their phase shifting behavior. That followed the assumption that any additional shifts in the relative phases of the sample and local oscillator signals were common to both and may therefore be ignored. This assumption is valid in cases where the sample and reference materials are both dielectrics. It is not valid, however, when comparing signals from a metal surface to signals from a dielectric surface. This stems from the fact that, unlike a dielectric, the phase shift by reflection from a metal is not restricted to 0° or 180°. We now present an approach that takes this difference into account and shows that the local field may be treated, conceptually, like an additional optic placed in the beam path between the LO and sample.

In our experimental configuration, a phase shift is introduced to the incident visible and infrared fields ($\mathbf{E}_{\text{vis}}$ and $\mathbf{E}_{\text{IR}}$, respectively) and the local oscillator field ($\mathbf{E}_{\text{LO}}$) by the phase shifting unit (PSU), lens, and local field corrections ($\mathbf{L}$) as they propagate to the sample surface (Figure 5.2). The observed fringes (Figure 5.4A) result from an interference of the sample and local oscillator SFG signals at the detector. The sum frequency field $\mathbf{E}_{\text{LO}}$ is generated as $\mathbf{E}_{\text{vis}}$ and $\mathbf{E}_{\text{IR}}$ pass through the LO. In the context of this problem, the fixed phases of the three fields (φ_{vis}, φ_{IR}, and φ_{LO}) are defined at the point they exit the LO.

The local oscillator field at the detector has been modified by transmission through the PSU and lens and by reflection from the sample

$$\mathbf{E}_{\text{LO}}^{\text{det}} = \mathbf{r}_{\text{S}}(\omega_{\text{SFG}}) \cdot \mathbf{M}_{\text{lens}}(\omega_{\text{SFG}}) \cdot \mathbf{M}_{\text{PSU}}(\omega_{\text{SFG}}) \cdot \mathbf{E}_{\text{LO}}, \tag{5.4}$$

where $\mathbf{r}_{\text{S}}$, $\mathbf{M}_{\text{lens}}$, and $\mathbf{M}_{\text{PSU}}$ are the complex-valued, wavelength dependent operators describing the effects of the gold surface, lens, and PSU upon both the intensity and phase of the field. The sample SFG field at the detector is likewise influenced by the PSU, lens, and local field

$$\begin{aligned}\mathbf{E}_{\text{S}}^{\text{det}} = \mathbf{L}_{\text{S}}(\omega_{\text{SFG}}) \cdot \chi_{\text{S}}^{(2)} \cdot \mathbf{L}_{\text{S}}(\omega_{\text{vis}}) \cdot \mathbf{M}_{\text{lens}}(\omega_{\text{vis}}) \cdot \mathbf{M}_{\text{PSU}}(\omega_{\text{vis}}) \cdot \mathbf{E}_{\text{vis}} \\ \times \mathbf{L}_{\text{S}}(\omega_{\text{IR}}) \cdot \mathbf{M}_{\text{lens}}(\omega_{\text{IR}}) \cdot \mathbf{M}_{\text{PSU}}(\omega_{\text{IR}}) \cdot \mathbf{E}_{\text{IR}}\end{aligned} \tag{5.5}$$

where $\mathbf{L}_{\text{S}}$ is the local field tensor for the sample.

The phase components of Eqs. 5.4 and 5.5 may be isolated and written as the sum of the individual phase contributions. The absolute phase of the local oscillator signal at the detector is

$$\varphi_{\mathrm{LO}}^{\mathrm{det}} = \varphi_{\mathrm{LO}} + \Delta\varphi_{\mathrm{PSU}}(\omega_{\mathrm{SFG}}) + \Delta\varphi_{\mathrm{lens}}(\omega_{\mathrm{SFG}}) + \Delta\varphi_{r,\mathrm{S}}(\omega_{\mathrm{SFG}}) \tag{5.6}$$

and the absolute phase of the sample SFG response at the detector is

$$\begin{aligned}\varphi_{\mathrm{S}}^{\mathrm{det}} = \varphi_{\mathrm{IR}} + \Delta\varphi_{\mathrm{PSU}}(\omega_{\mathrm{IR}}) + \Delta\varphi_{\mathrm{lens}}(\omega_{\mathrm{IR}}) + \Delta\varphi_{L,\mathrm{S}}(\omega_{\mathrm{IR}}) + \varphi_{\mathrm{vis}} + \Delta\varphi_{\mathrm{PSU}}(\omega_{\mathrm{vis}}) \\ + \Delta\varphi_{\mathrm{lens}}(\omega_{\mathrm{vis}}) + \Delta\varphi_{L,\mathrm{S}}(\omega_{\mathrm{vis}}) + \varphi_{\mathrm{S}} + \Delta\varphi_{L,\mathrm{S}}(\omega_{\mathrm{SFG}}).\end{aligned} \tag{5.7}$$

The positions and spacing of the measured interference fringes are dictated by the relative phase of the sample with respect to the local oscillator

$$\Delta\varphi_{\mathrm{S}}^{\mathrm{det}} = \varphi_{\mathrm{S}}^{\mathrm{det}} - \varphi_{\mathrm{LO}}^{\mathrm{det}}. \tag{5.8}$$

Expansion of the above expression and collection of terms yields

$$\Delta\varphi_{\mathrm{S}}^{\mathrm{det}} = \varphi_{\mathrm{S}} - \varphi_{\mathrm{LO}} + \varphi_{\mathrm{vis}} + \varphi_{\mathrm{IR}} - \Delta\varphi_{\mathrm{PSU}} - \Delta\varphi_{\mathrm{lens}} + \Delta\varphi_{L,\mathrm{S}} - \Delta\varphi_{r,\mathrm{S}}(\omega_{\mathrm{SFG}}), \tag{5.9}$$

where

$$\Delta\varphi_{\mathrm{PSU}} \equiv \Delta\varphi_{\mathrm{PSU}}(\omega_{\mathrm{SFG}}) - \Delta\varphi_{\mathrm{PSU}}(\omega_{\mathrm{vis}}) - \Delta\varphi_{\mathrm{PSU}}(\omega_{\mathrm{IR}}) \tag{5.10}$$

and

$$\Delta\varphi_{\mathrm{lens}} \equiv \Delta\varphi_{\mathrm{lens}}(\omega_{\mathrm{SFG}}) - \Delta\varphi_{\mathrm{lens}}(\omega_{\mathrm{vis}}) - \Delta\varphi_{\mathrm{lens}}(\omega_{\mathrm{IR}}) \tag{5.11}$$

are the total phase shifts by the PSU and lens[37,158] and

$$\Delta\varphi_{L,\mathrm{S}} \equiv \Delta\varphi_{L,\mathrm{S}}(\omega_{\mathrm{SFG}}) + \Delta\varphi_{L,\mathrm{S}}(\omega_{\mathrm{vis}}) + \Delta\varphi_{L,\mathrm{S}}(\omega_{\mathrm{IR}}) \tag{5.12}$$

is the total phase shift imparted by the local field.

To this point all comparisons of the sample phase have been with respect to the local oscillator phase at the detector, which is not constant as a function of wavelength. In order to obtain the absolute phase of the sample, comparison with a reference sample of known phase is needed. The difference in the relative phases of the sample and reference is given as

$$(\Delta\varphi_{\mathrm{S}}^{\mathrm{det}} - \Delta\varphi_{\mathrm{ref}}^{\mathrm{det}}) = \varphi_{\mathrm{S}} - \varphi_{\mathrm{ref}} + \Delta\varphi_{\mathrm{L,S}} - \Delta\varphi_{\mathrm{L,ref}} - \Delta\varphi_{r,\mathrm{S}}(\omega_{\mathrm{SFG}}) + \Delta\varphi_{r,\mathrm{ref}}(\omega_{\mathrm{SFG}}). \quad (5.13)$$

In the above expression, φ_{S} is the unknown sample phase that we desire to determine, $\Delta\varphi_{\mathrm{S}}^{\mathrm{det}}$ and $\Delta\varphi_{\mathrm{ref}}^{\mathrm{det}}$ are measured in the experiment, φ_{ref} is known, and the remaining terms may be calculated from experimental conditions. It should be noted that, in the case of dielectric surfaces, the $\Delta\varphi_L$ and $\Delta\varphi_r$ terms cancel yielding the same expressions used in prior work.[37,158]

Armed with this expanded theory, we can revisit the heterodyne data. The PSU and lens phase shifts were calculated using established expressions.[37,158] The wavelength-dependent phase shift by the lens is a function of its thickness (d), refractive index (n), and the speed of light (c)

$$\Delta\varphi_{\mathrm{lens}}(\omega_i) = \frac{d_{\mathrm{lens}} n_{\mathrm{lens}}(\omega_i)\omega_i}{c}. \quad (5.14)$$

The phase shift by the PSU is similarly dependent upon its thickness and refractive index, and additionally upon the incident angle of the beam (α)

$$\Delta\varphi_{\mathrm{PSU}}(\alpha, \omega_i) = \frac{d_{\mathrm{PSU}} n_{\mathrm{PSU}}(\omega_i) \cos\beta_i(\alpha, \omega_i)\omega_i}{c}, \quad (5.15)$$

where β_i is the refracted angle of the beam in the PSU calculated by Snell's law:

$$\beta_i(\alpha, \omega_i) = \arcsin\left(\frac{n_{\mathrm{air}}(\omega_i)}{n_{\mathrm{PSU}}(\omega_i)} \sin\alpha\right). \tag{5.16}$$

The local field phase shifts are the arguments of the complex-valued local fields. For the Au–ODT surface these were calculated as

$$\begin{aligned}
\Delta\varphi_{L_{yy}}(\omega_{\mathrm{SFG}}) &= \arg\left[L_{yy}(\omega_{\mathrm{SFG}})\right] && \text{(5.17a)}\\
&= \arg\left[1 + r_s(n_{\mathrm{air}}, n_{\mathrm{Au}}, \omega_{\mathrm{SFG}}, \theta)\right]\\
\Delta\varphi_{L_{yy}}(\omega_{\mathrm{vis}}) &= \arg\left[L_{yy}(\omega_{\mathrm{vis}})\right] && \text{(5.17b)}\\
&= \arg\left[1 + r_s(n_{\mathrm{air}}, n_{\mathrm{Au}}, \omega_{\mathrm{vis}}, \theta)\right]\\
\Delta\varphi_{L_{xx}}(\omega_{\mathrm{IR}}) &= \arg\left[L_{xx}(\omega_{\mathrm{IR}})\right] && \text{(5.17c)}\\
&= \arg\left[\sin\theta\,(1 + r_p(n_{\mathrm{air}}, n_{\mathrm{Au}}, \omega_{\mathrm{IR}}, \theta))\right],
\end{aligned}$$

where r_s and r_p are the Fresnel reflection coefficients for s- and p-polarized light, and θ is the incident angle of the beams to the surface. Analogous calculations were performed for the z-cut quartz reference material. The resulting phase contributions by the local field at $\omega_{\mathrm{IR}} = 2800\,\mathrm{cm}^{-1}$ are $\Delta\varphi_{L,\mathrm{S}} \approx -108°$, $\Delta\varphi_{L,\mathrm{ref}} = 0°$, $\Delta\varphi_{r,\mathrm{S}}(\omega_{\mathrm{SFG}}) \approx -154°$, and $\Delta\varphi_{r,\mathrm{ref}}(\omega_{\mathrm{SFG}}) = 180°$. This adds to a phase discrepancy of 266°, which is equivalent to −134° and is in agreement with the offset shown in Figure 5.5. The average of the first four few points at the low frequency end of the spectrum is $84 \pm 1°$ and represents the non-resonant phase (φ_{NR} in Eq. 5.2) of our Au–ODT sample.

5.4 Conclusions

Metals such as gold are commonly used as an internal phase reference for SFG measurements, as their vibrationally-nonresonant response provides the ability to more readily discern differences in relative phase between resonant modes in the sample. In many cases, knowledge of the absolute phase is also desired as it enables further quantification, such as the absolute orientation of chemical functional groups with respect to the surface. However, the value of the nonresonant phase of metals depends on the visible beam wavelength and is further altered by changes in electronic structure accompanying covalent bonding, such as when thiols are applied to gold. Although there are some cases in which analysis of homodyne data is able to arrive at the phase, this may be accomplished in general by heterodyne SFG measurements. Using a commonly prepared, model hydrophobic surface on gold, we have measured φ_{NR} by two independent methods. In the process, we have provided a route for determining φ_{S} for any sample, dielectric or metal.

Chapter 6

Phase-sensitive SFG of Buried Interfaces

Knowledge of the phase of the sum-frequency response, in addition to the magnitude, eliminates ambiguity in the polarity of resonant peaks. In studies of large molecules (peptides, proteins, etc.), in which interferences from many resonant modes of similar energy may yield a complicated and difficult to interpret spectrum, this additional information may allow for differentiation of small changes in molecular conformation. At buried interfaces, PS-SFG is particularly beneficial. For instance, the polar orientation of a molecule or functional group at solid–aqueous interface may not be intuitively clear, especially in the case of amphipathic solutes or mildly hydrophobic surfaces. PS-SFG can resolve this ambiguity. Additionally, the continuum of vibrational energies in the hydrogen bonding environment at aqueous interfaces result in broad peaks associated with water vibrational modes, making it difficult to confidently assign peak polarities in Lorentzian models of the spectra. Direct phase measurement eliminates this need.

One example of a question that could be resolved with buried interface PS-SFG at buried (and one that motivated the effort here) is what is the polar orientation of water adjacent to a calcite ($CaCO_3$) surface, and how does that orientation change as bulk solution pH is changed. It has been observed that the pH_{pzc} of calcite is approximately 8.0.[2] Above this pH the surface is negatively charged, and below this pH it is positively charged. In the model of the fused-silica–water interface ($pH_{pzc} = 2.0$[11]) (Chapter 3) the surface was negatively charged and imparted a strong ordering force upon the interfacial water molecules. Since all of the experiments were performed at pH 6, the sign of the $\chi^{(2)}$ response was not discussed, and it was assumed that the water molecules were roughly oriented such that the negative end of the permanent dipole was pointed away from the interface. At pH levels closer to pH_{pzc} it becomes less appropriate to assume a specific polar orientation of water, and the need for phase measurement becomes necessary to constrain the molecular orientation. Furthermore, if the sign of the surface charge is reversed, one might hypothesize that the polar orientation of the water molecules might also reverse. This latter behavior was elegantly shown using PS-SFG at the exposed liquid–surfactant–air interface. A negatively charged interface was formed by placing sodium dodecyl sulphate at the air–water surface, and a positively charged formed with cetrimonium bromide at the interface. The signs of the two OH vibrational responses (3200 and 3400 cm^{-1}) in the imaginary spectra were flipped, from which it was determined that the polar orientation of the water molecules was also flipped.[33]

There are a few published phase-resolved SFG spectra of mineral–water interfaces from Shen's and Waychunas' groups at Berkeley.[29,159,160] They have shown quite nicely, based upon PS-SFG results, the change in polar orientation of water at an Al_2O_3–water interface as a function of changing pH. However, the challenge of collecting these spectra can be inferred from the sparse nature of the data points comprising the imaginary spectra compared with the data density of the homodyne spectra.

In this chapter, use of both external phase reference (Chapter 4) and internal phase reference (Chapter 5) methods to extract phase information from the SFG response at a buried interface (defined here as any interface in which the visible and infrared sources approach through a medium other than air) is examined. This interface could be the solid–air interface approached from the solid, the liquid–air interface approached from the liquid, or a solid–liquid interface approached via the solid. The latter is the focus of this chapter.

6.1 External Phase Reference

The external phase reference method for buried interface phase-sensitive SFG is an extension of the methods presented in Chapter 4 in which the local oscillator placed upstream of the phase-shifting unit provides the reference phase signal. The only difference between the exposed interface and buried interface configurations of this method is that the visible and infrared sources pass through the sample prism prior to reaching the sample interface (Figure 6.1). I proposed that the effect of the additional prism upon the fringe pattern could be modelled following the formalism outlined in Chapter 4 by the inclusion of a single additional fixed optic to the fringe model. The challenging part of the experiment would be the exact determination of the prism optical path length in order to constrain its phase-shifting properties. In the following paragraphs, the methods developed for this experiment are outlined, followed by a discussion of some preliminary results and additional, unforeseen challenges encountered.

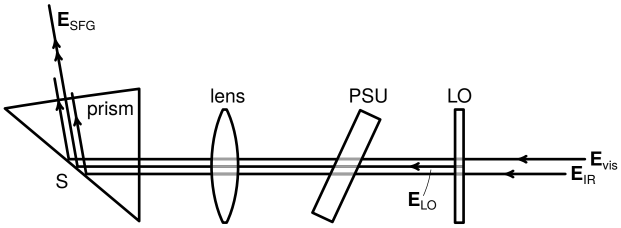

Figure 6.1: Schematic of the optical elements included in the calculation of buried interface relative phase. The phases of the electric fields $\mathbf{E}_{\text{vis}}$, $\mathbf{E}_{\text{IR}}$, and $\mathbf{E}_{\text{LO}}$ are affected as they pass through the phase shifting unit (PSU), lens, and prism on their way to the sample (S).

6.1.1 Experimental Methods

The optical setup for buried interface phase measurement was the same as described for the development of the exposed interface PS-SFG technique (Chapter 4), with one exception. In the exposed interface experiments, the pump beams were focused on the front face of a sample. In the buried interface experiments, beams were focused onto the back face of the sample (Figure 6.1). In this geometry, $\mathbf{E}_{\text{IR}}$, $\mathbf{E}_{\text{vis}}$, and $\mathbf{E}_{\text{LO}}$ pass through the sample prism to the back face of the prism, thereby adding an additional fixed optic phase-shift ($\Delta\varphi_{\text{prism}}$) to the general phase shift equation (Eq. 4.1), yielding the following expression

$$\Delta\varphi = \Delta\varphi_{\text{PSU}} + \Delta\varphi_{\text{lens}} + \Delta\varphi_{\text{prism}}. \tag{6.1}$$

Recall that the absolute phase of the sample is determined by comparison with the relative phase shift from a z-cut quartz surface. The addition of the buried interface complicates this comparison, as $\Delta\varphi_{\text{prism}}$ does not cancel in the absolute phase calculation. Therefore, it is critical that $\Delta\varphi_{\text{prism}}$ is accurately known.

An accurate determination of $\Delta\varphi_{\text{prism}}$ hinges upon how accurately both sample thickness and angle of incidence are known. As shown in Chapter 4 phase error associated with uncertainties in the distance travelled through low refractive index materials, such as air, is small compared to uncertainties elsewhere in the method. This is not the case, however, for higher index materials, such as fused silica or CaF_2, which are likely to be used as prisms in buried interface measurements. With digital calipers and a computer controlled rotation stage, sample thickness and beam angle of incidence are known to ±0.01 mm and ±0.1°, respectively. In the case of fused silica, this corresponds to an uncertainty of approximately $3 \times 360°$ at a nominal 70° angle of incidence.

6.1.2 Loss of Output Collinearity

One of the challenges of the buried interface phase measurement is that the collinear geometry of the emitted SFG fields that is maintained at the exposed interface is lost upon reflection from a buried interface. The angle of an SFG beam emitted from an interface (θ_{SFG}) is given by the phase-matching condition

$$n_{\mathrm{SFG}} k_{\mathrm{SFG}} \sin\theta_{\mathrm{SFG}} = n_{\mathrm{vis}} k_{\mathrm{vis}} \sin\theta_{\mathrm{vis}} \pm n_{\mathrm{IR}} k_{\mathrm{IR}} \sin\theta_{\mathrm{IR}}, \tag{6.2}$$

where n_i is the wavelength-dependent refractive index of the medium through which the incident source and reflected SFG beams are travelling, k_i is the wave vector of the incident and emitted beams, and θ_i is the beam angle.[6,161] Because the refractive index dispersion in air is small, the reflected angle of the local oscillator beam (θ_{LO}) is equal to the angle of the sample SFG beam (θ_{S}) for the exposed interface case. This equivalence is not maintained at a buried interface if the dispersion between the visible and infrared beams is large, and hence, the LO and sample beams in a phase experiment exit the prism at different angles, compromising the fringe pattern necessary for phase retrieval.

The magnitude of deviation from collinearity is dependent upon prism geometry and material. (There may be combinations whereby collinearity is maintained for a given prism geometry and material at a single IR wavelength, but these will be single points over the IR domain). In the case of a fused-silica–water interface, using prisms and incident angles similar to those presented in Chapter 3, the beams incident at 70°, is emitted at 68.9° rather than at the reflection angle and is refracted to 68.3° upon exiting the prism.

In order to record interference fringes by external reference method, the local oscillator signal must enter the prism at an angle slightly offset from the angle of the visible and infrared sources. Perhaps the most reproducible means for accomplishing this is to use a non-resonant buried interface in reflection geometry as a local oscillator.[49,163] Since the angle of the SFG beam is entirely dependent upon the refractive index of the incident medium, the SFG active material at the interface does not affect the angle of the SFG beam; only the material and the wavelengths of the source visible and IR fields determine the angle. By establishing the LO in reflection geometry at a buried interface of the same material as the sample interface, the LO angle is adjusted properly over the entire wavelength region studied.

Alternatively, the angles of the visible and IR source beams can travel through the LO in a non-collinear fashion, such that the angle of the LO beam at the sample surface is different from the visible and IR beams. This scenario is not as widely applicable as the reflection geometry described above, but has the advantage of minimizing alteration of the optical bench from the external interface phase measurement setup. I was successful in collecting fringes in this latter geometry a couple of times, however, I was unable to develop a systematic method for strategically “misaligning” the beams in order to observe fringes.

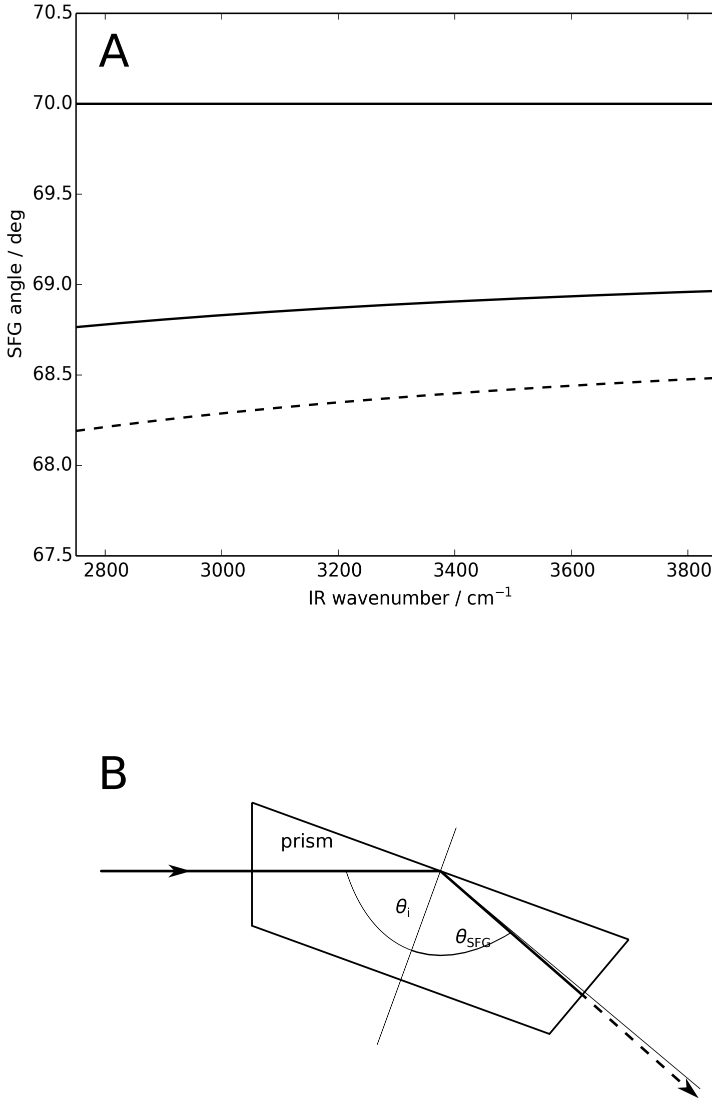

Figure 6.2: At a buried interface, the sum-frequency field exits the prism at an angle that is different from the incident angles. The plot (A) and schematic (B) show the theoretical angles of the reflected (solid, thin line), SFG (solid, thick line), and refracted SFG (dashed line) beams in a 70°/70° fused silica dove-prism. All beams enter the prism normal to the dove-cut face. Calculations assumed a 532 nm visible beam. Refractive indices were calculated using established literature values.[112,162]

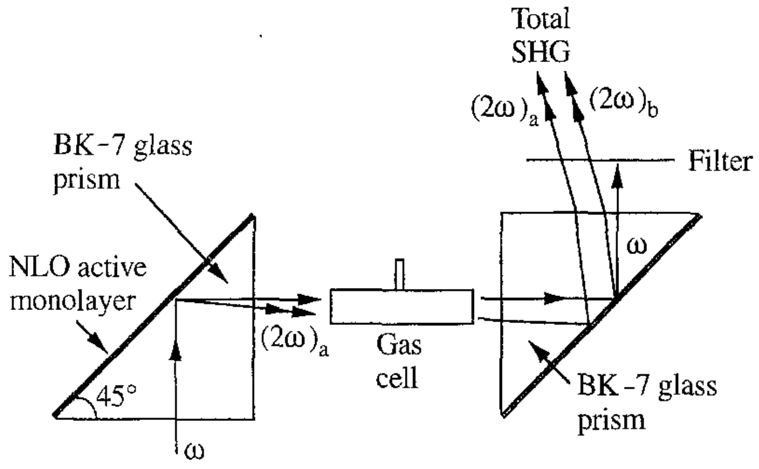

Figure 6.3: A scheme for measuring SHG interference and phases of $\chi^{(2)}$ in total internal reflection geometry. For a 1064 nm Nd:YAG fundamental and a TIR prism made of quartz, the use of a second TIR process as a reference source is applicable for polychromatic wavelengths. Reproduced with permission from Stolle et al. (1996)[49]

6.1.3 Fringe Asymmetry

A comparison of fringes collected from an exposed interface with those from a buried interface (Figure 6.4) reveals an asymmetry of fringes from the buried interface that poses an additional challenge associated with this method for buried interface PS-SFG. Fringes obtained from the exposed interface are symmetrically spaced about 0° PSU rotation (e.g. there are an equal number of peaks and troughs on either side of 0°). In contrast, fringes collected from the buried interface are more closely spaced along the PSU rotation axis at angles >0° than they are at angles <0°. Since our model of fringe shape and spacing is not applicable to asymmetric fringes, our ability to extract relative phase information from these fringes is compromised. A revisitation of the fringe theory is necessary.

In the general phase-shift equation (Eq. 4.1) the only term that is a function of PSU tilt angle is the phase shift of the PSU itself ($\Delta\varphi_{\text{PSU}}$); all other optics in the beam path were considered to impart a constant phase-shift, independent of PSU rotation. But, deviations in the horizontal plane of the visible, infrared, and local oscillator beams by the PSU actually result in a PSU tilt-angle dependence of the stationary optics. For example, it is clear that the distances travelled through the focussing lens, and hence $\Delta\varphi_{\text{lens}}$, differ between passing through the center versus slightly offset from center. In the same fashion, the beam paths through the sample prism toward the buried interface will change as the PSU rotates. We can get away with ignoring this angular dependence since the phase-shift contribution of the lens cancels in the absolute phase calculation (Eq. 4.10). However, $\Delta\varphi_{\text{prism}}$ does not cancel in the absolute phase calculation, and therefore the angular dependence must be explicitly accounted for.

The effects of functional shape upon fringe shape were examined. Four types of phase-shift functions, with respect to PSU tilt angle, were examined: constant, linear,

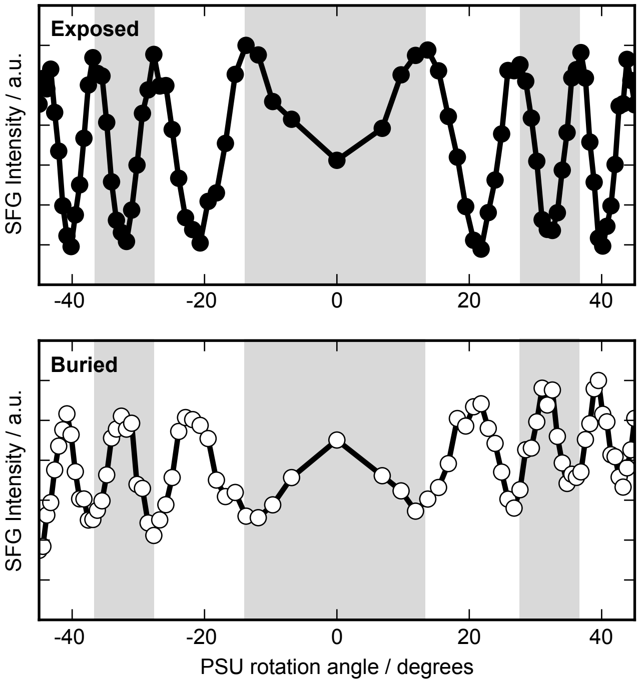

Figure 6.4: Comparison of interference fringes generated from exposed (top) and buried (bottom) CaF_2 interfaces. The most obvious difference between the two fringes is the approximately 180° phase difference. However, upon closer inspection, there appears another difference. The number of observed fringes on either side of 0° PSU rotation is equal in the exposed geometry. In contrast, an unequal number of fringes is observed on either side of zero rotation in the buried interfaced geometry.

quadratic, and cubic. The results are illustrated in Figure 6.5. For comparison, the effect on fringe shape of a constant phase-shift (zero angular dependence, horizontal blue line) is shown in Figure 6.5a. Clearly, these are the types of fringes we are used to collecting and fitting. Addition of a constant phase shift only has the effect of moving the total phase shift (black line) up or down the y-axis with no effect upon the curvature of the phase function. Addition of a linear phase-shift function (Figure 6.5b) has the effect of shifting the position of function minimum of the original PSU phase-shift (grey line), but not its curvature. As in the constant phase-shift function, the second derivative (curvature) of the linear function is zero over the entire range of tilt angles, so that the total phase-shift function does not accumulate or lose curvature. The net result is that the "center" of the fringe pattern is shifted along the PSU tilt angle axis. In contrast, it is clear from Figure 6.5c that addition of a quadratic function increases the number of fringes over the same PSU tilt angle range. This is a result of a non-zero second derivative which causes the total phase-shift function to accumulate curvature. Note that in the example shown, the effect of the quadratic function was to increase the number of fringes. It could equally have the effect of decreasing the number of fringes if the the second derivative were negative. Finally, addition of a cubic function (Figure 6.5) has the effect of increasing the curvature on one side of the phase-shift function, and decreasing the curvature on the other side. This results in an asymmetric fringe pattern in which there are more fringes on one side of zero PSU rotation than the other.

These observations reveal something about the phase-shifting function associated with the buried interface. Firstly, it confirms that there is a PSU dependence upon the phase-shift, indicating that it cannot be treated as a static optic similar to the lens. Secondly, it shows that the prism phase-shift function is similar in shape to a cubic function. The actual function will, of course, not be a simple cubic, but

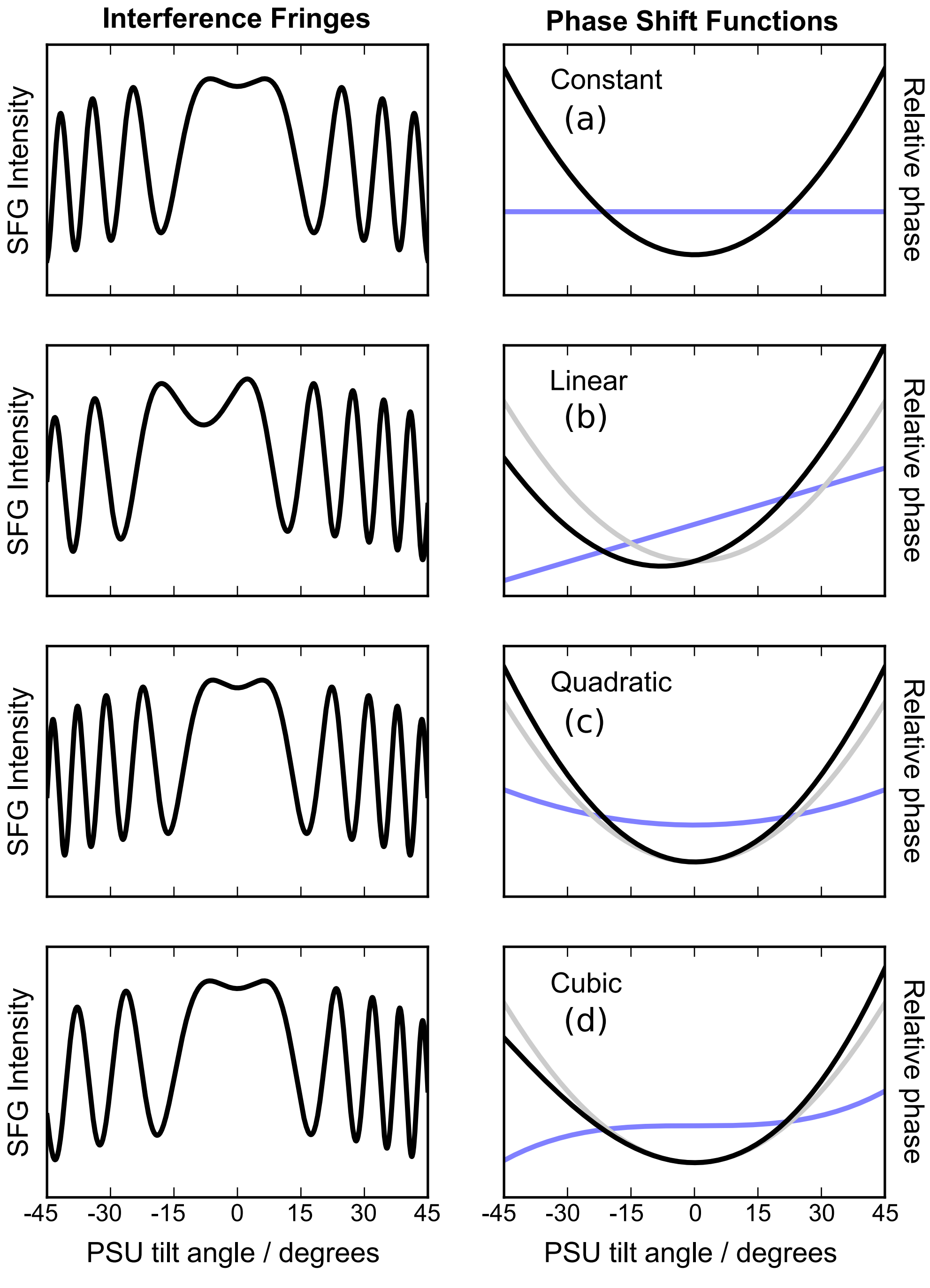

Figure 6.5: Illustration of the effects of addition of different types of phase functions upon shape of observed interference fringes. The effects of (a) constant, (b) linear, (c) quadratic, and (d) cubic functions are shown. Modeled interference fringes are shown in the left-hand column. Corresponding phase functions are shown in the right-hand column. Blue lines represent the constant, linear, quadratic, or cubic phase-shift functions. Grey lines show the PSU phase-shift function. The solid black line represents the sum of grey and blue lines.

rather a much more complicated trigonometric function, that is more than likely not independent of the PSU and lens phase-shift functions. With this insight, I set out to develop a model based upon prism shape.

The hypothesis was that if the sample prism entrance and reflection faces were not parallel, then the changes in path lengths, and hence phase-shift due to a slight displacement of beam position by the PSU could account for the asymmetric nature of the fringe. The paths (segment JK in Figure 6.6a) of the visible, infrared and LO beams through a CaF_2 prism whose front and back faces are 1° out of parallel were calculated and used to calculate $\Delta\varphi_{\text{prism}}$. The resulting phase-shift function is nearly linear in shape (Figure 6.6b) leading to a symmetric, but offset, fringe pattern. Unfortunately, this model does not fully account for the observed buried interface fringe asymmetry. The next step in model development would be to account for the slight non-collinearity of the beams exiting the focussing lens prior to the sample. In the present model the assumption was made that the angle of incidence was the same for all beams entering the prism. But we know that this is not technically correct. Deviations of the visible, IR, and LO beams by the PSU mean that refracted angles of each of the beams exiting the lens will be different.

6.1.4 Outlook

Given the challenges presented in the previous two subsections, I believe that the external phase reference method for buried interface PS-SFG will be difficult to achieve. First, the issue of fringe shape must resolved. This will likely add several degrees of freedom to the fringe model; the effects of these additional degrees of freedom upon precision of the fitted phase is unknown. Next, there are likely only a few combinations of geometry and prism material that minimize or even eliminate loss of collinearity. As such, the technique may be used to constrain the signal phase at a

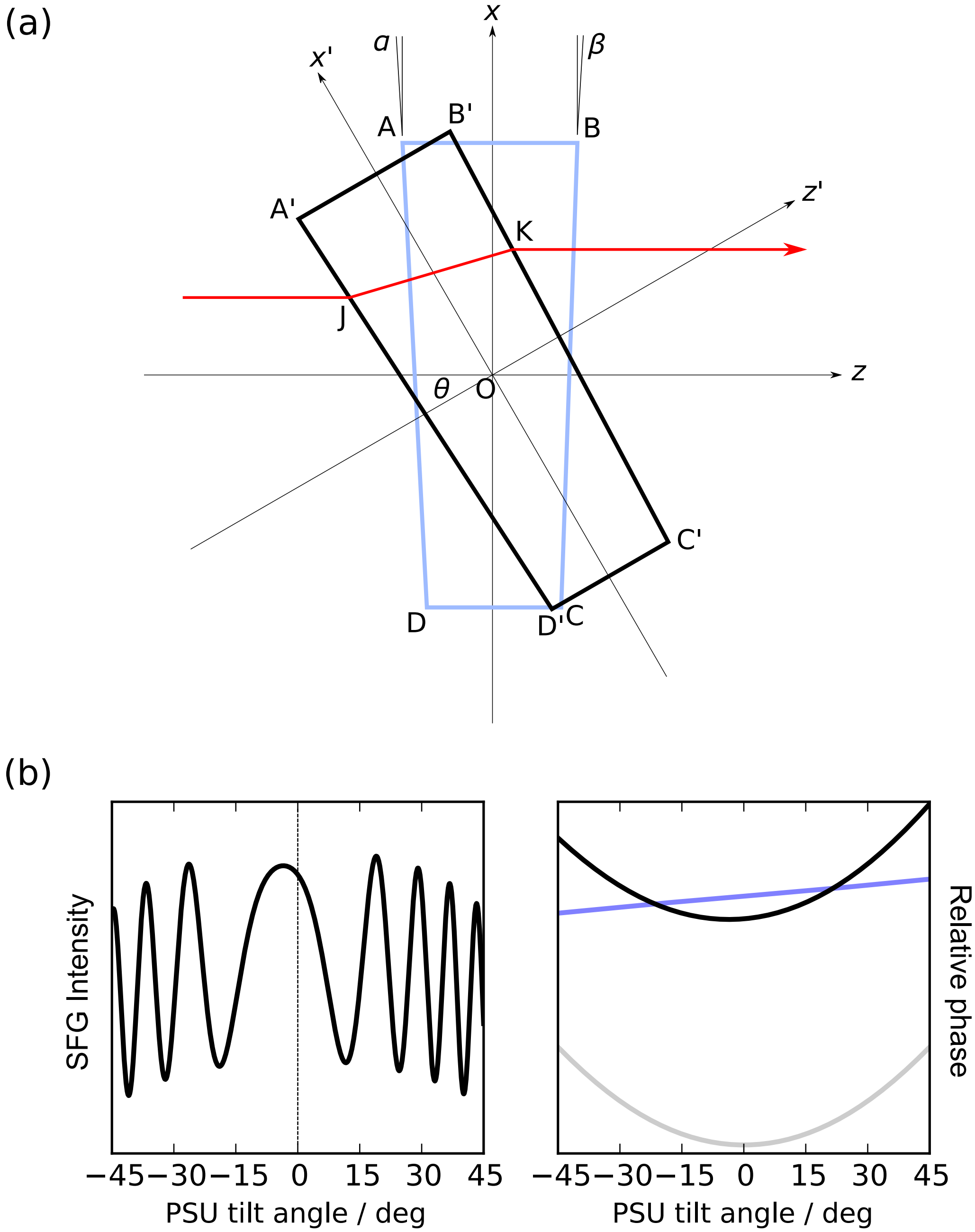

Figure 6.6: Schematic of non-parallel sample prism (a) and results of modeling PSU-dependent phase-shift due to prism (b). The modeled prism was 10 mm thick CaF_2 prism oriented at 45° angle of incidence with the front face 1° out of parallel with the back face.

few points over the entire spectral range, but it will not be a complete measurement of the magnitude and phase.

6.2 Internal Phase Reference

Another way to obtain SFG phase information is through the use of an internal reference, such as gold, as discussed in Chapter 5. The use of an internal phase reference would overcome some of the challenges encountered with the use of an external phase reference. In particular, since the phase is not determined from fitting of fringe patterns in this case, the challenges of fringe asymmetry and loss of collinearity, leading to loss of fringes, are not encountered. Undoubtedly, there will be other challenges, but I see the use of an internal phase reference as a promising route toward buried interface phase measurement.

The idea is to prepare a buried interface that consists of the prism, followed by a non-resonant contributing layer (i.e. vapor-deposited gold layer or gold nanoparticles) and deposit a thin layer of the surface of interest over the top. Provided that the physical separation of the non-resonant layer and the surface is small enough then it can be considered that the reference signal and the sample response are both created in the local field.

Data collection would follow the procedure illustrated in Figure 6.7. First, using the external phase reference method to measure the nonlinear susceptibility of a metallic interface (Chapter 5) the phase of the interface would be measured in exposed interface geometry. Next, the sample is flipped and the buried interface measured. The measured fields will be a sum of the non-resonant response ($\mathbf{E}_{\mathrm{NR}}$) of the metallic layer and the response from the sample ($\mathbf{E}_{\mathrm{S}}$). The real and imaginary spectra can then be generated from a fit of the data to the Lorentzian model of the spectra (Eq. 2.8).

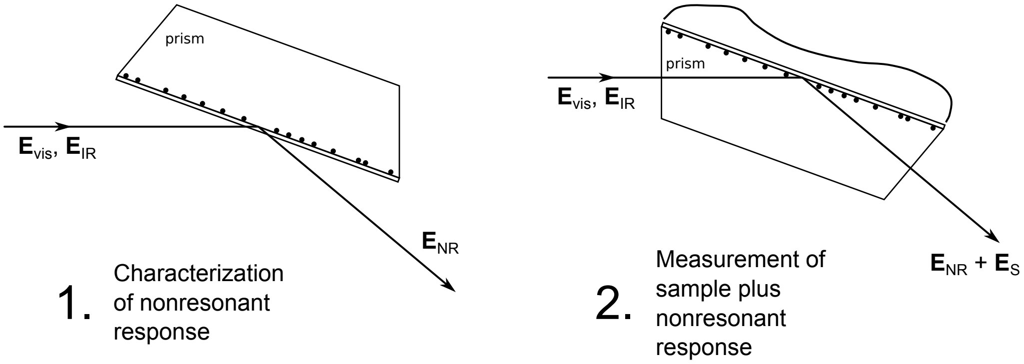

Figure 6.7: Schematic of the steps necessary to measure phase-resolved SFG sample response using an internal phase reference material.

No method comes without its own specific set of challenges. In this method I envision the biggest challenge to be the measurement of $\chi^{(2)}_{\mathrm{NR}}$ phase. Recall that this measurement requires knowledge of the refractive index of the metallic surface so that the local-field phase shift can be accounted for. In the case of the method proposed here, it cannot be assumed that the complex refractive index of thin-film gold or gold nanoparticle monolayers is the same as for thicker film gold surfaces. This might entail an additional step of measuring the refractive index of the surface first, or obtaining literature measurements of their optical properties.[164,165]

6.3 Conclusion

Phase-sensitive SFG measurements of buried interfaces remain a challenge to perform. There are a few reported measurements of this type in the literature, but exact methods for data collection have not been reported.

I have attempted to develop a universally applicable method as an extension of exposed interface PS-SFG methods. Two main challenges, loss of collinearity and fringe asymmetry, were encountered. The sources of both challenges have been investigated and we are beginning to have a better understanding of them.

I have proposed an alternate method for buried interface phase measurement that relies on theory developed for the measurement of the phase of the non-resonant response from non-dielectric interfaces. This method utilizes interference in the local field of the non-resonant response from a metallic layer with the response from the interface of interest to provide phase information of the resonant modes at the interface.

Chapter 7

Conclusions

In this thesis I set out to measure interfacial structure of water at mineral– and polymer–water interfaces using conventional and phase-sensitive SFG methods. Over the course of this research, several contributions to the understanding of interfacial structure and to the theory and practice of SFG phase measurement were made. These are listed below.

1. A model was developed to describe SFG response from the negatively charged fused-silica–aqueous solution interface over five orders of magnitude salt concentration. The model separates the SFG response into four regions of ionic strength, each of which reflect a different effect upon interfacial structure by altering ionic strength. At low ionic strength addition of salt promotes increased ordering of interfacial water by increasing the magnitude of surface charge. Further addition of salt, up to approximately $1\,\mathrm{mol\,L^{-1}}$, decreases penetration depth of the surface potential, but does not alter interfacial water structure. At the highest concentrations of NaCl, hydrogen bonding interactions are disrupted leading to a loss of ordered water at the interface.

2. Interfacial water structure and changes in structure at fused-silica, CaF_2, polystyrene, and PMMA–aqueous solution interfaces was described as a function of changes in solution NaCl concentration. The evolution of spectral intensity and shape, analyzed in the context of the model developed for the fused-silica–solution interface, revealed large difference in interfacial water structure at each of these interfaces, as well as some similarity. Water at the fused-silica interface adopted a more highly coordinated configuration over most of concentration range measured. Similar coordination behavior was observed at the PMMA interface, despite a much different extent of ordering. Likewise, water adopted a higher coordination configuration at the polystyrene interface between concentrations of $1 \times 10^{-5}\,\mathrm{mol\,L^{-1}}$ and $0.1\,\mathrm{mol\,L^{-1}}$. However, at concentrations greater than $0.1\,\mathrm{mol\,L^{-1}}$ its coordination state abruptly decreased. There appeared an even distribution of higher- and lower-coordinated water at the CaF_2 interface over lower concentration ranges, giving way to only lower-coordination water at high salt concentration.

3. Methods were established for obtaining the phase of SFG signal from exposed interfaces with high precision and accuracy. Our first presentation of fringe shape model used in a collinear geometry phase-sensitive SFG experiment described the extraction of signal phase from the interference patterns, but not signal intensity, which was still obtained through homodyne detection. Building upon our group's model of interference fringe shape, a method was demonstrated to obtain both magnitude and phase simultaneously from the interference pattern. The importance of this method is that it eliminates potential phase errors associated with addition and removal of optics within the experimental setup, thereby improving the accuracy and precision of the phase measurement.

4. Expanded the theory for phase-sensitive SFG measurement of non-dielectric interfaces. Determination of the SFG signal phase requires comparison of the phase measured from a sample interface with a phase reference material. This comparison is straightforward when comparing two dielectric materials. However, when the sample is metallic, additional consideration of the effects of the local field upon the detected signal and phase must be made. By treating the local field as an additional "virtual" optic in the experimental setup, its effects may be accounted for, allowing for accurate determination of phase. This theory is applicable to phase measurement at any type of exposed interface and opens the door to the use the non resonant response from gold (or other metals) as a phase reference for the measurement of the *absolute* phase of an interface.
5. Buried interface phase-sensitive SFG methods were explored. Although attempts at measuring the phase of SFG signals originating from buried interfaces were met with limited success, much was learned. Most interesting was the appearance of an asymmetric pattern of interference fringes, which, based upon analysis of phase-shift function types points to an effect of the non-parallel nature of the front and back faces of the sample prism. Based upon theory developed for measuring SFG signal phase from metallic surfaces, another route to buried interface phase measurement looks promising.

7.1 Recommendations for Future Work

The highest priority direction for future work is to develop a method for buried interface phase measurement using the gold as an internal standard as outlined in Chapter 6; much of the groundwork for this method has been established. Development of this capability would undoubtedly aid in the investigation interfaces with greater and greater complexity, such as large molecule adsorption, lipid bilayers, and reversals in surface charge.

Within the geochemical context, two avenues of research that warrant exploration are (1) examination of water structure at calcium carbonate interfaces and (2) investigation of the adopted structure and conformation of large polyelectrolytes, such as humic and fulvic acids, upon adsorption to mineral or polymer surfaces.

The interfacial structure of water at a $CaCO_3$ interface has significant ecological and biogeochemical importance. Recently, a few groups have presented spectroscopic and *ab initio* molecular modeling results revealing the speciation of chemisorbed, hydrolyzed water on the carbonate mineral surface.[166–168] Others have used electrophoretic mobility measurements of calcite particles over a range of pH to infer surface speciation.[169] None, however, have examined the structure of water at the first few layers adjacent the mineral surface. A phase-sensitive SFG analysis of this system over a broad range of pH and ionic strength would address this gap in knowledge in a very detailed manner.

Humic and fulvic acids in natural systems result from the biodegradation of plant matter. These polyelectrolytes commonly coat mineral particles and can bind to a variety of chemical species, including oils and trace metal ions. As such, they may act as transport vectors for environmental contaminants, and an understanding of their reactivity in a variety of conditions (pH, temperature, salinity) is necessary for development of remediation protocols. It has recently been shown, using SFG techniques, that the structure and binding affinity of model polyelectrolytes at the water–nonpolar fluid interface is dependent upon metal ions in solution.[170] It is reasonable to assume a similar behavior at mineral–water interfaces. In addition, evidence suggests that there is a kinetic component to the structure of adsorbed humic acids.[171] Quartz crystal microbalance studies of humic acid adsorption to an alumina surface indicate a two step process occurring over the course of 40 min. Differences in the viscoelastic character of the adsorbed material in the two steps suggests structural differences. Buried interface PS-SFG would be well suited to study these systems and would add structural detail to the results already obtained by other methods.

Bibliography

[1] Covert, P. A. An Examination of the Form and Variability of Manganese Oxide in Columbia River Suspended Material. M.Sc. thesis, Oregon State University, Corvallis, 2001.

[2] Van Cappellen, P.; Charlet, L.; Stumm, W.; Wersin, P. *Geochim. Cosmochim. Acta* **1993**, *57*, 3505–3518.

[3] Weiner, S.; Dove, P. M. *Biomineralization, Reviews in Mineralogy and Geochemistry*; 2003; Vol. 54; pp 1–29.

[4] Waldbusser, G. G.; Brunner, E. L.; Haley, B. A.; Hales, B.; Langdon, C. J.; Prahl, F. G. *Geophys. Res. Lett.* **2013**, *40*, 2171–2176.

[5] Klaas, C.; Archer, D. E. *Global Biogeochem. Cycles* **2002**, *16*, 1116.

[6] Lambert, A. G.; Davies, P. B.; Neivandt, D. J. *Appl. Spectrosc. Rev.* **2005**, *40*, 103–145.

[7] Ji, N.; Ostroverkhov, V.; Chen, C.; Shen, Y. R. *J. Am. Chem. Soc.* **2007**, *129*, 10056–10057.

[8] Yamaguchi, S.; Tahara, T. *J. Chem. Phys.* **2008**, *129*, 101102.

[9] Shen, Y. R. *Annu. Rev. Phys. Chem.* **2013**, *64*, 129–150.

[10] Stumm, W.; Morgan, J. J. *Aquatic Chemistry: Chemical Equilibria and Rates in Natural Qaters*; Wiley-Interscience: New York, 1981.

[11] Ong, S.; Zhao, X.; Eisenthal, K. B. *Chem. Phys. Lett.* **1992**, *191*, 327–335.

[12] Davis, J. A. *Geochim. Cosmochim. Acta* **1982**, *46*, 2381–2393.

[13] Grahame, D. C. *Chem. Rev.* **1947**, *41*, 441–501.

[14] Morel, F. M. M.; Hering, J. G. *Principles and Applications of Aquatic Chemistry*; Wiley-Interscience: New York, 1993.

[15] Greene, P. R.; Bain, C. D. *Colloids Surf. B* **2005**, *45*, 174–180.

[16] Kahan, T. F.; Reid, J. P.; Donaldson, D. J. *J. Phys. Chem. A* **2007**, *111*, 11006–11012.

[17] Wren, S. N.; Donaldson, D. *Chem. Phys. Lett.* **2012**, *522*, 1–10.

[18] Blaudez, D.; Buffeteau, T.; Cornut, J. C.; Desbat, B.; Excafre, N.; Pezolet, M.; Turlet, J. M. *Appl. Spectrosc.* **1993**, *47*, 869–874.

[19] Blaudez, D.; Turlet, J.-M.; Dufourcq, J.; Bard, D.; Buffeteau, T.; Desbat, B. *J. Chem. Soc. Faraday Trans.* **1996**, *92*, 525–530.

[20] Westerberg, S.; Wang, C.; Somorjai, G. A. *Surf. Sci.* **2005**, *582*, 137–144.

[21] Hall, S. A.; Jena, K. C.; Covert, P. A.; Roy, S.; Trudeau, T. G.; Hore, D. K. *J. Phys. Chem. B* **2014**, *118*, 5617–5636.

[22] Shen, Y. R. *Nature* **1989**, *337*, 519–525.

[23] Hall, S. A.; Hickey, A. D.; Hore, D. K. *J. Phys. Chem. C* **2010**, *114*, 9748–9757.

[24] Mondal, J.; Nihonyanagi, S.; Yamaguchi, S.; Tahara, T. *J. Am. Chem. Soc.* **2010**, *132*, 10656–10657.

[25] Jena, K. C.; Covert, P. A.; Hall, S. A.; Hore, D. K. *J. Phys. Chem. C* **2011**, *115*, 15570–15574.

[26] Velarde, L.; Zhang, X.; Lu, Z.; Joly, A. G.; Wang, Z.; Wang, H.-F. *J. Chem. Phys.* **2011**, *135*, 241102.

[27] Superfine, R.; Huang, J. Y.; Shen, Y. R. *Opt. Lett.* **1990**, *15*, 1276–1278.

[28] Superfine, R.; Huang, J. Y.; Shen, Y. R. *Chem. Phys. Lett.* **1990**, *172*, 303–306.

[29] Zhang, L.; Tian, C.; Waychunas, G.; Shen, Y. R. *J. Am. Chem. Soc.* **2008**, *130*, 7686–7694.

[30] Tian, C.; Ji, N.; Waychunas, G. A.; Shen, Y. R. *J. Am. Chem. Soc.* **2008**, *130*, 13033–13039.

[31] Tian, C.; Shen, Y. R. *J. Am. Chem. Soc.* **2009**, *131*, 2790–2791.

[32] Ji, N.; Ostroverkhov, V.; Tian, C. S.; Shen, Y. R. *Phys. Rev. Lett.* **2008**, *100*, 096102.

[33] Nihonyanagi, S.; Yamaguchi, S.; Tahara, T. *J. Chem. Phys.* **2009**, *130*, 204704.

[34] Stiopkin, I. V.; Jayathilake, H. D.; Bordenyuk, A. N.; Benderskii, A. V. *J. Am. Chem. Soc.* **2008**, *130*, 2271–2275.

[35] Nihonyanagi, S.; Yamaguchi, S.; Tahara, T. *J. Am. Chem. Soc.* **2010**, *132*, 6867–6869.

[36] Chen, X.; Hau, W.; Huang, Z.; Allen, H. *J. Am. Chem. Soc.* **2010**, *132*, 11336–11342.

[37] Jena, K. C.; Covert, P. A.; Hore, D. K. *J. Chem. Phys.* **2011**, *134*, 044712.

[38] Chang, R. K.; Ducuing, J.; Bloembergen, N. *Phys. Rev. Lett.* **1965**, *15*, 6–8.

[39] Kemnitz, K.; Bhattacharyya, K.; Hicks, J. M.; Pinto, G. R.; Eisenthal, K. B. *Chem. Phys. Lett.* **1986**, *131*, 285–290.

[40] Corn, R. A.; Higgins, D. A. *Chem. Rev.* **1994**, *94*, 107–125.

[41] Min, M.; Jeon, Y.; Sung, J.; Seok, S.; Kim, D.; Kim, H.; Yoon, K. *J. Phys. Chem. C* **2007**, *111*, 18159–18163.

[42] Schuhacher, D.; Marowsky, G.; Fedyanin, A. A.; Dolgova, T. V.; Aktsipetrov, O. A. *Mater. Sci. Semicond. Process.* **2001**, *4*, 51–53.

[43] Carriles, R.; An, Y. Q.; Downer, M. C. *Phys. Stat. Sol.* **2005**, *242*, 3001–3006.

[44] Lu, R.; Rao, Y.; Zhang, W.-K.; Wang, H.-F. *Proc. SPIE Conf. Nonlinear. Spectrosc.* **2002**, *4812–4815*, 115–124.

[45] Kajikawa, K.; Wang, L.-M.; Isoshima, T.; Wada, T.; Knoll, W.; Sasabe, H.; Okada, S.; Nakanishi, H. *Thin Solid Films* **1996**, *284–285*, 612–614.

[46] Chen, J.; Machida, S.; Yamanoto, Y. *Opt. Lett.* **1998**, *23*, 676–678.

[47] Mifflin, A.; Musorrafiti, M.; Konek, C.; Geiger, F. *J. Phys. Chem. B* **2005**, *109*, 24386–24390.

[48] Lu, R.; Wang, H.-F. *Chin. Phys. Lett.* **2003**, *20*, 1269–1271.

[49] Stolle, R.; Marowsky, G.; Schwarzberg, E.; Berkovic, G. *Appl. Phys. B* **1996**, *63*, 491–498.

[50] Jeon, Y.; Min, H.; Kim, D.; Oh-E, M. *J. Kor. Phys. Soc.* **2005**, *46*, S159–S162.

[51] Du, Q.; Freysz, E.; Shen, Y. R. *Phys. Rev. Lett.* **1994**, *72*, 238–241.

[52] Jena, K. C.; Hore, D. K. *J. Phys. Chem. C* **2009**, *113*, 15364–15372.

[53] Schnitzer, C.; Baldelli, S.; Shultz, M. J. *J. Phys. Chem. B* **2000**, *104*, 585–590.

[54] Gragson, D. E.; Richmond, G. L. *J. Am. Chem. Soc.* **1998**, *120*, 366–375.

[55] Liu, D.; Ma, G.; Levering, L. M.; Allen, H. C. *J. Phys. Chem. B* **2004**, *108*, 2252–2260.

[56] Yang, Z.; Li, Q.; Chou, K. C. *J. Phys. Chem. C* **2009**, *113*, 8201–8205.

[57] Toney, M. F.; Howard, J. N.; Richer, J.; Borges, G. L.; Gordon, J. G.; Melroy, O. R.; Wiesler, D. G.; Yee, D.; Sorensen, L. B. *Nature* **1994**, *368*, 444–446.

[58] Nihonyanagi, S.; Ye, S.; Uosaki, K. *Electrochim. Acta* **2001**, *46*, 3057–3061.

[59] Mucha, M.; Frigato, T.; Levering, L. M.; Allen, H. C.; Tobias, D. J.; Dang, L. X.; Jungwirth, P. *J. Phys. Chem. B* **2005**, *109*, 7617–7623.

[60] Chen, X.; Yang, T.; Kataoka, S.; Cremer, P. S. *J. Am. Chem. Soc.* **2007**, *129*, 12272–12279.

[61] Fenter, P.; Sturchio, N. C. *Prog. Surf. Sci.* **2004**, *77*, 171–258.

[62] Zhang, Z. et al. *Langmuir* **2004**, *20*, 4954–4969.

[63] Park, C.; Fenter, P. A.; Nagy, K. L.; Sturchio, N. C. *Phys. Rev. Lett.* **2006**, *97*, 016101.

[64] Park, C.; Fenter, P. A.; Sturchio, N. C.; Nagy, K. L. *Langmuir* **2008**, *24*, 13993–14004.

[65] Xu, D.; Leng, Y.; Chen, Y.; Li, D. *Appl. Phys. Lett.* **2009**, *94*, 201901.

[66] Dimitrov, D. I.; Raev, N. D. *J. Electroanal. Chem.* **2000**, *486*, 1–8.

[67] Lee, S. H.; Rossky, P. J. *J. Chem. Phys.* **1994**, *100*, 3334–3345.

[68] Yeh, I.-C.; Berkowitz, M. L. *J. Chem. Phys.* **1999**, *110*, 7935–7942.

[69] Eftekhari-Bafrooei, A.; Borguet, E. *J. Am. Chem. Soc.* **2009**, *131*, 12034–12035.

[70] Teschke, O.; Ceotto, G.; de Souza, E. F. *Phys. Rev. E* **2001**, *64*, 011605.

[71] Shen, Y. R. *Annu. Rev. Phys. Chem.* **1989**, *40*, 327–350.

[72] Eisenthal, K. B. *Chem. Rev.* **1996**, *96*, 1343–1360.

[73] Vogel, V.; Shen, Y. R. *Ann. Rev. Mater. Sci.* **1991**, *21*, 515–534.

[74] Geiger, F. M. *Ann. Rev. Phys. Chem.* **2009**, *60*, 61–83.

[75] Bloembergen, N.; Pershan, P. S. *Phys. Rev.* **1962**, *128*, 606–622.

[76] Petersen, P. B.; Saykally, R. J. *Ann. Rev. Phys. Chem.* **2006**, *57*, 333–364.

[77] Zhao, X.; Ong, S.; Eisenthal, K. B. *Chem. Phys. Lett.* **1993**, *202*, 513–520.

[78] Stack, A. G.; Higgins, S. R.; Eggleston, C. M. *Geochim. Cosmochim. Acta* **2001**, *65*, 3055–3063.

[79] Salafsky, J. S.; Eisenthal, K. B. *J. Phys. Chem. B* **2000**, *104*, 7752–7755.

[80] Wei, X.; Hong, S.-C.; Zhuang, X.; Goto, T.; Shen, Y. R. *Phys. Rev. E* **2000**, *62*, 5160–5172.

[81] Briggman, K. A.; Stephenson, J. C.; Wallace, W. E.; Richter, L. J. *J. Phys. Chem. B* **2001**, *105*, 2785–2791.

[82] Wang, J.; Buck, S.; Chen, Z. *J. Phys. Chem. B* **2002**, *106*, 11666–11672.

[83] Tarbuck, T. L.; Ota, S. T.; Richmond, G. L. *J. Am. Chem. Soc.* **2006**, *128*, 14519–14527.

[84] Scatena, L. F.; Brown, M. G.; Richmond, G. L. *Science* **2001**, *292*, 908–912.

[85] Wang, J.; Buck, S. M.; Even, M. A.; Chen, Z. *J. Am. Chem. Soc.* **2002**, *124*, 13302–13305.

[86] Watry, M. R.; Tarbuck, T. L.; Richmond, G. L. *J. Phys. Chem. B* **2003**, *107*, 512–518.

[87] Yeganeh, M. S.; Dougal, S. M.; Pink, H. S. *Phys. Rev. Lett.* **1999**, *83*, 1179–1182.

[88] Gragson, D. E.; McCarty, B. M.; Richmond, G. L. *J. Am. Chem. Soc.* **1997**, *119*, 6144–6152.

[89] Gragson, D. E.; Richmond, G. L. *J. Phys. Chem. B* **1998**, *102*, 3847–3861.

[90] Hopkins, A. J.; Schrödle, S.; Richmond, G. L. *Langmuir* **2010**, *26*, 10784–10790.

[91] Jena, K. C.; Covert, P. A.; Hore, D. K. *J. Phys. Chem. Lett.* **2011**, *2*, 1056–1061.

[92] Flores, S. C.; Kherb, J.; Cremer, P. S. *J. Phys. Chem. C* **2012**, *116*, 14408–14413.

[93] Azam, M. S.; Weeraman, C. N.; Gibbs-Davis, J. M. *J. Phys. Chem. C* **2013**, *117*, 8840–8850.

[94] Dewan, S.; Yeganeh, M. S.; Borguet, E. *J. Phys. Chem. Lett.* **2013**, *4*, 1977–1982.

[95] Lee, C. H.; Chang, R. K.; Bloembergen, N. *Phys. Rev. Lett.* **1967**, *18*, 167–170.

[96] Aktsipetrov, O. A.; Fedyanin, A. A.; Dadap, J. I.; Downer, M. C. *Laser Phys.* **1996**, *6*, 1142–1151.

[97] Eichler, H.; Gunter, P.; Pohl, D. *Laser induced dynamic gratings*; Springer: Berlin, 1986.

[98] de Beer, A. G. F.; Campen, R. K.; Roke, S. *Phys. Rev. B* **2010**, *82*, 235431.

[99] Kataoka, S.; Gurau, M. C.; Albertorio, F.; Holden, M. A.; Lim, S. M.; Yang, R. D.; Cremer, P. S. *Langmuir* **2004**, *20*, 1662–1666.

[100] Kim, J.; Kim, G.; Cremer, P. S. *J. Am. Chem. Soc.* **2002**, *124*, 8751–8756.

[101] Kitamura, A.; Fujiwara, K.; Yamamoto, T.; Nishikawa, S.; Moriyama, H. *J. Nucl. Sci. Technol.* **1999**, *36*, 1167–1175.

[102] Bockris, J. O.; Reddy, A. K. N. *Modern Electrochemistry*; Plenum Press, New York, 1970.

[103] Morel, F. M. M. *Principles of Aquatic Chemistry*; John Wiley & Sons, 1983.

[104] Ahmed, S. M. *Can. J. Chem.* **1966**, *44*, 1663–1670.

[105] Abenroth, R. P. *J. Coll. Inter. Sci.* **1970**, *34*, 591–596.

[106] Zheng, D.-S.; Wang, Y.; Liu, A.-A.; Wang, H.-F. *Int. Rev. Phys. Chem.* **2008**, *27*, 629–664.

[107] Backus, E. H. G.; Garcia-Araez, N.; Bonn, M.; Bakker, H. J. *J. Chem. Phys. C* **2012**, *116*, 23351–23361.

[108] Zhuang, X.; Miranda, P. B.; Kim, D.; Shen, Y. R. *Phys. Rev. B* **1999**, *59*, 12632–12640.

[109] Kasarova, S. N.; Sultanova, N. G.; Ivanov, C. D.; Nikolov, I. D. *Opt. Mater.* **2007**, *29*, 1481–1490.

[110] Daimon, M.; Masumura, A. *Appl. Opt.* **2002**, *41*, 5275–5281.

[111] Ghosh, G. *Opt. Commun.* **1999**, *163*, 95–102.

[112] Ciddor, P. E. *Appl. Opt.* **1996**, *35*, 1566–1573.

[113] Segelstein, D. J. The Complex Refractive Index of Water. M.Sc. thesis, University of Missouri, Kansas City, 1981.

[114] Querry, M. R.; Waring, R. C.; Holland, W. E.; Hale, G. M.; Nijm, W. *J. Opt. Soc. Am.* **1972**, *62*, 849–855.

[115] Querry, M. R.; Holland, W. E.; Waring, R. C. *J. Opt. Soc. Am.* **1976**, *66*, 830–836.

[116] Ostroverkhov, V.; Waychunas, G. A.; Shen, Y. R. *Chem. Phys. Lett.* **2004**, *386*, 144–148.

[117] Becraft, K. A.; Richmond, G. L. *Langmuir* **2001**, *17*, 7721–7724.

[118] Becraft, K. A.; Moore, F. G.; Richmond, G. L. *J. Phys. Chem. B* **2003**, *107*, 3675–3678.

[119] Eftekhari-Bafrooei, A.; Borguet, E. *J. Am. Chem. Soc.* **2010**, *132*, 3756–3761.

[120] Choi, H. S. *Can. Metall. Quart.* **1963**, *2*, 405–414.

[121] Becraft, K. A.; Moore, F. G.; Richmond, G. L. *Phys. Chem. Chem. Phys.* **2004**, *6*, 1880–1889.

[122] Garand, A.; Mucci, A. *Mar. Chem.* **2004**, *91*, 27–35.

[123] Zhang, D.; Dougal, S. M.; Yeganeh, M. S. *Langmuir* **2000**, *16*, 4528–4532.

[124] Klein, R. J.; Fischer, D. A.; Lenhart, J. L. *Langmuir* **2008**, *24*, 8187–8197.

[125] Bekele, S.; Tsige, M. *Langmuir* **2013**, *29*, 13230–13238.

[126] Lubarsky, G. V.; Browne, M. M.; Mitchell, S. A.; Davidson, M. R.; Bradley, R. H. *Colloids Surf. B* **2005**, *44*, 56–63.

[127] Tian, C. S.; Shen, Y. R. *Proc. Natl. Acad. Sci. U. S. A.* **2009**, *106*, 15148–15153.

[128] Feng, R.-R.; Guo, Y.; Lü, R.; Velarde, L.; Wang, H.-F. *J. Phys. Chem. A* **2011**, *115*, 6015–6027.

[129] Liu, Y.; Wolf, L. K.; Messmer, M. C. *Langmuir* **2001**, *17*, 4329–4335.

[130] Sovago, M.; Vartiainen, E.; Bonn, M. *J. Phys. Chem. C* **2009**, *113*, 6100–6106.

[131] Morita, A.; Hynes, J. T. *Chem. Phys.* **2000**, *258*, 371–390.

[132] Morita, A.; Hynes, J. T. *J. Phys. Chem. B* **2002**, *106*, 673–685.

[133] Morita, A. *J. Phys. Chem. B* **2006**, *110*, 3158–3163.

[134] Nihonyanagi, S.; Ishiyama, T.; Lee, T.-K.; Yamaguchi, S.; Bonn, M.; Morita, A.; Tahara, T. *J. Am. Chem. Soc.* **2011**, *133*, 16875–16880.

[135] Ye, S.; Nihonyanagi, S.; Uosaki, K. *Phys. Chem. Chem. Phys.* **2001**, *3*, 3463–3469.

[136] Ward, R. N.; Davies, P. B.; Bain, C. D. *J. Phys. Chem.* **1993**, *97*, 7141–7143.

[137] Lu, X.; Myers, J. N.; Chen, Z. *Langmuir* **2014**, *30*, 9418–9422.

[138] Maurer, S.; Waschatko, G.; Schach, D.; Zielbauer, B. I.; Dahl, J.; Weidner, T.; Bonn, M.; Vilgis, T. A. *J. Phys. Chem. B* **2013**, *117*, 13872–13883.

[139] Kett, P. J. N.; Casford, M. T. L.; Davies, P. B. *J. Phys. Chem. B* **2013**, *117*, 6455–6465.

[140] Barth, C.; Jakubczyk, D.; Kubas, A.; Anastassacos, F.; Brenner-Weiss, G.; Fink, K.; Schepers, U.; Bräse, S.; Koelsch, P. *Langmuir* **2012**, *28*, 8456–8462.

[141] Johal, M. S.; Ward, R. N.; Davies, P. B. *J. Phys. Chem.* **1996**, *100*, 274–279.

[142] Ward, R. N.; Davies, P. B.; Bain, C. D. *J. Phys. Chem. B* **1997**, *101*, 1594–1601.

[143] Himmelhaus, M.; Eisert, F.; Buck, M.; Grunze, M. *J. Phys. Chem. B* **2000**, *104*, 576–584.

[144] Zolk, M.; Eisert, F.; Pipper, J.; Herrwerth, S.; Eck, W.; Buck, M.; Grunze, M. *Langmuir* **2000**, *16*, 5849–5852.

[145] Jacob, J. D. C.; Rittikulsittichai, S.; Lee, T. R.; Baldelli, S. *J. Phys. Chem. C* **2013**, *117*, 9355–9365.

[146] Weidner, T.; Apte, J. S.; Gamble, L. J.; Castner, D. G. *Langmuir* **2009**, *26*, 3433–3440.

[147] Baugh, L.; Weidner, T.; Baio, J. E.; Nguyen, P.-C. T.; Gamble, L. J.; Stayton, P. S.; Castner, D. G. *Langmuir* **2010**, *26*, 16434–16441.

[148] Buck, M.; Eisert, F.; Grunze, M.; Trager, F. *Appl. Phys. A.* **1995**, *60*, 1–12.

[149] Dreesen, L.; Humbert, C.; Celebi, M.; Lemaire, J. J.; Mani, A. A.; Thiry, P. A.; Peremans, A. *Appl. Phys. B* **2002**, *74*, 621–625.

[150] Cimatu, K.; Baldelli, S. *J. Phys. Chem. C* **2009**, *113*, 16575–16588.

[151] Hosseinpour, S.; Hedberg, J.; Baldelli, S.; Leygraf, C.; Johnson, M. *J. Phys. Chem. C* **2011**, *115*, 23871–23879.

[152] Hernandez, M.; Chinwangso, P.; Cimatu, K.; Srisombat, L.; Lee, T. R.; Baldelli, S. *J. Phys. Chem. C* **2011**, *115*, 4688–4695.

[153] Bain, C. D.; Troughton, E. B.; Tao, Y.-T.; Evall, J.; Whitesides, G. M.; Nuzzo, R. G. . *J. Am. Chem. Soc.* **1989**, *111*, 321–335.

[154] Feller, M. B.; Chen, W.; Shen, Y. R. *Phys. Rev. A* **1991**, *43*, 6778–6792.

[155] Wadayama, T.; Yano, H.; Sasaki, Y.; Takahashi, J.-i.; Hatta, A. *Mat. Trans.* **2004**, *45*, 86–91.

[156] Liu, Y.; Kalambur, A. T.; Rabolt, J. F. *Langmuir* **2004**, *20*, 816–822.

[157] Guyot-Sionnest, P.; Hunt, J. H.; Shen, Y. R. *Phys. Rev. Lett.* **1987**, *59*, 1597–1600.

[158] Covert, P. A.; FitzGerald, W. A.; Hore, D. K. *J. Chem. Phys.* **2012**, *137*, 014201.

[159] Sung, J.; Shen, Y. R.; Waychunas, G. A. *J. Phys.: Condens. Matter* **2012**, *24*, 124101.

[160] Sung, J.; Zhang, L.; Tian, C.; Shen, Y. R.; Waychunas, G. A. *J. Phys. Chem. C* **2011**, *115*, 13887–13893.

[161] Boyd, R. W. *Nonlinear Optics*; Academic Press: Boston, 1992.

[162] Malitson, I. H. *J. Opt. Soc. Am.* **1965**, *55*, 1205–1209.

[163] Stolle, R. Aspekte von Phasenmessungen in der Nichlinearen Optik. Ph.D. thesis, Georg-August-Universität zu Göttingen, 1995.

[164] Ung, T.; Liz-Marzan, L. M.; Mulvaney, P. *Colloids and Surfaces A: Physicochemical and Engineering Aspects* **2002**, *202*, 119–126.

[165] Chen, M.; Horn, R. G. *J. Colloid Interface Sci.* **2007**, *315*, 814–817.

[166] Lardge, J. S.; Duffy, D. M.; Gillan, M. J. *J. Phys. Chem. C* **2009**, *113*, 7207–7212.

[167] Lardge, J. S.; Duffy, D. M.; Gillan, M. J.; Watkins, M. *J. Phys. Chem. C* **2010**, *114*, 2664–2668.

[168] Cooke, D. J.; Gray, R. J.; Sand, K. K.; Stipp, S. L. S.; Elliott, J. A. *Langmuir* **2010**, *26*, 14520–14529.

[169] Heberling, F.; Trainor, T. P.; Lutzenkirchen, J.; Eng, P.; Denecke, M. A.; Bosbach, D. *J. Colloid Interface Sci.* **2011**, *354*, 843–857.

[170] Beaman, D. K.; Robertson, E. J.; Richmond, G. L. *Langmuir* **2012**, *28*, 14245–14253.

[171] Eita, M. *Soft Matter* **2011**, *7*, 709–715.